

# INTERFACE Force Field for Alumina with Validated Bulk Phases and a pH-Resolved Surface Model Database for Electrolyte and Organic Interfaces

Cheng Zhu,<sup>1</sup> Krishan Kanhaiya,<sup>1</sup> Samir Darouich,<sup>2</sup> Sean P. Florez,<sup>1</sup> Karnajit Sen,<sup>2</sup> Patrick Keil,<sup>3</sup>  
Nawel S. Khelfallah,<sup>4</sup> Eduard Schreiner,<sup>2</sup> Ratan K. Mishra,<sup>2\*</sup> Hendrik Heinz<sup>1\*</sup>

<sup>1</sup> Department of Chemical and Biological Engineering, University of Colorado Boulder, Boulder,  
CO 80303-0596, USA

<sup>2</sup> Group Research, BASF SE, Carl-Bosch-Strasse 38, 67056 Ludwigshafen am Rhein, Germany

<sup>3</sup> BASF Coatings GmbH, Glasuritstrasse 1, 48165 Münster, Germany

<sup>4</sup> Chemetall GmbH, Trakhener Strasse 3, 60487 Frankfurt am Main, Germany

\* Correspondence to: [ratan.mishra@basf.com](mailto:ratan.mishra@basf.com), [hendrik.heinz@colorado.edu](mailto:hendrik.heinz@colorado.edu)

## Abstract

Alumina and aluminum oxyhydroxides underpin chemical-engineering technologies from heterogeneous catalysis, corrosion protection, functional coatings, energy-storage devices, to biomedical components. Yet molecular models that predictively connect phase structure, pH-dependent surface chemistry, electrolyte organization, and adsorption across operating conditions remain limited. Here we introduce a unified INTERFACE Force Field (IFF) parameterization together with a curated, ready-to-use pH-resolved surface model database that provides the most accurate and transferable atomistic description of major alumina phases to date. The framework covers  $\alpha$ -Al<sub>2</sub>O<sub>3</sub>,  $\gamma$ -Al<sub>2</sub>O<sub>3</sub>, boehmite, diaspore, and gibbsite using a single, physically interpretable parameter set that is directly compatible with CHARMM, AMBER, OPLS-AA, CVFF, and PCFF. Across structural, thermodynamic, mechanical, and interfacial benchmarks, simulations reproduce experimental reference data with >95% accuracy, exceeding existing force fields and the reliability of current density-functional approaches. A key advance is the first transferable treatment of surface ionization and charge regulation across alumina phases over a broad pH range, enabling simulations of realistic solid–electrolyte interfaces without phase-specific reparameterization. Quantitative reliability is demonstrated by reproducing zeta-potential trends and pH-dependent adsorption of a corrosion inhibitor at alumina–water interfaces. Predicted adsorption free energies and surface contact times correlate with experiments across more than an order of magnitude, enabling process-relevant screening and clarifying limitations of classical adsorption models. Relative to ML-DFT workflows, the approach is 100–1000 $\times$  faster and reaches system sizes and

time scales inaccessible to quantum methods. The results establish a predictive computational platform for designing alumina-containing catalysts, corrosion-resistant coatings, energy storage and biomaterials under realistic process conditions.

**Keywords:** Alumina, surface chemistry, molecular dynamics simulation, INTERFACE force field, corrosion, solid-electrolyte interfaces, aluminum oxide, aluminum oxyhydroxide, aluminum hydroxide, non-bonded models, coatings, surface protection

## 1. Introduction

Aluminum (Al) is the most abundant metal in the earth's crust, mostly in the form of bauxite, a mixture of aluminum oxides, hydroxides, and aluminosilicates.[1, 2] The oxides and hydroxides have versatile applications due to excellent mechanical, thermal, electrical, chemical, and biocompatible properties (Figure 1a-e).[3-6] The most common phases include  $\alpha$ -alumina ( $\alpha$ - $\text{Al}_2\text{O}_3$ ),  $\gamma$ -alumina ( $\gamma$ - $\text{Al}_2\text{O}_3$ ), diasporite ( $\alpha$ - $\text{AlO(OH)}$ ), boehmite ( $\gamma$ - $\text{AlO(OH)}$ ), and gibbsite ( $\text{Al(OH)}_3$ ) (Figure 1f-j). For example,  $\alpha$ -alumina is used for engineered ceramics due to wear resistance, for substrates in electronic circuits due to high thermal conductivity, as well as for prosthetics and implants due to biocompatibility.[7-9] The porosity of  $\gamma$ -alumina is suited for catalysts, catalyst supports, and adsorbents.[10-12] Nanostructures of aluminum oxide and hydroxides are also used as coatings on battery electrodes and separators,[13] for engineering drug delivery systems and advanced imaging systems,[14] as well as in reinforcements in polymer and

metal matrix composites.[7, 9] High purity  $\alpha$ -alumina (sapphire) is used in LEDs and optical lenses. Gibbsite is often included in fire retardants due to water release upon heating.[15] Gibbsite-rich bauxite rock is also a key source to produce aluminum metal with wide use due to low mass density, good ductility, and high electrical conductivity.[1, 2] The oxide and hydroxide phases then play a critical role in surface protection and as anti-corrosion coatings of Al and its alloys (Figure 1c).[16] Strength, stiffness, toughness, corrosion resistance, and physical appearance can be improved by alloying elements such as Cu, Si, Mg, Cr, and Ni.[17] Examples of major Al alloys include the 1xxx series to the 7xxx series,[18] as well as the 6xxx series with Si and Mg.[19]

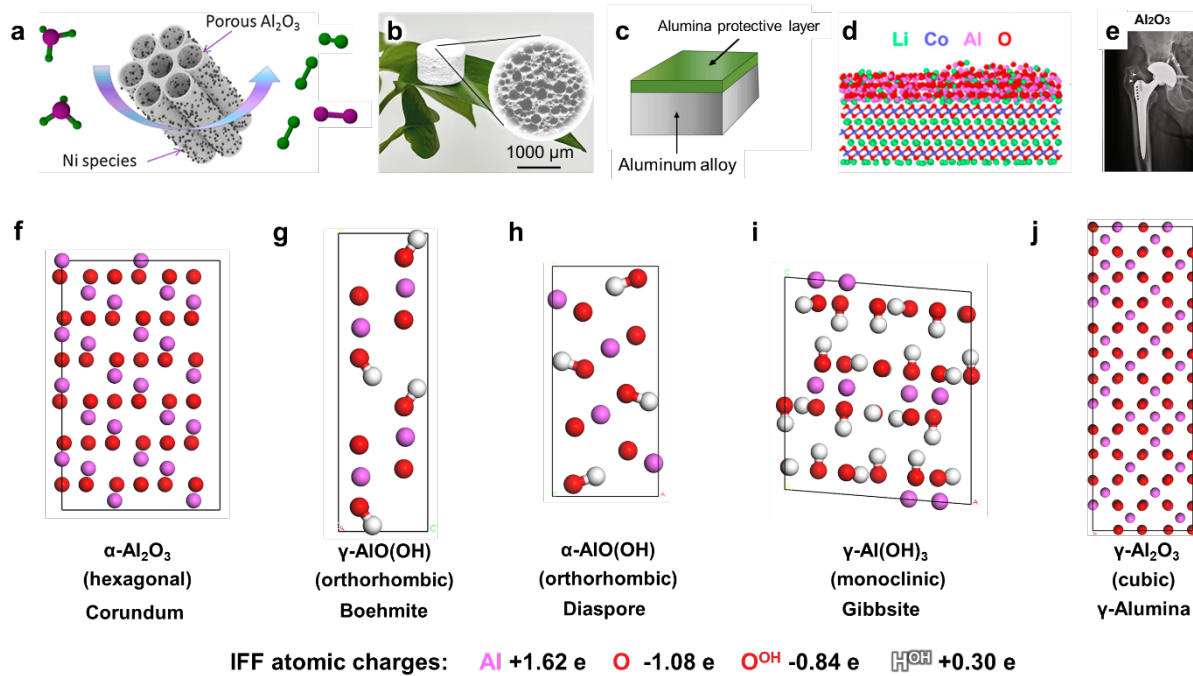


**Figure 1.** Common uses of aluminum oxide and hydroxide phases and their representation in the INTERFACE force field (IFF) for molecular simulations. Applications include (a) Catalyst supports (shown for ammonia decomposition),[6] (b) lightweight porous ceramics based on  $\text{Al}_2\text{O}_3$ , (c) Alumina protective layer on an aluminum alloy, (d) Li-Co-Al-O structure, (e)  $\text{Al}_2\text{O}_3$  in a bone structure, (f)  $\alpha\text{-Al}_2\text{O}_3$  (hexagonal) Corundum, (g)  $\gamma\text{-Al(OH)}$  (orthorhombic) Boehmite, (h)  $\alpha\text{-Al(OH)}$  (orthorhombic) Diaspore, (i)  $\gamma\text{-Al(OH)}_3$  (monoclinic) Gibbsite, and (j)  $\gamma\text{-Al}_2\text{O}_3$  (cubic)  $\gamma$ -Alumina.

protein foaming of precursors,[5] (c) coatings for corrosion protection, (d) coatings on electrodes and separators in metal ion batteries,[13] (e) implants with long lifetime and biocompatibility, such as hip prostheses.[4] We introduce the INTERFACE force field (IFF) and a surface model database for (f) hexagonal  $\alpha$ -aluminium oxide (corundum,  $\alpha\text{-Al}_2\text{O}_3$ ), (g) orthorhombic boehmite ( $\gamma\text{-AlO(OH)}$ ), (h) orthorhombic diaspore ( $\alpha\text{-AlO(OH)}$ ), (i) monoclinic gibbsite ( $\text{Al(OH)}_3$ ), and (j) cubic  $\gamma\text{-Al}_2\text{O}_3$ , extensible to mixed phases and dopants.[20] The models are based on nonbonded interactions and IFF atomic charges critical to reproduce bulk, surface, and reactive properties are shown below.

As Al alloys with enhanced corrosion resistance still suffer from pitting and stress-assisted corrosion,[21] various protective coatings such as oxide layers,[22] polymeric and silicone-based coatings,[23] powder coatings,[24] and Zn galvanizing[25] can provide long-term protection. Aluminum oxides ( $\text{Al}_2\text{O}_3$ ) are attractive protection coatings due high abundance, relatively low cost, chemical and thermal stability, relatively good strength, wear resistance, hardness, high melting point, and good electrical resistance.[26-28] Phase transitions between alumina phases as well as hydration and dehydration reactions (Figure 1a-e) can often be selectively realized by modulated treatment temperature.[29]

Given the widespread use of  $\text{Al}_2\text{O}_3$  and related compounds, it is important to understand, evaluate and predict structures and properties of pure, porous, and mixed phases, hydration reactions, as well as interactions with metals, oxides, solvents, molecules, polymers, and

biopolymers. Simulations can be faster and complement time-consuming experiments, reach all-atom resolution, and monitor reaction dynamics. At the same time, quantum mechanical and molecular simulations lack accurate, compatible parameters and realistic surface models of Al<sub>2</sub>O<sub>3</sub>-derived phases to address these problems. IFF parameters for several oxides and hydroxides including  $\alpha$ -Al<sub>2</sub>O<sub>3</sub> demonstrate 10 to 100 fold improvements in reliability in bulk and surface properties, beyond the accuracy of density functional theory (DFT) methods.[20] Bottlenecks of prior simulation approaches from DFT and generic models such as UFF and CLAYFF for Al<sub>2</sub>O<sub>3</sub> and oxyhydroxides include (1) lack of physical understanding of the parameters, (2) limited validation of bulk and interfacial properties, often with less than two types of comparisons to experimental measurements,[30-34] and (3) disregard of the pH-sensitive surface chemistry of alumina phases in contact with aqueous solutions. In addition, (4) prior force fields are also missing tests for multiple alumina-related phases and (5) have no demonstrated compatibility with parameter sets for solvents, organic molecules, and biopolymers such as CHARMM, AMBER, OPLS-AA, CVFF, and PCFF.

In this contribution, we introduce the INTERFACE force field (IFF) and a pH-resolved surface model database for alumina phases, aqueous interfaces, and organic hybrid materials, following consistent IFF-level validation of structural and interfacial properties.[35] At a theory level, IFF builds on interpretable representations of chemical bonding and charge distributions in inorganic and organic compounds, which have been developed for diverse chemistries across the periodic table and are extensible to new structures.[35, 36] IFF is a class I force field, including full class

II compatibility, and can be combined with the force fields CHARMM, AMBER, GROMOS, OPLS-AA, PCFF, and COMPASS without further parameter additions.[35, 37-40] IFF models and parameters have been thoroughly validated to reproduce chemical bonding, structural and interfacial properties in comparison to experimental reference data and theory, enabling quantitative simulations and predictions of multiphase assembly up to 1000 nm (see Section S1 in the Supplementary Material).[36, 41, 42]

As chemical bonding in alumina phases is approximately as ionic as covalent, we benefit from using nonbonded models, which eliminate additional groups of parameters for bonds, angles, and dihedrals that are part of bonded models (Figure 2). This treatment also avoids time-consuming modifications of the parameterization for each phase and facilitate the simulation of mixed oxides with minimal modifications.[20] For the simulation of aqueous interfaces at different pH values, adjustments in chemical composition and atomic charges are sufficient while we can retain the same force field types and remaining parameters.[20, 43] The new models overcome high uncertainties in earlier models and parameters,[30-33] introduce detailed surface chemistry,[34] and exceed the capabilities of DFT and DFT/ML approaches.[20] These models are necessary to enable trustworthy MD simulations of complex alumina hybrid materials for faster discovery of catalysts, analysis of corrosion processes, alumina hybrid materials and drug delivery systems.

We validate a series of bulk and surface properties of the alumina phases, including lattice parameters, (hkl) surface energies, bulk moduli, and contact angles relative to experimental reference data. As a sample application, we illustrate the simulation of electrolyte interfaces and

binding characteristics of the corrosion inhibitor p-hydrobenzoic acid in comparison to experimental adsorption isotherms.

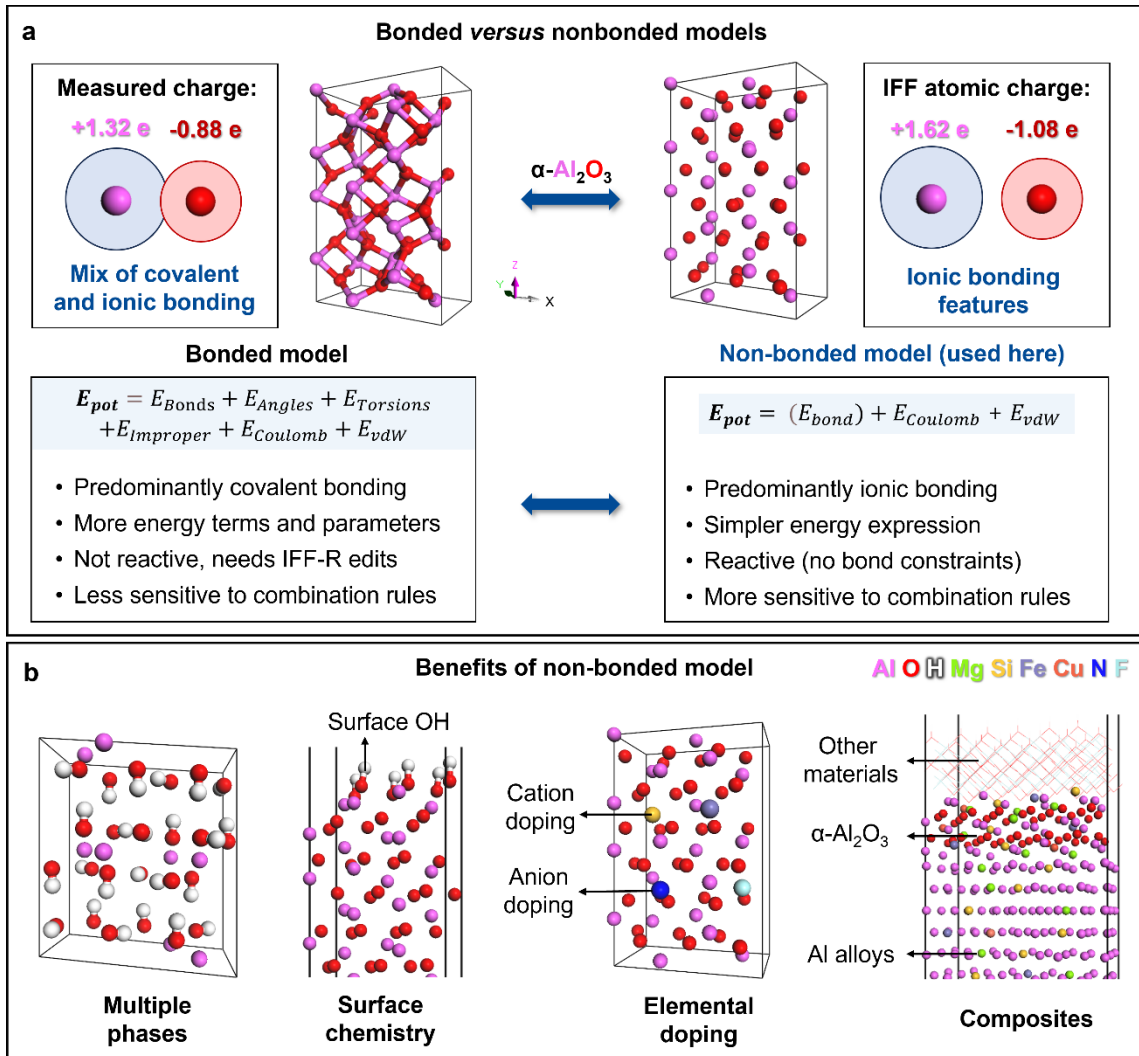


**Figure 2.** Bonded versus nonbonded alumina models, and the benefits of choosing nonbonded models here. (a) Atomistic representation of  $\alpha\text{-Al}_2\text{O}_3$  and atomic charges in both cases. The nonbonded model uses slightly higher atomic charges than the bonded model to account for residual covalent bonding contributions and requires far less constants (bond and angle parameters)

due to fewer energy terms. (b) Further benefits of the nonbonded models. We require no additional parameters to represent multiple phases, surface chemistry, doping, defects, and reactive interfaces. Both types of FF models are suited to represent surface chemistry, interfaces with electrolytes, organic molecules, and (bio)polymers.

## 2. Results and Discussion

### 2.1. Rationale for Non-Bonded Models

While Al atoms and O atoms in  $\text{Al}_2\text{O}_3$  have formal charges (oxidation states) of +3e for Al and -2e for O, chemical bonding is approximately half covalent by sharing valence electrons in Al-O bonds and half ionic.[44] The atomic charges are between +1.3e and +1.7e for all alumina and aluminum hydroxide species, allowing the use of bonded or nonbonded models (Figure 2a).[20, 44-46] Using nonbonded models has several advantages (Figure 2b):[20]

- (1) We utilize fewer parameters (atomic charge and LJ potential parameters), and only require bonded parameters for O-H bonds and  $\text{AlOH}_2^+$  bond angles;
- (2) We cover all phases of  $\text{Al}_2\text{O}_3$  and oxyhydroxides with one set of compatible IFF parameters;
- (3) We include critical surface chemistry across the range of pH values from 2 to 12 without the need for further angle and torsion parameters;
- (4) We achieve high accuracy of computed structural, interfacial, and mechanical properties, including doping, defects, and reactive composites.

Overall, the models simulate bulk and interfacial properties of  $\text{Al}_2\text{O}_3$  and oxyhydroxides with

an accuracy >95%. Further discussion of bonded versus nonbonded models is provided in Sections S2 and S3 in the Supplementary Material.[47]

## 2.2. IFF Energy Expression and Parameters

The force field parameters utilize the energy expressions supported by IFF.[35] We include additive terms for a harmonic bond stretching potential (for O-H bonds), a harmonic angle bending potential for protonated alumina species, Coulomb energy, and a Lennard-Jones potential with 12-6 and 9-6 options (Table 1):

$$E_{pot} = \sum_{ij \text{ bonded}} K_{r,ij} (r_{ij} - r_{0,ij})^2 + \sum_{ijk \text{ bonded}} K_{\theta,ijk} (\theta_{ijk} - \theta_{0,ijk})^2 + \frac{1}{4\pi\epsilon_0} \sum_{\substack{ij \text{ Coulomb} \\ (1,2 \text{ and } 1,3 \text{ excl})}} \frac{q_i q_j}{r_{ij}} + \sum_{\substack{ij \text{ nonbonded} \\ (1,2 \text{ and } 1,3 \text{ excl})}} \epsilon_{ij} \left[ \left( \frac{r_{min}}{r_{ij}} \right)^{12} - 2 \left( \frac{r_{min}}{r_{ij}} \right)^6 \right] \quad (1)$$

$$E_{pot} = \sum_{ij \text{ bonded}} K_{r,ij} (r_{ij} - r_{0,ij})^2 + \sum_{ijk \text{ bonded}} K_{\theta,ijk} (\theta_{ijk} - \theta_{0,ijk})^2 + \frac{1}{4\pi\epsilon_0} \sum_{\substack{ij \text{ Coulomb} \\ (1,2 \text{ and } 1,3 \text{ excl})}} \frac{q_i q_j}{r_{ij}} + \sum_{\substack{ij \text{ nonbonded} \\ (1,2 \text{ and } 1,3 \text{ excl})}} \epsilon_{ij} \left[ 2 \left( \frac{r_{min}}{r_{ij}} \right)^9 - 3 \left( \frac{r_{min}}{r_{ij}} \right)^6 \right] \quad (2)$$

The parameters include the harmonic bond stretching constants  $K_r$ , equilibrium bond lengths  $r_0$ , the harmonic angle bending constants  $K_\theta$ , equilibrium bond angles  $\theta_0$ , atomic charges  $q_i$ , equilibrium nonbond distances  $r_{min}$  (earlier also called  $r_0$  or  $\sigma_0$ ), as well as the nonbond potential well depth  $\epsilon$ . The bonded parameters  $K_r, r_0, K_\theta$ , and  $\theta_0$  represent the characteristics of covalent bonds in [Al O-H] groups or [Al OH<sub>2</sub><sup>+</sup>] groups in contact with aqueous solution (Figure

3). The two options in the potential energy expression differ in the LJ potential (Equations (1) and (2)). IFF parameters using the 12-6 Lennard-Jones potential[35] have full compatibility with CHARMM,[48] AMBER,[37] Dreiding,[49] CVFF,[50] OPLS-AA[40] force fields and include specific combination rules (IFF-CHARMM, AMBER, Dreiding with arithmetic mean for  $r_{min,ij}$  and Equation (1), IFF-CVFF, OPLS with geometric mean for  $r_{min,ij}$  and Equation (1)). IFF parameters using the 9-6 Lennard-Jones potential[35] are compatible with CFF,[51] PCFF,[52] and COMPASS[53] force fields and employ the Waldmann-Hagler combination (IFF-PCFF and Equation (2)). The nonbonded models are more sensitive to combination rules than bonded models since chemical bonding is entirely represented by Coulomb and Lennard-Jones interactions (Figure 2a).[20] Therefore, we utilize distinct IFF parameters for best compatibility with (CHARMM, AMBER, DREIDING), (CVFF, OPLS), and (PCFF, CFF, COMPASS).

The parameters for inner Al and O atoms of all alumina phases are identical to those of  $\alpha$ - $\text{Al}_2\text{O}_3$ .[20] Additions involve bulk and surface [Al<sub>2</sub> O-H] groups as well as protonated Al<sub>2</sub>OH<sub>2</sub><sup>+</sup> and deprotonated Al<sub>2</sub>O<sup>-</sup> surface groups with associated charge distributions (Figure 3). The atomic charges of +1.62e for internal Al and -1.08e for internal O atoms are at the high end of the physical range to represent predominantly ionic bonds and incorporate residual covalent contributions (Figure 3a). The values are consistent with experimental data from measurements of X-ray deformation electron densities, trends in atomization energy of Al compared to other elements, and trends in the first ionization energy of Al compared to other elements.[28, 44, 54-56] The atomization energy of Al, for example, is lower than for more covalent C and Si atoms, and higher

than for more ionic Na, Mg, and Mn atoms (Figure S1 in the Supplementary Material). Similar considerations apply to trends in first ionization energies (Figure S2 in the Supplementary Material). The charges are also consistent with electronegativity difference of 1.83 between O and Al, relative to similar chemistries with known atomic charges.[44]

Adjustments for  $\text{Al}_2\text{OH}$  surface groups based on pH value and (hkl) facets align with changes in chemical bonding during hydration, protonation, and deprotonation reactions of alumina phases as observed in measurements of contact angles, surface titration, zeta potentials, and pK values (Figure 3b). Hereby, the models benefit from chemical analogies with silica,[43] clay minerals,[45] hydroxyapatite,[57] and other metal hydroxide surfaces,[20] such as Al-OH, Si-OH, P-OH, Mg-OH, and Ca-OH groups, which have undergone extensive prior validation in IFF. The atomic charges in electroneutral  $\text{Al}_2\text{OH}$  groups are slightly higher in the bulk of hydroxide-containing minerals (-0.84e/+0.30e) than on  $\text{Al}_2\text{OH}$  terminated surfaces (-0.79e/+0.25e) due to higher internal polarity (Figure 3b and Figure S3 in the Supplementary Material). On protonated  $\text{Al}_2\text{OH}_2^+$  surface groups below the point of zero charge (typically pH < 8),[58-60] we maintain the oxygen charge of -0.79e of neat  $\text{Al}_2\text{OH}$  groups and only increase the H charges, which is necessary for structural stability of the surface (if bonded terms for Al-O were added, these charges would be lower). On deprotonated  $\text{Al}_2\text{O}^-$  surface groups, the  $\text{O}^-$  site retains a high charge of -1.26e, and the nearest two Al atoms only reduce their atomic charge to 1.48e for the same reason (Figure 3b). Our single set of atom types and parameters, along with the specific charge distribution, describes all major phases of aluminum oxides and hydroxides and requires no phase-specific modifications (Fig. 1f-

j). Models with pH-resolved aqueous surface chemistry including the  $\text{Al}_2\text{OH}$ ,  $\text{Al}_2\text{OH}_2^+$   $\text{Cl}^-$ , and  $\text{Al}_2\text{O}^- \text{Na}^+$  groups are necessary for realistic simulations of solid-electrolyte and inorganic-organic interfaces.

The parameters in the form of IFF-CHARMM, AMBER; IFF-CVFF, OPLS-AA; and IFF-PCFF, COMPASS are listed in Table 1 (see Section S4 in the Supplementary Material for a detailed interpretation).

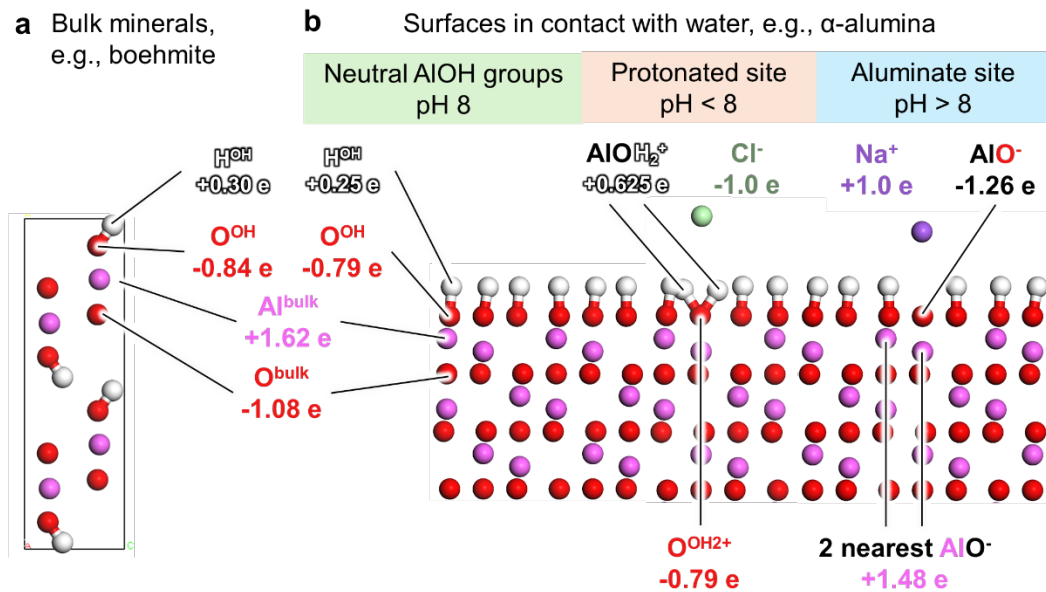


**Figure 3.** Atomic charges and atom types. We use one set of atom types for all bulk minerals and surfaces and small differences in atomic charges at surfaces. (a) Bulk mineral using the example of boehmite. Internal  $\text{Al}_2\text{OH}$  groups have an atom type  $\text{O}^{\text{OH}}$  for oxygen atoms with -0.84e charge and an atom type  $\text{H}^{\text{OH}}$  for hydrogen atoms with +0.30e charge. (b) Surface groups can be native to minerals or formed upon hydration. Surface  $\text{Al}_2\text{OH}$  groups have the same atom types  $\text{O}^{\text{OH}}$  and  $\text{H}^{\text{OH}}$ ,

but with reduced charges of  $-0.79e$  and  $+0.25e$ . Depending on pH value, further protonation or deprotonation may occur, leading to adjustments in local atomic charges without changes in atom types. The charge balance for electroneutral  $\text{Al}_2(\text{OH}_2)^+$   $\text{Cl}^-$  (pH < 8) and  $\text{Al}_2\text{O}^-$   $\text{Na}^+$  sites (pH > 8) is shown. Negative O charges at both types of surface sites are comparatively high to account for ionic and covalent bonding contributions and maintain structural stability.

**Table 1.** IFF parameters for alumina phases. Nonbonded parameters include partial atomic charges for all atom types (Figure 3) and Lennard-Jones (LJ) parameters. Bonded terms are applied to  $(\text{Al})\text{O-H}$  and  $(\text{Al})\text{OH}_2^+$  groups in the topmost layer of the surface, which interact with aqueous media across varying pH conditions.

Atomic charges	Al (e)	O <sup>bulk</sup> (e)	O <sup>OH</sup> (e)	H (e)
Same for all energy functions	Al: +1.62 In $\text{AlO}^-$ : +1.48 (2 Al closest to O <sup>-</sup> sites)	AlOH <sup>bulk</sup> : -0.84 AlOH <sup>surf</sup> : -0.79 AlOH <sub>2</sub> <sup>+</sup> : -0.79 AlO <sup>-</sup> : -1.26	AlOH <sup>bulk</sup> : 0.30 AlOH <sup>surf</sup> : 0.25 AlOH <sub>2</sub> <sup>+</sup> : 0.625	
LJ parameters	Al	O <sup>bulk</sup>	O <sup>OH</sup>	H <sup>OH</sup>
	$r_{min}$ (Å), $\epsilon$ (kcal/mol)	$r_{min}$ (Å), $\epsilon$ (kcal/mol)	$r_{min}$ (Å), $\epsilon$ (kcal/mol)	$r_{min}$ (Å), $\epsilon$ (kcal/mol)
IFF-CHARMM, AMBER	1.86, 0.1	3.54, 0.09	3.47, 0.122	1.085, 0.015 <sup>a</sup>
IFF-CVFF, OPLS	1.72, 0.45	3.3, 0.35	3.47, 0.122	1.085, 0.015 <sup>a</sup>

IFF-PCFF, COMPASS	1.81, 0.35	3.45, 0.2	3.47, 0.120	1.098, 0.013
<b>Bonded parameters</b>		<b>O–H bond</b>	<b>Angle (in <math>\text{AlOH}_2^+</math>)</b>	
Same for all energy functions		(Al) O-H: $r_0 = 0.945 \text{ \AA}$ $K_r = 495 \text{ kcal}/(\text{mol}\cdot\text{\AA}^2)$	NA $\theta_0 = 109.47^\circ$ $K_\theta = 50 \text{ kcal}/(\text{rad}\cdot\text{\AA}^2)$	
		(Al) O-H <sub>2</sub> <sup>+</sup> : $r_0 = 1.000 \text{ \AA}$ $K_r = 540.6 \text{ kcal}/(\text{mol}\cdot\text{\AA}^2)$		

<sup>a</sup> Alternatively, simpler H parameters in OH groups of 0.001, 0.001 can be used with less than 5% change in interfacial properties.

### 2.3. Validation of the Lattice Parameters, Surface Energy, and Bulk Modulus

The non-bonded models allow an excellent representation of the structural and interfacial properties of  $\text{Al}_2\text{O}_3$  and oxyhydroxide compounds (Figure 4 and Tables S1 to S6 in the Supplementary Material). Average deviations from experimental data are 0.8% in lattice parameters (2.1% in density), 4% in surface energies, and 7% in bulk modulus (for 12-6 LJ potentials), plus agreement in contact angles.

For  $\alpha$ -alumina, lattice vectors and angles are almost identical to experimental values with average deviations less than 0.15%. The root mean squared displacement (RMSD) of the atoms during simulations was about 0.15  $\text{\AA}$ , and the density matches experiments within 0.1% relative to XRD data of 3.984  $\text{g}/\text{cm}^3$  (Figure 4a and Table S1 in the Supplementary Material).[61] The (0001) surface energy of  $1.65 \pm 0.05 \text{ J}/\text{m}^2$  is reproduced within error bars,[62] and the (11 $\bar{2}$ 0) surface

energy was computed to be slightly higher at  $1.88 \text{ J/m}^2$  (Figure 4b, Figure S4 and Table S1 in the Supplementary Material). Experimental measurements suggest a bulk modulus of  $254 \text{ GPa}$ ,[63, 64] which IFF MD simulations reproduce within 4-8%, except for IFF-PCFF which is less recommended than CHARMM, AMBER, CVFF, and OPLS-AA compatible parameters for mechanical properties (Figure 4c).[20] Detailed elastic constants for  $\alpha\text{-Al}_2\text{O}_3$  are also reproduced well in MD simulations (Table S6 in the Supplementary Material). Notably, the simulated shear modulus is  $155 \text{ GPa}$ , which only deviates 6% from the experimental value  $165 \text{ GPa}$ , and the computed Poisson ratio of 0.26 is close to the experimental measurement of 0.24.[63]

For boehmite, the computed lattice parameters deviate on average by about 1% and RMSD deviations are  $\sim 0.5 \text{ \AA}$  in a  $25 \text{ \AA}$  supercell. The definition of the structures is thus excellent (Figure 5a). The density in MD simulations matches experimental values within 0.5%, except for IFF-CHARMM, AMBER with 3% deviation (Figure 4a and Table S2 in the Supplementary Material). Computed (001) surface energies match likely values of  $\sim 0.9 \text{ J/m}^2$  within 5% while the cleavage plane of lowest energy is (010), terminated by  $\text{Al(OH)}$  groups on both sides (Figure 1g), with  $0.20 \pm 0.04 \text{ J/m}^2$  surface energy (Figure 4b and Table S2 in the Supplementary Material). The experimental bulk modulus is somewhat uncertain to-date, with most likely values of  $100 \pm 10 \text{ GPa}$ . MD simulations with 12-6 LJ potentials yield values of 95 and 100 GPa (70 GPa for PCFF) in excellent agreement, consistent with excellent lattice parameters and surface energies (Figure 4c and Table S2 in the Supplementary Materials).

Diaspore showed overall  $\sim 2\%$  deviation in lattice parameters and up to several percent in

individual values (Figure 4a and Table S3 in the Supplementary Material). Computed densities agree within 1-3% of experimental data, and the structural fidelity is very high (Figure 5b). The (001) surface energy was computed as  $\sim 1.25 \text{ J/m}^2$ , similar to the (100) surface energy of  $\sim 1.20 \text{ J/m}^2$  (Figure 4b). The experimental bulk modulus of approximately 120 GPa was computed around 110 GPa, except for IFF-PCFF (86 GPa) which routinely leads to underestimations (Figure 4c and Table S3 in the Supplementary Material).

Computations on gibbsite ( $\gamma\text{-Al(OH)}_3$ ) achieved excellent reproduction of the lattice parameters with average deviations  $< 1\%$ , including the monoclinic cell angle, and deviations in density of 2-4% (Figure 4a and Table S4 in the Supplementary Material).  $\gamma\text{-Al(OH)}_3$  stands out as a highly hydrous mineral with 2D OH layers that coordinate Al layers in alternation (Figure 1i), are easily displaced and known to form perfect (001) cleavage planes with a computed surface energy of  $0.28 \pm 0.03 \text{ J/m}^2$  (Figure 4b). The value aligns with the presence of densely packed OH groups at the interface and is equal to about 4x the surface tension of liquid water ( $72 \text{ mJ/m}^2$ ). The bulk modulus is expected to be between 30 and 35 GPa according to experimental data at low pressures, and computed values agree within this range, except a lower value for IFF-PCFF (Figure 4c and Table S4 in the Supplementary Material). As a result of the hydrous nature and associated lower cohesion, the  $\text{Al(OH)}_3$  layers are easily displaced and simulation cells of  $69.472 \times 60.936 \times 58.233 \text{ \AA}^3$  size or larger where required to maintain stable structures in MD simulations (Figure S5 in the Supplementary Material).

$\gamma\text{-Al}_2\text{O}_3$  is a distinctively disordered cubic phase with a well-defined oxygen lattice and

random occupancy of vacancies by Al (32 O sites and 119 fractionally occupied Al sites).[65] Stoichiometric models for simulations require a supercell that consists of at least 3 unit cells, such as  $3 \times 1 \times 1$  ( $23.815 \times 7.938 \times 7.938 \text{ \AA}^3$ ). The  $\gamma$ -Al<sub>2</sub>O<sub>3</sub> model then includes 64 Al atoms in random positions along with 96 O atoms in well-defined positions (Figure S6 in the Supplementary Material). The lattice parameters are reproduced in excellent agreement with experimental data, showing average deviations of 0.4%, and the density agrees within  $\sim 2.5\%$  (Figure 4a and Table S5 in the Supplementary Material). Some rearrangements of Al atoms among the fractionally occupied lattice sites were seen during molecular dynamics, along with high structural stability of the O lattice (Figure S7 in the Supplementary Material). The (001) surface energy is  $1.66 \pm 0.1 \text{ J/m}^2$  according to measurements,[66] identical to  $\alpha$ -Al<sub>2</sub>O<sub>3</sub> within the uncertainty, and reproduced within 4% in molecular simulations (Figure 4b). The bulk modulus of 162 GPa is also reproduced by simulations, although with some scatter between the CVFF and CHARMM versions (Figure 4c and Table S5 in the Supplementary Material).

The data further show that higher mass density correlates with higher surface energy and higher bulk modulus (Figure 4a-c). Disordered ( $\gamma$ -Al<sub>2</sub>O<sub>3</sub>) and hydrated minerals (boehmite, diaspore, gibbsite) have lower densities than  $\alpha$ -Al<sub>2</sub>O<sub>3</sub>, and surfaces terminated with OH groups (boehmite, diaspore, gibbsite) possess lower surface energy than anhydrous surfaces ( $\alpha$ -Al<sub>2</sub>O<sub>3</sub> and  $\gamma$ -Al<sub>2</sub>O<sub>3</sub>). As previously described, [35] bulk moduli often correlate with surface energies as they are derivatives of the surface energy with respect to displacement of the bounding surfaces. IFF strongly outperforms prior force fields (Pedone,[20, 67] CLAYFF,[20, 68, 69] UFF,[20, 70]

ReaxFF[20, 71, 72]) and often DFT calculations,[20] providing the simplest, most compatible and transferable tool. Specifically, Pedone cannot provide surface and interfacial properties, CLAYFF has deviations in lattice parameters and densities of 5-10% and mismatches of ~30% in surface energy, including boehmite and gibbsite,[20, 68, 69] and UFF has extreme uncertainties on the order of 100%.[20, 70] ReaxFF performance is variable, depending on parameterization, typically with 5-10% deviations in lattice parameters, 50% error in surface energy, and 10-20% in bulk moduli.[20, 71, 72] DFT simulations commonly have 3-4% errors in lattice parameters and density, ~25% errors in surface energy, and ~15% uncertainty in bulk modulus, all of which are higher than in IFF simulations of the alumina phases (~2%, 4%, and 7% using 12-6 LJ).[20]

In summary, the single set of interpretable parameters for alumina phases in IFF reproduces key features of chemical bonding, structural and energetic properties in outstanding agreement with experimental reference data. The performance is independent of the force field sub-class used (IFF-CHARMM, AMBER; IFF-CVFF, OPLS-AA; IFF-PCFF, COMPASS) and the simulation software used (LAMMPS, NAMD, GROMACS, OpenMM, Forcite/Materials Studio). For best predictions of mechanical properties, the 12-6 LJ versions are preferred over 9-6 LJ versions. From neat oxide and mixed hydroxides to the hydrous  $\text{Al(OH)}_3$  and structurally disordered  $\gamma$ -alumina phases, IFF outperforms prior force fields and often DFT calculations, providing the simplest, most compatible and transferable parameters.

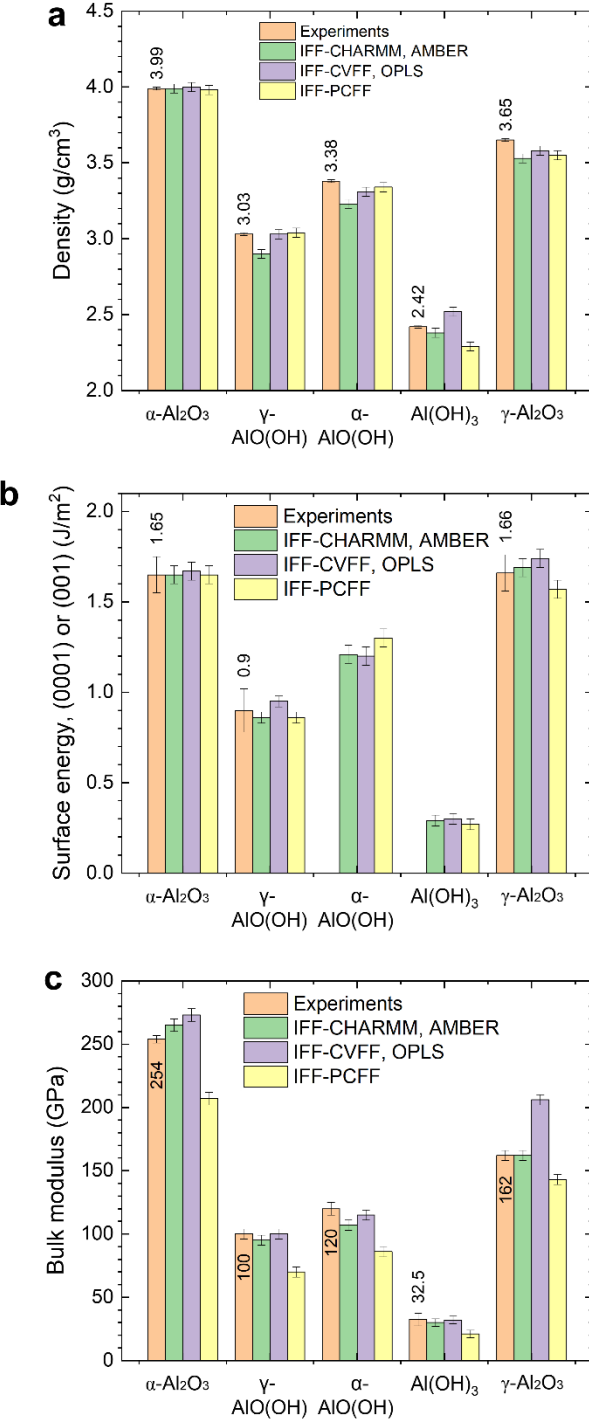


**Figure 4.** Validation of IFF for the 5 alumina phases shows excellent agreement of computed bulk and surface properties with experimental reference data. (a) Densities (2.1% average deviation). (b) Surface energies of the (0001) plane (corundum) and (001) planes of other phases (4.0% average deviation). (c) Bulk modulus (3.5% average deviation).

average deviation). (c) Bulk modulus (7% average deviation for 12-6 LJ). The close agreement demonstrates universality and compatibility of non-bonded IFF parameters for different phases of aluminum oxides and hydroxides. IFF-PCFF with 9-6 LJ options is less preferred than the other options due to less accurate representation of mechanical properties. Details of lattice parameters, surface energies, mechanical properties, and references to experimental data are given in Tables S1 to S5 in the Supplementary Material.

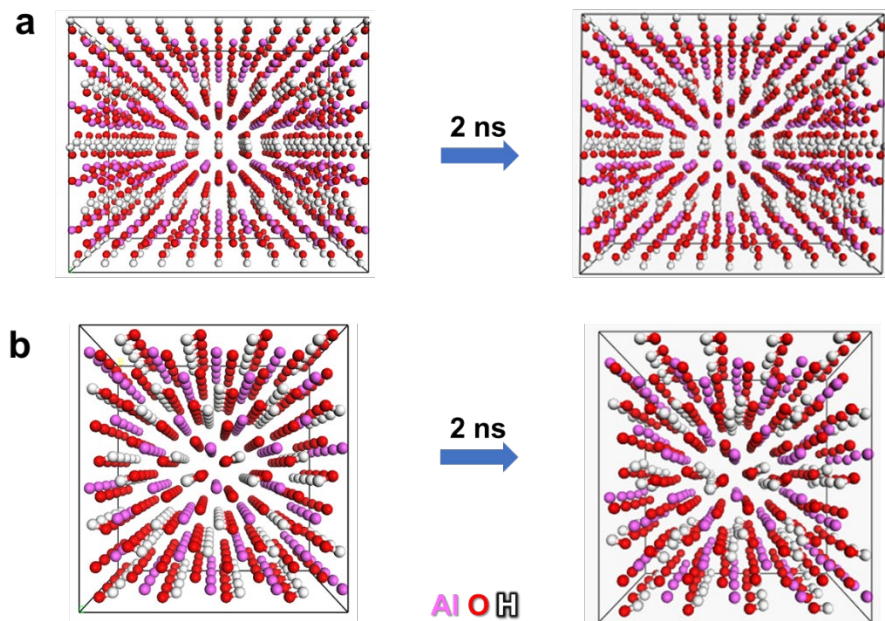


**Figure 5.** Visualization of the structural stability during IFF MD simulations (IFF-CVFF) for boehmite and diasporite. Starting and equilibrated structures after 2 ns are shown in perspective view. (a) Boehmite ( $\gamma$ -AlO(OH)) with a box size of  $28.760 \times 24.480 \times 14.836 \text{ \AA}^3$ . (b) Diasporite ( $\alpha$ -AlO(OH)) structures with a box size of  $17.604 \times 18.842 \times 14.225 \text{ \AA}^3$ . Examples for other phases

are included in the Supplementary Material.

## 2.4. Validation of Aqueous Interfacial Properties

$\alpha$ -Al<sub>2</sub>O<sub>3</sub> undergoes surface hydration in water to form a molecularly thin Al(OH)<sub>3</sub> overlayer similar to gibbsite (Figure 6a).[73] The contact angle of clean hydrated alumina surface is 0° in experiments[74] and we consistently obtain 0° in IFF MD simulations (Figure 6a and Figures S8 to S11 in the Supplementary Material). We used the flexible SPC water model, or the TIP3P model which lead to a negligible difference.[20, 43] The water interfacial properties from MD simulations were then further compared with experimental data from crystal truncation rod (CTR) diffraction, which enable accurate determinations of the atomic layer positions near the surface, which include contractions relative to the bulk layer spacing (Figure 6b, c).[73] The average layer spacing between the O atoms of the adsorbed water molecules (denoted as O<sup>Wat</sup>) from the terminal O layers on the hydrated  $\alpha$ -Al<sub>2</sub>O<sub>3</sub> (0001) surfaces (O<sup>OH</sup>) is 2.30 Å in measurements versus ~2.5 Å in MD simulations (Figure 6b, c).[73] The complete water structure at the interface can be seen from MD simulation and the computed radial distribution functions (Figure 6d, e). Accordingly, the water layers are disordered and the first peak ranges from 2.4 Å to 3.5 Å. The expansion of interfacial Al<sup>sur</sup>-O<sup>OH</sup> and Al<sup>sur</sup>-O<sup>bulk</sup> atomic layer distances is correctly captured in MD simulations. Specifically, the 1.01 Å and 0.97 Å distances in layers 2-3 and 4-5 are larger than 0.84 Å in lower inner layers (layers 7-8 and 8-9) in CTR measurements (Figure 6b). MD simulations yield distances of 1.00 Å and 0.95 Å for layers 2-3 and 4-5, as well as 0.87 Å for layers 7-8 and 8-9,

showing excellent agreement (Figure 6c). Also,  $\text{Al}^{\text{sur}}\text{--}\text{Al}^{\text{sur}}$  atomic layer distances are compressed to 0.23 Å compared to  $\text{Al}^{\text{bulk}}\text{--}\text{Al}^{\text{bulk}}$  distance of 0.49 Å according to CTR measurements,[73] and we consistently obtain 0.29 Å and 0.49 Å in MD simulations (layers 3-4 and 6-7 in Figure 6b, c). Overall, the  $\alpha\text{-Al}_2\text{O}_3$  (0001) surface models show high accuracy in reproducing the measured atomic layer distances with an average deviation of  $\sim$ 4%, including superficial expansion and compression of atomic layers. Radial distribution functions between the surface oxygen atoms and water oxygen atoms also show the distribution of further water layers (Figure 6d, e). The layers are centered near 3.2, 4.7, 6.8, and weakly at 8.7 Å before approximating the bulk structure of water.

The (hkl) wetting properties of other alumina phases such as  $\gamma\text{-Al}_2\text{O}_3$ , gibbsite, boehmite and diaspore involve similar hydration reactions leading to local gibbsite overlayers. Vice versa, all alumina phases convert to  $\alpha\text{-Al}_2\text{O}_3$  upon heating via dehydration and reconstruction, respectively (Figure S12 in the Supplementary Material).

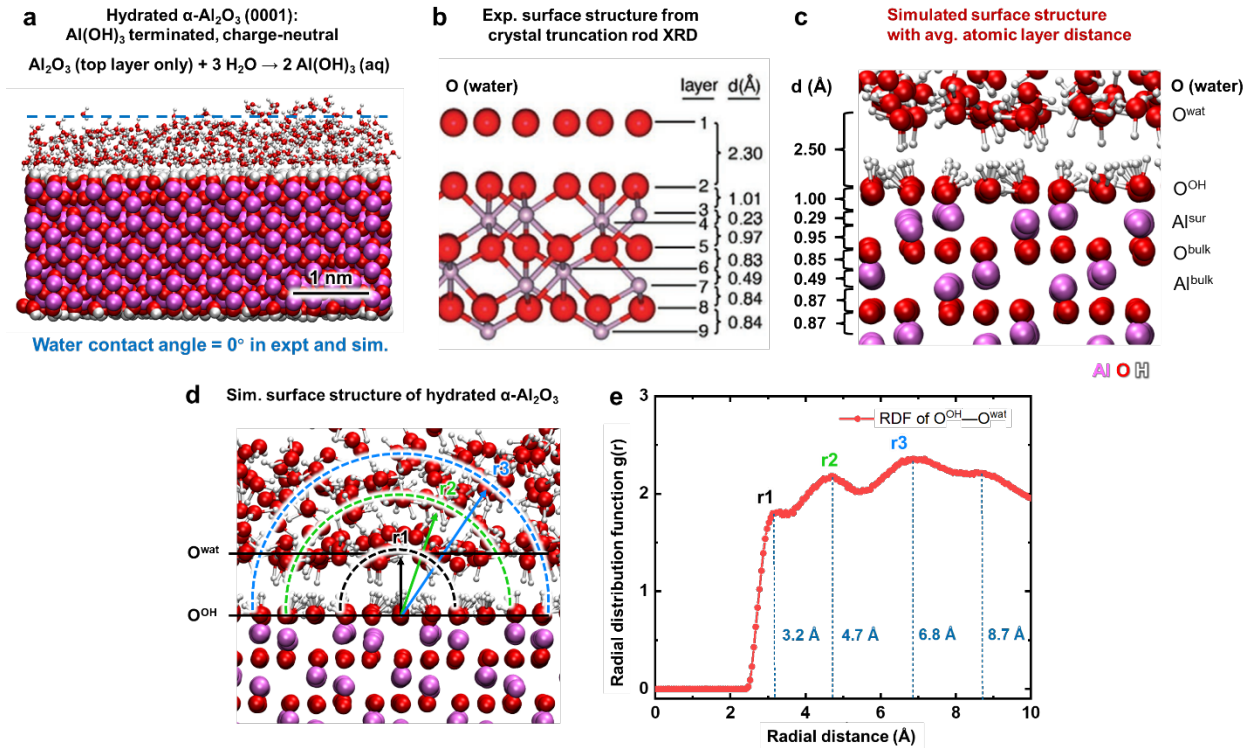


**Figure 6.** Interfacial water structure of hydrated  $\alpha$ - $\text{Al}_2\text{O}_3$  (0001). (a) The cleaved surface reacts with water to form a superficial monolayer of gibbsite,  $\text{Al(OH)}_3$ . The simulated water contact angle of  $0^\circ$  agrees with experimental measurements of  $0^\circ$ .[74] (b) Experimentally measured atomic layer distances from crystal truncation rod (CTR) diffraction.[73] (c) The simulated atomic layer distances as a time average over 5 nanoseconds align with the experimental data, including surface-specific expansions of  $\text{Al}^{\text{sur}}-\text{O}^{\text{OH}}$  distances and contractions of  $\text{Al}^{\text{sur}}-\text{Al}^{\text{sur}}$  distances. (d) MD Simulations also reveal the location of hydrogen atoms and dynamics of the water interfaces. (e) Radial distribution functions between O atoms on the surface and in bulk water show the formation of distinct layers. IFF-CHARMM parameters were used.

## 2.5. Surface Model Database as a Function of pH Value in Aqueous Solution and Electrolyte

## Dynamics

The surface chemistry is variable depending on the phase of alumina chosen and the pH value in solution.[58, 59] We provide a surface model database for common (hkl) cleavage planes of the five alumina phases in vacuum, which include both the surface structure prior to hydration and after exposure to electrolytes (Table 2, Table S7 and Supplementary Files in the Supplementary Material). Upon full hydration, all phases and nanoparticles of alumina form a hydrated gibbsite-like  $\text{Al}(\text{OH})_3$  layer on the surface, [73, 75] which is sensitive to the pH value in the electrolyte and requires appropriately ionized surface models (Figures 7 and 8). The surface model database contains hydrated and ionized surface models for pH values from 2 to 12 based on surface titration measurements for the examples of  $\alpha\text{-Al}_2\text{O}_3$  (0001) and  $\gamma\text{-Al}(\text{OH})_3$  (001) surfaces. These features have not been systematically incorporated in prior models so that earlier simulation studies often led to qualitatively different or unphysical results.

**Table 2.** Guide to IFF surface models of alumina phases and common (hkl) planes after cleavage, hydration, and exposure to electrolytes as a function of pH values. Upon hydration, all surfaces feature a gibbsite-like  $\text{Al}(\text{OH})_3$  layer with an area density of OH groups between 13.5 per  $\text{nm}^2$  (gibbsite) and 15.5 per  $\text{nm}^2$  (corundum) at the point of zero charge of  $\text{pH} \sim 8$ . In contact with aqueous electrolytes, the surfaces undergo ionization as a function of the pH value across a wide range of positive to negative charge.

Alumina phase and (hkl) surface	Surface termination in vacuum	Surface termination upon hydration at pzc	pH value in solution	Surface ionization (e/nm <sup>2</sup> ) <sup>a</sup>	Percent of ionic OH surface groups
$\alpha$ -Al <sub>2</sub> O <sub>3</sub> (0001), (10-10), (11-20)	Al or O	Al(OH) <sub>3</sub>	2	+1.75 $\pm$ 0.1	$\sim$ 12% OH <sub>2</sub> <sup>+</sup>
$\gamma$ -Al <sub>2</sub> O <sub>3</sub> (001)	Al and O		5	+0.9 $\pm$ 0.1	$\sim$ 6% OH <sub>2</sub> <sup>+</sup>
$\alpha$ -AlOOH (100), (010), (001)	O and OH		8.1 $\pm$ 0.5	0 $\pm$ 0.1	$\sim$ 0% (OH only)
$\gamma$ -AlOOH (100), (010)	O and OH		10	-0.75 $\pm$ 0.1	$\sim$ 5% Al <sub>2</sub> O <sup>-</sup>
$\gamma$ -Al(OH) <sub>3</sub> (001)	Al(OH) <sub>3</sub>		12	-1.5 $\pm$ 0.1	$\sim$ 10% Al <sub>2</sub> O <sup>-</sup>

<sup>a</sup> Based on experimental data from surface titration and zeta potential measurements in refs. [58, 59].

In deriving these surface models, we combine knowledge of surface chemistry,[76, 77] acid-base concepts, zeta potential measurements,[60, 78, 79] and quantitative surface titration data.[58, 59] The gibbsite-like hydrated alumina surfaces[73, 75] are prone to protonation and deprotonation reactions (Figure 7a).[76, 77] Zeta potential measurements[60] and surface titration

measurements[58, 59] have characterized the surface charge density as a function of pH value, indicating a point of zero charge (pzc) at pH  $\sim 8.1 \pm 0.5$  for  $\alpha$ -alumina and  $\gamma$ -alumina. Earlier studies also report a broader range of the pzc between pH 7 and 9. Protonated surfaces with  $[\text{Al}_2 \cdots \text{OH}_2^+]$  groups are present at pH  $< 8$  (Figure 7b) and begin to dissolve into  $\text{Al}^{3+}(\text{aq})$  species at pH values below 4.5. At pH  $> 8$ , we find deprotonated surfaces with  $[\text{Al}_2 \cdots \text{O}^-]$  groups (Figure 7b) that begin to dissolve into  $\text{Al}(\text{OH})_4^-$  ions at pH values above 9.4.[59] The presence of  $\text{Al}(\text{OH})_3$  overlayers,  $[\text{Al}_2 \cdots \text{OH}_2^+]$  and  $[\text{Al}_2 \cdots \text{O}^-]$  surface groups, rather than geminal  $\text{Al}_2(\text{OH})_2^-$  groups, is supported by XPS[75] and FTIR studies.[80, 81] The coordination environment of the superficial  $\text{OH}_2^+$ ,  $\text{OH}$ , and  $\text{O}^-$  species involves two nearest Al neighbors through a 3-center coordination bond (Figure 7b, c-e). This geometry is distinctly different, for example, from SiOH groups on silica surfaces with localized Si-OH bonds[43] and reflects the increased ionic character in alumina species. We represent these chemistries and coordination environments in the nonbonded models by adjusting the atomic charge distribution and adding the necessary counter ions on the surface layers for charge neutrality (Figure 7c and Section S4 in the Supplementary Material). The ions can be exchanged for other ions or buffer ions that control the pH value.

The IFF alumina surface model database incorporates experimental surface titration data (Figure 8a, Table 2, Figure S13 and Table S7 in the Supplementary Material)[58, 59] to quantitatively represent the amount of protonated and deprotonated sites. The area density of OH groups on hydrated (0001)  $\alpha$ -alumina and on (001) gibbsite surfaces is 15.3 per nm<sup>2</sup> and 13.6 per nm<sup>2</sup> at the point of zero charge, respectively (Figure 8b). Across the pH spectrum from 2 to 12, the

surface charge density ( $\sigma$ ) ranges from approximately  $+1.75 \text{ e/nm}^2$  to 0 at pH  $\sim 8$ , and then from 0 to  $-1.5 \text{ e/nm}^2$  (Figure 8a-c). The drastic changes in (hkl) surface chemistry of the alumina phases in contact with aqueous electrolytes require specifically designed models at a given pH value for predictive simulations (Figure 8b, c). Positive ionization or negative ionization up to about 1.5 groups per  $\text{nm}^2$  with  $\pm 1.5$  elementary charges per  $\text{nm}^2$  equals to ionization of up to  $\sim 10\%$  of all OH groups (Figure 8c and Table 2). The precise surface charge density also depends on the electrolyte composition and concentration (Figure S13 in the Supplementary Material).[58] We assume NaCl solution between 0.0 to 0.5 M concentration, and customization to other electrolytes can be made as needed.

The charge density exceeds that of silica surfaces, which have been extensively studied in experiments and included in IFF, albeit around a different pzc (8 for alumina vs 3 for silica).[43, 82, 83] The wide range of alumina surface charge drastically changes the type of species attracted, for example, molecules with R-COO<sup>-</sup> groups vs R-NH<sub>3</sub><sup>+</sup> groups, their binding affinity, packing density, and self-assembly. Utilizing adequate surface models is thus critical regardless of the simulation method employed.

Our IFF guidance can be applied to all alumina phases in contact with electrolytes as they exhibit similar surface chemistry and point of zero charge (Table 2).[60, 75] The workflow to construct customized models of surfaces or nanoparticles with a specific surface charge density is as follows: (1) Build a model of the nanostructure or (hkl) surface with full (or partial) hydration, e.g., charge-neutral Al(OH)<sub>3</sub> termination, including correct atom types and charges. (2) According

to the desired pH value, decide on the type and area density of ionized surface groups (Table 2, Figure 8c, Figure S13 and Table S7 in the Supplementary Material). (3) Build a model of sufficient size and identify a statistical distribution of the charged sites (Figure S14 in the Supplementary Material). (4) At the identified sites, add or remove atoms, adjust the atomic charges and modify the atom types as needed (Figure 7c). (5) Double check for charge neutrality and correct, stoichiometric modifications made.

To illustrate the effect of the pH-dependent surface chemistry on the structure of the electrolyte at the solid-liquid interfaces, we computed the density profiles of water, sodium ions, and chloride ions at pH values of 2, 5, 8, 10, and 12 (Figure 8d, e). The water density profile indicates major peaks at 2.5 Å and 5.8 Å away from superficial Al-bound O atoms, as well as a minor 3<sup>rd</sup> peak near 8.8 Å (Figure 8d inset). The water density profile was not affected by the pH value in a major way since ionization rarely surpasses 15% of AlOH groups (Table 2). At low pH values of 2, the major share of superficial chloride ions remains bound to the AlOH<sub>2</sub><sup>+</sup> groups and only 13% dissociate, however, at pH values of 5, 45% or ~0.4 Cl<sup>-</sup> ions per nm<sup>2</sup> dissociate more than 5 Å away from the surface (Figure 8e and Table S8 in the Supplementary Material). A small fraction of Cl<sup>-</sup> ions is even found up to 20 Å away from the alumina surface. Thus, a pH value close to the pzc of 8 results in dissociation of a higher fraction of ions from the surface than pH values further away from the pzc. This trend is related to a lower overall surface charge per unit area and consistent with a steep onset of the positive zeta potential in experiments near the pzc, while the curve flattens at pH values further away from the pzc.[78, 79] A similar trend is seen at high pH

values for the dissociation of  $\text{Na}^+$  ions (Figure 8d and Table S8 in the Supplementary Material).

Hereby, the negative surface charge at high pH is more concentrated on singular O atoms, as opposed to delocalization of the positive charge over two H atoms and one O atom at low pH, and sodium ions are smaller than chloride ions. Therefore,  $\text{Na}^+$  ions are more strongly bound and only about 10% dissociate more than 5 Å away from the surface. Consistently, the negative zeta potential at high pH values tends to be smaller than the positive zeta potential for the same amount of positive surface charge at low pH values in the absence of other added electrolytes (-25 to -40 mV at high pH vs. +30 to +80 mV at low pH).[78, 79]

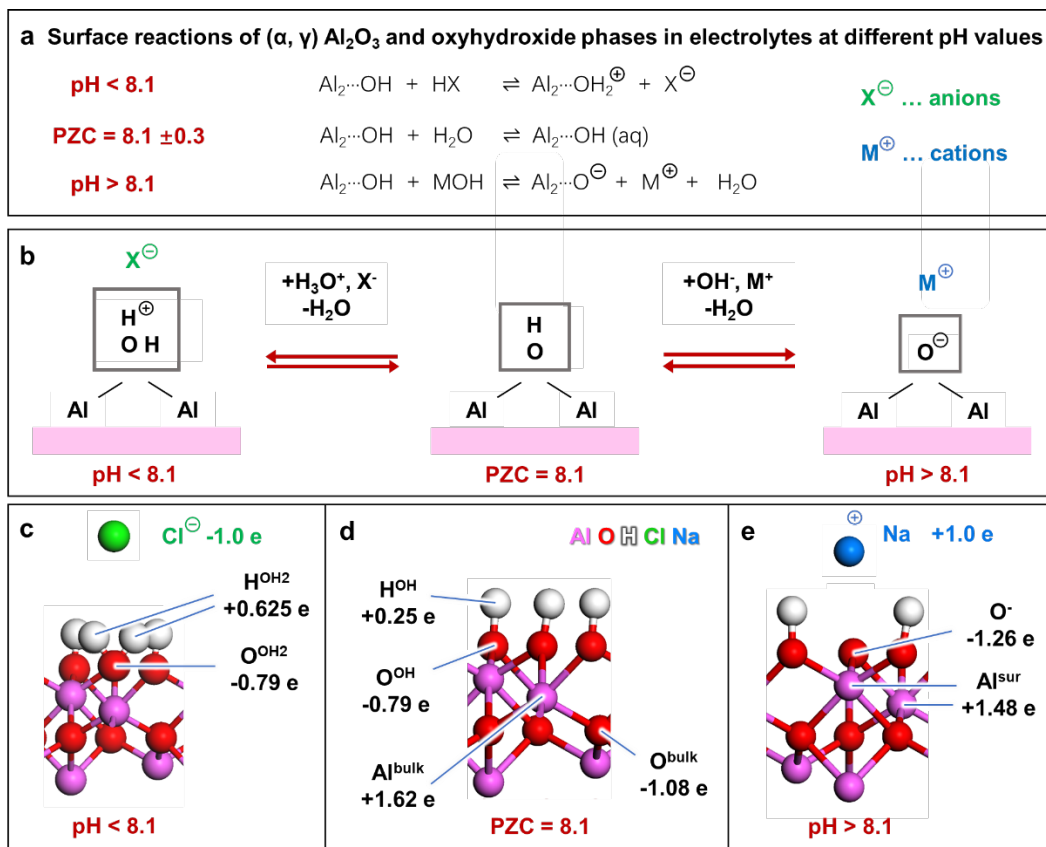


**Figure 7.** Surface chemistry of alumina and oxyhydroxide phases at different pH values. (a)

Hydration of minerals leads to formation of superficial gibbsite layers with  $\text{Al}_2\text{OH}$  surface groups. These layers are charge-neutral at the point of zero charge at pH  $\sim 8.1$ . The  $[\text{Al}_2 \cdots \text{OH}]$  groups undergo protonation reactions at lower pH values and deprotonation reactions at higher pH values.[58, 59] (b) Illustration of the chemical environment of surface terminal groups. Terminal oxygen species have two nearest neighbor Al ions rather than localized Al-OH bonds. (c-e) Representation in IFF atomistic models, for the example of a hydrated  $\alpha\text{-Al}_2\text{O}_3$  (0001) surface, including modifications of atomic charges. Al-O bonds are shown to illustrate spatial relationships in the partially covalent bonds. Atomic charges of the neutral OH-terminated surface (d) are modified locally for  $\text{OH}_2\text{Cl}$  defects (c) and  $\text{Al}_2\text{ONa}$  defects as indicated.

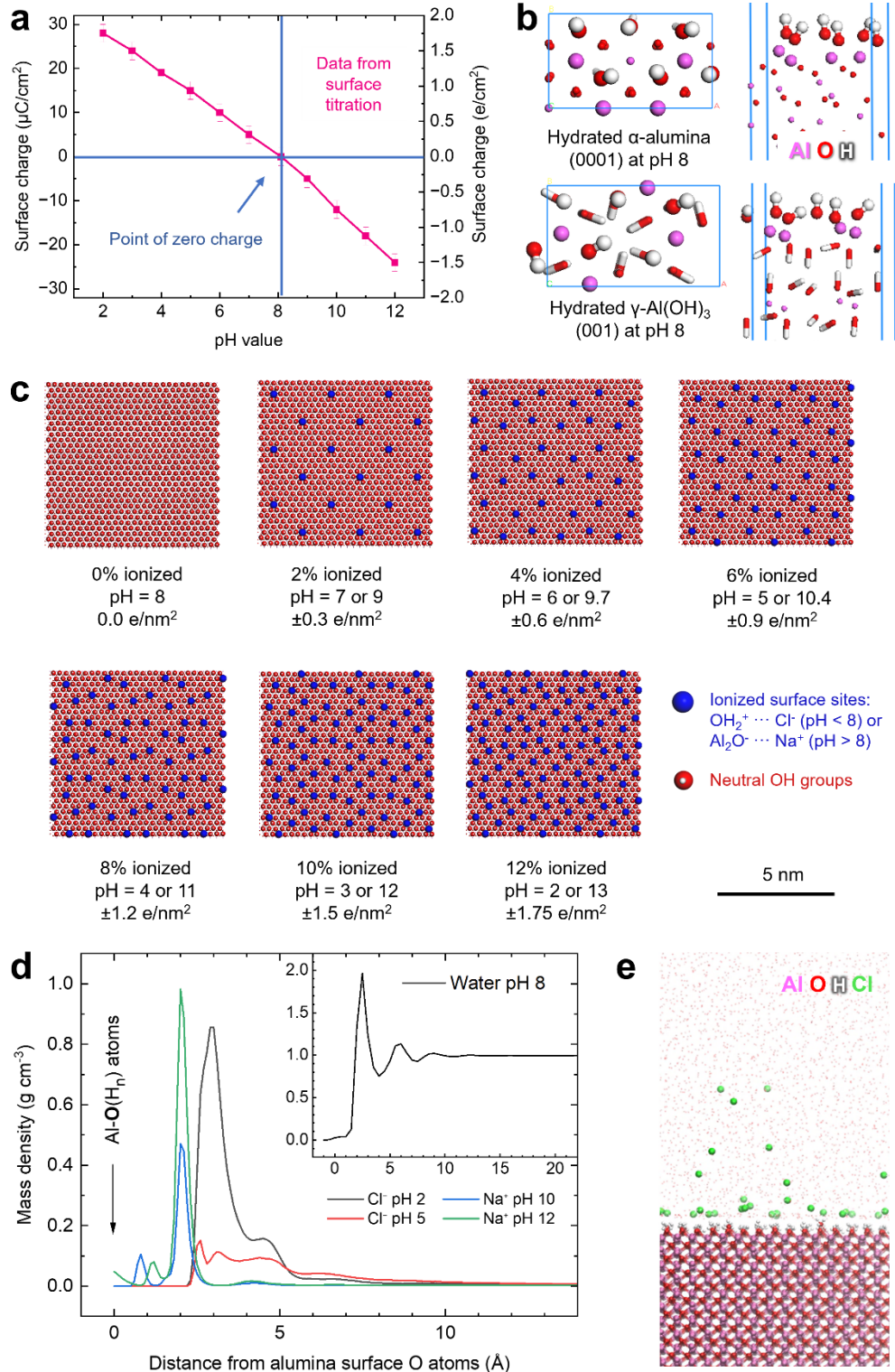


**Figure 8.** Surface charge density of hydrated alumina phases, implementation in atomistic models, and influence on electrolyte interfaces. (a) The average surface charge density of  $\alpha$ -Al<sub>2</sub>O<sub>3</sub> (0001)

surfaces in NaCl solution (0 to 0.5 M) as a function of pH value according to surface titration experiments.[58] The slope of the curve is lightly flatter for positively charged surface species at pH < 8.1 than for negatively charged surface species at pH > 8.1. Gibbsite and other hydrated alumina phases follow the same trend. (b) Unit models of electroneutral  $\alpha$ -Al<sub>2</sub>O<sub>3</sub> (0001) surfaces and  $\gamma$ -Al(OH)<sub>3</sub> (001) surfaces used to build larger ionized surfaces at specific pH values in (c). On the upper surface, the outer molecular layer of Al(OH)<sub>3</sub> is shown in ball-and-stick rendering to distinguish from the rest of the structure. (c) Top view onto  $\alpha$ -Al<sub>2</sub>O<sub>3</sub> (0001) surface models for pH values from 2 to 13, showing the range of density of positively or negatively charged groups up to 1.75e per nm<sup>2</sup>. Incoming molecules or ions near the surface accordingly adapt their interactions. The surface area shown is 24.729  $\times$  23.7945 Å<sup>2</sup>. (d) Density profiles of electrolytes at distinct pH values illustrate the effects of solution pH on the binding properties. Chloride ions at low pH value are bound to Al-OH<sub>2</sub><sup>+</sup> groups on the surface and diffuse into solution (past 0.5 nm), especially at pH values close to the pzc. Smaller sodium ions at high pH value are bound strongly to AlO<sup>-</sup> groups, which have a highly localized negative charge, with a smaller fraction dissociated past 0.5 nm away from the surface. The inset shows the water density profile at pH 8 (no ionization), which remains essentially the same at different pH values. (e) Representative snapshot of the interfacial region at pH = 2 with a distribution of positively charged surface sites and chloride counterions that penetrate the solution phase past 1 nm.

## 2.6. Adsorption of Corrosion Inhibitors

The pH-resolved surface models of alumina surfaces are therefore critical to predict the adsorption of molecules, polymers, or reactants in catalysis. As an example, we consider the adsorption of the corrosion inhibitor p-hydroxybenzoic acid on alumina surfaces, for which detailed adsorption isotherms were previously measured between pH 5 and 9 (Figure 9a).[79] There are order-of-magnitude differences in the adsorbed amount related to changes in alumina surface chemistry (Figure 8). The alumina sample in these experiments had a pzc of  $\sim 7$ , i.e., slightly lower than the more common value of 8. In the simulations, accordingly, we defined the zero-charge surface models equivalent to pH 7, shifting the pH downwards by one unit for the models in the database (Table 2). MD simulations at the pzc, two pH units below, and two pH above quantitatively correlate with the adsorbed amounts in experiments (Figure 9b-g). Specifically, we find strong adsorption at pH  $\sim 5$ , with a residence time of 85% and a binding free energy of -2.6 kcal/mol ( $\Delta G = -RT \ln K$  with  $K = \frac{t_{ads}}{t_{des} \cdot c_{sol}}$  with  $c_{sol} = 0.064$  M) (Figure 9b, c). The attraction arises from ion paring of the negatively charged carboxylate groups with the positively charged  $\text{Al}_2(\text{OH}_2)^+$  groups on the alumina surface. The computed binding free energy of -2.6 kcal/mol is in very good agreement with -3.6 kcal/mol calculated from the experimentally measured Langmuir adsorption constant ( $K_S = 0.42 \frac{l}{mmol} = 420 M^{-1}$ ).[79] At the point of zero charge at pH  $\sim 7$  and above at pH  $\sim 9$ , the adsorbed amount decreases significantly in experiment (Figure 9a) and in MD simulation (Figure 9c-g), from 1.8 molecules per  $\text{nm}^2$  to less than 0.2 molecules per  $\text{nm}^2$ . Ion paring is no longer feasible due to lack of surface charge at the pzc, and the presence of a negative surface

charge locally repels negatively charged benzoate groups at pH  $\sim$  9. The fraction of time p-hydroxybenzoate was in contact with the surface was then only 26% and 14%, respectively. Temporary contacts with the surface involve dipolar interactions and hydrogen bond interactions which add no relative strength due to surrounding water molecules. In addition, the phenolic OH group is partly deprotonated at pH 9 (which we accounted for in the simulation, see Figure 9g). The binding constants remain slightly larger than one and binding free energies remain slightly negative at -1.0 and -0.5 kcal/mol, related to the dilute concentration in solution. Simulations at lower pH of 3 predicted a further increase in binding of p-hydroxybenzoic acid with 98.8% of time bound and  $\Delta G$  (sim) = -4.2 kcal/mol (Figure 9c).

No prior tools or MD simulations have been available to obtain such quantitative, pH-resolved 3D molecular-scale insights. The quality of predictions relative to measurements is remarkable, similar to earlier IFF models for silica-organic interfaces.[82] We also noted some limitations of the classical Langmuir models of adsorption, which suggest high binding constants across the range of pH values (5, 7, 9) despite steeply decreasing adsorption (see ref. [79] and Section S6 in the Supplementary Material). These limitations appear to lie in theory rather than in the measurements while MD simulations with realistic alumina surface models enable excellent predictions across the range of alumina phases, surface environments, and multiphase materials.

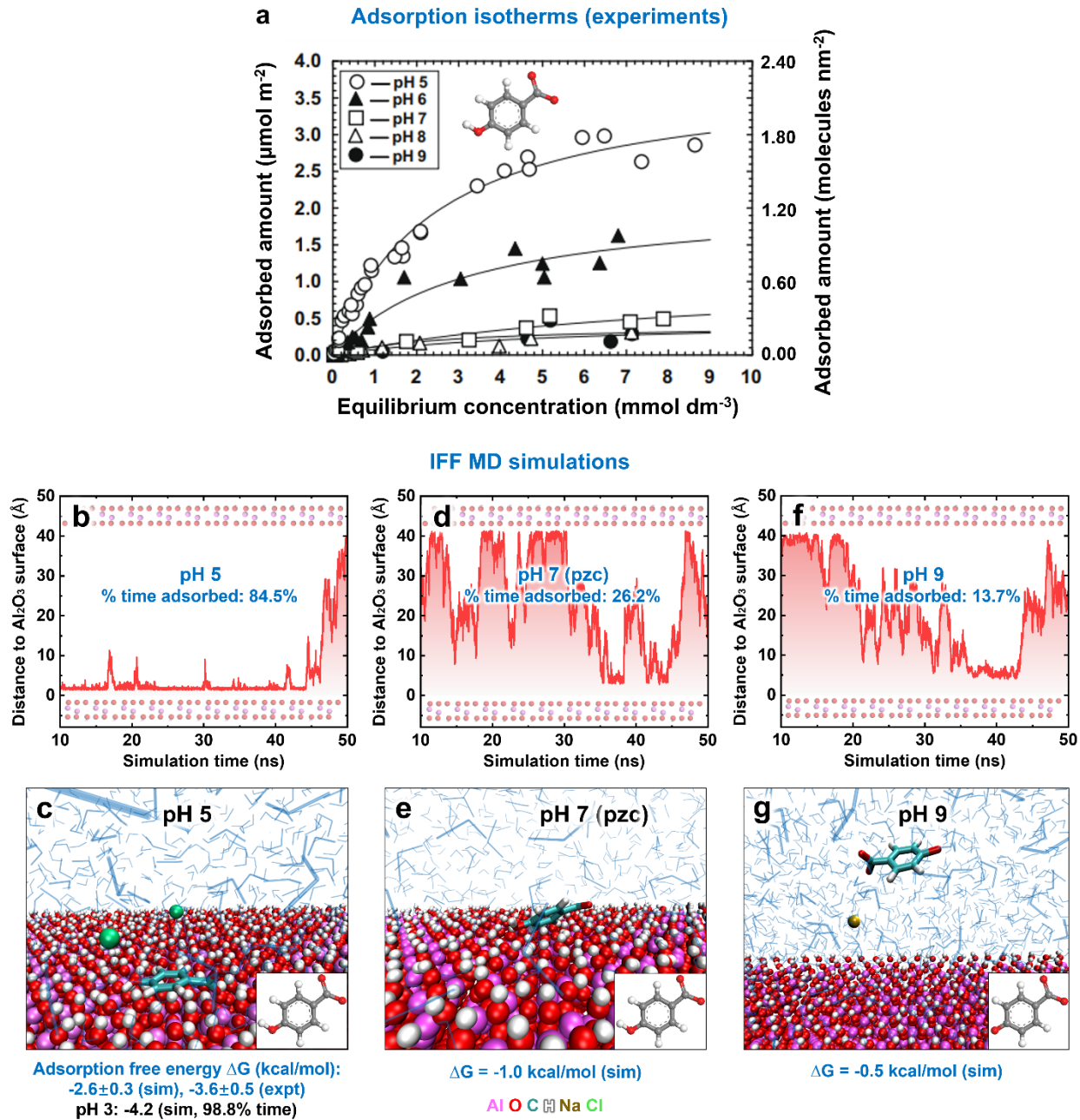


**Figure 9.** Adsorption of p-hydroxybenzoic acid, a corrosion inhibitor, according to experiments[79]

and simulations in aqueous solution at different pH values. (a) Experimental adsorption isotherms[79] indicate a major dependence of the adsorbed amount on the acidity, ranging from near monolayer coverage at pH 5 (~2 molecules per nm<sup>2</sup>) to weak temporary adsorption (<0.2

molecule per nm<sup>2</sup>) at pH 8 and 9 (reproduced with permission from ref. [79]). (b-g) MD simulations with surface models of 0.60 OH<sub>2</sub><sup>+</sup> groups per nm<sup>2</sup> (pH 5), full OH termination (pH 7, pzc), and 0.75 Al<sub>2</sub>O<sup>-</sup> groups per nm<sup>2</sup> (pH 9) show changes in adsorption of single molecules in excellent agreement with experimental adsorption isotherms. The time in contact was very high at pH 5 and decreased to transient adsorption at pH 9. Computed free energies of binding agree with laboratory data at pH 5.

### 3. Conclusion

In summary, we present a unified and rigorously validated set of INTERFACE Force Field (IFF) parameters and surface models for aluminum oxides and hydroxides that enable quantitative predictions of bulk and interfacial properties across all major alumina phases. These primarily nonbonded models capture the lattice parameters, densities, bulk moduli, surface energies, and water contact angles of  $\alpha$ -Al<sub>2</sub>O<sub>3</sub>,  $\gamma$ -Al<sub>2</sub>O<sub>3</sub>, diaspore, boehmite, and gibbsite with better than 95% agreement with experimental data. Simplicity and transferability eliminate the need for phase-specific reparameterization and ensure broad compatibility with CHARMM, AMBER, OPLS-AA, CVFF, and PCFF force fields to predict electrolyte interactions and organic assembly.

Beyond structural fidelity, the models accurately reproduce pH-dependent surface chemistry and charge distributions essential for realistic simulations of aqueous interfaces. The pH-resolved surface model database bridges experimental titration and zeta potential data with atomistic

resolution, enabling correct representation of protonated, neutral, and deprotonated alumina surfaces over the full pH range. This capability is indispensable for studying solid–electrolyte interfaces, adsorption of corrosion inhibitors, coatings, drugs, interaction with cell membranes, and interfacial reactivity in catalytic applications.

Compared to previous force fields and DFT/ML hybrid approaches, the IFF framework delivers higher accuracy, interpretability, and computational efficiency. It routinely supports simulation domains exceeding 10 nm and timescales beyond 100 ns—orders of magnitude more accessible than first-principles methods—while maintaining atomic-level realism. The models are thus well suited to explore complex multiphase systems involving electrolytes, dopants, organic molecules, and polymers under experimentally relevant conditions.

Overall, the new alumina models constitute a major advance in atomistic simulation methodology, providing a reliable foundation for predictive design of alumina-containing materials across diverse technologies—from catalysis and corrosion protection to electrode coatings, implants, and biomedical applications. The inclusion of realistic, pH-resolved surface chemistry also opens a pathway toward multiscale integration of chemical accuracy and materials functionality. The methodology can be readily extended to doped aluminas, mixed-metal oxides, and emerging oxide–polymer hybrid systems.

## 4. Computational Methods

### 4.1. Building of Molecular Models

Models of the aluminum oxides and hydroxides with 1.5–3.0 nm side length were constructed from multiple supercells of the unit cells obtained by X-ray diffraction. The graphical user interface of Materials Studio was utilized to build and visualize all-atom models.[84] The simulation cell was larger than 12 Å in three directions for all simulations, and vacuum slabs of at least >50 Å in the vertical direction were utilized for the simulation of surface energies and contact angles to exclude interactions with periodic images in this direction.

#### **4.2. Force Field Parameters**

The IFF parameters were developed using the energy expressions of common class I and class II force fields. The IFF parameters are compatible with several class I force fields such as CVFF,[50] CHARMM,[48] Dreiding,[49] AMBER,[37] and OPLAS-AA.[40] The energy terms include a 12-6 Lennard-Jones potential with Lorentz-Berthelot combination rules (or small variations thereof). IFF parameters are also compatible with class II force fields such as CFF,[51] PCFF,[52] and COMPASS.[53] Then, the energy terms include a 9-6 Lennard-Jones potential with Waldman-Hagler combination rules. By definition, class II force fields differ from class I force fields by additional cross-terms and higher order terms for bonded potentials. These additional terms are not necessary for or interfering with alumina phases and can be kept for originally included compounds.[46, 51]

#### **4.3. Molecular Dynamics Simulation of Crystal Structures and Lattice Parameters**

For the simulations of crystal structures and bulk modulus, MD simulations were carried out in the isothermal-isobaric ensemble (NPT), while the canonical ensemble (NVT) was employed for the simulations of surface properties. The Discover program in Materials Studio and the Large-scale Atomic/Molecular Massively Parallel Simulator (LAMMPS) were applied when using IFF-OPLS/CVFF,[84] and IFF-PCFF,[85] while the Nanoscale Molecular Dynamics (NAMD) program was employed for IFF-CHARMM.[86] Regardless of the software used, a spherical cutoff of 12 Å was applied for the summation of pair-wise Lennard-Jones interactions, which is the standard IFF setting. Ewald methods (Ewald for Discover program, Particle Mesh Ewald (PME) for NAMD and particle-particle particle-mesh solver (PPPM) for LAMMPS in high accuracy of  $10^{-6}$  kcal mol<sup>-1</sup> were employed for the summation of electrostatic interactions (Coulomb), which is also the standard IFF setting. Simulations were conducted for 2 ns and a timestep of 1 fs to achieve equilibrium, whereby all atoms were allowed to move freely (no fixed atoms). All simulations were repeated at least 3 times to obtain average results.

Though several settings are slightly different in these three simulation programs, however, they yield the same results (properties) within a typical difference of 0–2%, which is within the simulation errors. When using the Discover program, the temperature was controlled at 300 K using the velocity scaling thermostat with instantaneous fluctuations of  $\pm 10$  K, and the pressure was maintained at 1 atm with the Parrinello–Rahman barostat. When using the NAMD program, the temperature was controlled at 300 K using the Langevin thermostat with a damping coefficient of 1 ps<sup>-1</sup>. The average temperature remained within  $\pm 0.5$  K of the target temperature with

instantaneous fluctuations of  $\pm 20$  K. In LAMMPS, the temperature was controlled at 300 K using the Nose-Hoover thermostats with temperature damping every 100 fs.

#### 4.4. Simulation of Surface Energies

Surface free energies  $\gamma_{SV}$ , also called solid-vapor surface tensions, were computed using two NVT simulations, one with a 3D slab before and one with a 3D slab after cleavage. Before cleavage, a bulk slab with a length larger than 12 Å (typically  $> 20$  Å) in all three directions was used. After cleavage, a vacuum slab of  $> 50$  Å length in the cleavage direction was created to expose the surface. For a given compound, these two models had the same number of atoms and the same equilibrium size in the  $x$  and  $y$  directions. The two model systems were subjected to NVT MD simulation at 300 K for 2 ns to reach equilibrium. The difference in average total energy between the non-cleaved structure  $E_{NC}$  and the cleaved structure  $E_C$  equaled the surface free energy per surface area  $A$ :

$$\gamma_{SV} = \frac{E_C - E_{NC}}{2A} - T \frac{S_C - S_{NC}}{2A} \approx \frac{E_C - E_{NC}}{2A}. \quad (3)$$

The entropy contribution  $-T \frac{S_C - S_{NC}}{2A}$  is negligible compared to the cohesive energy contribution  $\frac{E_C - E_{NC}}{2A}$  in the metal oxides, supported by minor oscillations of the metal atoms around their lattice points in the bulk and at the cleaved surfaces.[42] The entropy term was estimated to contribute less than 0.01 J m<sup>-2</sup> to the reported surface free energies, which is small compared to surface energies of metal oxides in the range around 0.3 J m<sup>-2</sup> to 2.0 J m<sup>-2</sup> and within the standard deviations of experimental measurements ( $\geq 0.01$  J m<sup>-2</sup>).

#### **4.5. Simulation of Water Contact Angles**

The water contact angle was computed using MD simulations in the NVT ensemble as an average over 2 ns using the LAMMPS program (IFF-OPLS/CVFF, IFF-PCFF) and the NAMD program (IFF-CHARMM). For the hydrated  $\alpha$ -Al<sub>2</sub>O<sub>3</sub> (0001) surface, as an example, a typical cell size of 41.215×47.589×80.000 Å<sup>3</sup> including a >50 Å vacuum slab was built to allow enough space for the water droplet to wet the surface. A water cube consisting of 515 SPC water molecules was placed 5 Å above the hydrated  $\alpha$ -Al<sub>2</sub>O<sub>3</sub> (0001) surface. During subsequent MD simulation, the water cube gradually spread out and reached the wetting equilibrium on the hydrated  $\alpha$ -Al<sub>2</sub>O<sub>3</sub> (0001) surface. Snapshots over the last 2 ns in equilibrium were collected for analysis using circular overlays as described in ref. [87]. The settings in simulation protocols were the same as for crystal structures and surface energies.

#### **4.6. Simulation of Mechanical Properties**

Mechanical properties of the alumina phases were investigated using equilibrium molecular dynamics (MD) simulations using LAMMPS. For example, a 5 x 5 x 2 supercell of  $\alpha$ -Al<sub>2</sub>O<sub>3</sub> was utilized. Starting with the equilibration structure as used in the calculation of lattice parameters, the structure was exposed to a controlled isotropic stress or anisotropic deformation and sampling of the resulting lattice parameters or pressure tensor, respectively. To obtain statistically meaningful averages, ten copies of each system were equilibrated for 10 ns in the NPT ensemble

at  $T = 298.15$  K and  $P = 1$  atm using a Verlet integrator with a timestep of 1 fs. The deterministic Nose-Hoover thermostat and barostat with coupling constants of 100 and 1000 fs, respectively, were applied to maintain constant temperature and pressure. To ensure that the main elements of the stress tensor reached the desired pressure of 1 atm and that off-diagonal elements were close to zero, the simulation box was adjusted independently in all six directions. Following equilibration, the Enhanced Monte Carlo program was used to alter the dimensions of the simulation box in one direction, while keeping the others constant. Elongation and compression were performed up to 1% in the main directions and up to 3% in the off-diagonal directions. Each deformed system underwent further simulation in the NVT ensemble at  $T = 298.15$  K, during which the strain tensor was sampled every 1 ps. Using linear regression, the slope of the stress-strain curve was calculated and from it, the stiffness tensor  $C$  was obtained. The elastic compliance tensor  $S$  was then derived by inverting  $C$ , enabling computation of the elastic moduli  $E_i = 1/S_{ii}$ ,  $i = 1, 2, 3$ , the Poisson ratio  $\nu$ , shear moduli  $G_{ij} = E_i/(2+2\nu_{ij})$ ,  $i = 1, 2, 3$ , and bulk modulus  $K = E/(3-6\nu)$  [7].

*Bulk Modulus.* The bulk modulus was calculated using the Discover program in Materials Studio with two independent NPT simulations at low pressure (0.0001 GPa) and high pressure (1 GPa) with the Parrinello–Rahman barostat, respectively. Other simulation settings remained the same as described in simulation protocols for lattice parameters. The bulk modulus was calculated using the following equation:

$$BM = -\frac{P_l - P_h}{V_l - V_h} \times V_l. \quad (3)$$

$P_l$  was the simulated value of low pressure,  $P_h$  the simulated value of high pressure,  $V_l$  the simulated cell volume at low pressure, and  $V_h$  the simulated cell volume at high pressure.

*Elastic Constants.* LAMMPS was employed to simulate the elastic constants with IFF-OPLS/CVFF with reference to the LAMMPS examples.[88] The Ewald method (PPPM) was used for the summation of electrostatic interactions (Coulomb) with a high accuracy of  $10^{-6}$  kcal mol $^{-1}$ . Several variables were set for the simulations, e.g., the sampling interval was 20 timesteps, the number of samples was 20, and the frequency of one average sampling was 400 timesteps. The system was first equilibrated for 2 ns followed by simulations for 0.5 ns with a timestep of 1 fs at 298.15 K for each perturbation cycle. Positive and negative deformations (equal to 1% of the strain) were exerted on the lattice structure in six directions during the perturbation cycles, including  $xx$ ,  $yy$ ,  $zz$ ,  $xy$ ,  $xz$ , and  $yz$ .

#### 4.7. Simulation of Solid-Liquid Interfaces

The density profiles of the alumina surfaces in contact with water were simulated at pH values of 2, 5, 8, 10, and 12 using MD simulations in the NPT ensemble, allowing full equilibration of the liquid density. We built simulation boxes of  $\sim 3$  nm x 3 nm lateral extension with the pH-specific surface models and a water slab of at least 5 nm height. Relaxation over 100 ns allowed the equilibration of positions of  $\text{Cl}^-$  or  $\text{Na}^+$  ions on and off the surface (with ions initially placed away from the surface for equilibration), and sampling of the density profiles vertical to the alumina (0001) surfaces over the last 75 ns. The solution density was approximately 1.00 g/cm $^3$  and MD

simulations were carried using a time step of 1 fs at 298 K using the program LAMMPS, the PPPM method for high accuracy electrostatics ( $10^{-4}$  sufficient), and a spherical cutoff for van-der-Waals interactions at 12 Å (IFF standard). Density profiles were created using custom python scripts.

#### **4.8. Simulation of the Adsorption of Organic Molecules**

The binding energies and conformations of p-hydroxybenzoate on the alumina (0001) surfaces were computed using the surface models for the respective pH values of 5, 7, and 9 in contact with a water slab of 4 nm thickness (TIP3P model, 856 molecules) and the organic molecules. As determined in the related experiments, the point of zero charge with full OH termination of the surface was set as pH 7 (rather than pH 8), with the other two models reflecting surface ionization 2 pH units below and above the pzc at 5 and 9 (rather than 6 and 10). The molecular models of p-hydroxybenzoate and its deprotonated form at high pH were based on the IFF/CHARMM36 force fields, including IFF virtual  $\pi$  electrons.[89] The solution density was 1.000 g/cm<sup>3</sup>, and MD simulations in the NVT ensemble were carried out for 80 ns with a time step of 1 fs at 298 K, using the program NAMD, the PPPM method for high accuracy electrostatics ( $10^{-4}$ ), and a spherical cutoff for van-der-Waals interactions at 12 Å (IFF standard). The time in contact (within 3 Å from superficial O atoms) was recorded to compute the percentage of time in contact and the free energy of binding, along with the concentration in solution (0.064 M) and the approximate concentration of available adsorption sites (~1 M, ~2 sites per nm<sup>2</sup> surface area in flat-on binding configuration).

## **Supplementary Material Available**

Additional Figures, Tables, discussion, and Supplementary Files that contain the force field, the database of 3D surface models, simulation run scripts, and examples to reproduce the reported data.

## **Acknowledgements**

We acknowledge the helpful comments provided by Dr. Pieter J. in 't Veld, BASF SE.

## **Author Contributions: CRedit**

C.Z. contributed to conceptualization, data curation, methodology, analysis, writing the original and revised drafts. K. K. contributed to methodology, validation, and review. S. D., S. P. F., and K. S. contributed to data curation, visualization, and writing the original draft. P. K., N. S. K., and E. S. contributed to analysis and review. R. K. M. contributed to conceptualization, resources, supervision, investigation, writing and editing. H. H. contributed to conceptualization, resources, supervision, investigation, data curation, writing, editing, and validation.

## **Funding Sources**

The authors acknowledge support by the National Science Foundation (OAC 1931587, CMMI 1940335, DMREF 2323546) and the University of Colorado Boulder. We utilized allocations of computational resources at the Argonne Leadership Computing Facility, supported by the Office

of Science of the U.S. Department of Energy (DE-AC02-06CH11357), and at the Summit supercomputer, a joint effort of the University of Colorado Boulder and Colorado State University supported by the National Science Foundation (ACI 1532235 and ACI 1532236). We also utilized allocations of computational resources at the BASF supercomputer Quriousity.

## References

- [1] G.E. Totten, D.S. MacKenzie, *Handbook of Aluminum: Vol. 1: Physical Metallurgy and Processes*, Marcel Dekker, New York, 2003.
- [2] G.E. Totten, D.S. MacKenzie, *Handbook of Aluminum: Vol. 2: Alloy Production and Materials Manufacturing*, Marcel Dekker, New York, 2003.
- [3] L.D. Hart, E. Lense, *Alumina Chemicals: Science and Technology Handbook*, Wiley, Hoboken, NJ, USA, 1990.
- [4] D. Li, C. Wang, Z. Li, H. Wang, J. He, J. Zhu, Y. Zhang, C. Shen, F. Xiao, Y. Gao, X. Zhang, Y. Li, P. Wang, J. Peng, G. Cai, B. Zuo, Y. Yang, Y. Shen, W. Song, X. Zhang, L. Shen, X. Chen, Nano-sized Al<sub>2</sub>O<sub>3</sub> particle-induced autophagy reduces osteolysis in aseptic loosening of total hip arthroplasty by negative feedback regulation of RANKL expression in fibroblasts, *Cell Death Dis.*, 9 (2018) 840.
- [5] X. Li, Z. Ye, H. Jiao, K. Zhao, Z. Yan, Al<sub>2</sub>O<sub>3</sub> porous ceramics with high strength by protein foaming Method, *Sci. Rep.*, 15 (2025) 6424.
- [6] Y. Gu, Y. Ma, Z. Long, S. Zhao, Y. Wang, W. Zhang, One-pot synthesis of supported Ni@Al<sub>2</sub>O<sub>3</sub> catalysts with uniform small-sized Ni for hydrogen generation via ammonia decomposition, *Int. J. Hydrogen Energy*, 46 (2021) 4045-4054.
- [7] F. Bouville, Strong and tough nacre-like aluminas: Process-structure-performance relationships and position within the nacre-inspired composite landscape, *J. Mater. Res.*, 35 (2020) 1076-1094.
- [8] W. Peng, K.T. Mao, F.C. Cai, H.G. Meng, Z.J. Zhu, T.Q. Li, S.J. Yuan, Z.J. Xu, X.Y. Feng, J.H. Xu, M.D. McGehee, J.X. Xu, Reducing nonradiative recombination in perovskite solar cells with a porous insulator contact, *Science*, 379 (2023) 683-690.
- [9] Z.D. Wang, G.D. Meng, L.L. Wang, L.L. Tian, S.Y. Chen, G.L. Wu, B. Kong, Y.H. Cheng, Simultaneously enhanced dielectric properties and through-plane thermal conductivity of epoxy composites with alumina and boron nitride nanosheets, *Sci. Rep.*, 11 (2021).
- [10] Y. Chen, N.N. Wang, O. Ola, Y.D. Xia, Y.Q. Zhu, Porous ceramics: Light in weight but heavy in energy and environment technologies, *Mater. Sci. Eng. R-Rep.*, 143 (2021) 100589.
- [11] M. Mohammadi, M. Khodamorady, B. Tahmasbi, K. Bahrami, A. Ghorbani-Choghamarani, Boehmite nanoparticles as versatile support for organic-inorganic hybrid materials: Synthesis, functionalization, and applications in eco-friendly catalysis, *J. Industrial Engineering Chem.*, 97 (2021) 1-78.
- [12] F. Zhang, M.H. Zeng, R.D. Yappert, J.K. Sun, Y.H. Lee, A.M. LaPointe, B. Peters, M.M. Abu-Omar, S.L.

Scott, Polyethylene upcycling to long-chain alkylaromatics by tandem hydrogenolysis/aromatization, *Science*, 370 (2020) 437-441.

[13] J.A. Nguyen, A. Becker, K. Kanhaiya, H. Heinz, A.W. Weimer, Analyzing the Li-Al-O interphase of atomic layer-deposited Al<sub>2</sub>O<sub>3</sub> films on layered oxide cathodes using atomistic simulations, *ACS Appl. Mater. Interfaces*, 16 (2024) 1861-1875.

[14] E. Nematollahi, M. Pourmadadi, F. Yazdian, H. Fatoorehchi, H. Rashedi, M.N. Nigjeh, Synthesis and characterization of chitosan/polyvinylpyrrolidone coated nanoporous  $\gamma$ -alumina as a pH-sensitive carrier for controlled release of quercetin, *Int. J. Biological Macromolecules*, 183 (2021) 600-613.

[15] Y.C. Wang, K. Yu, J.P. Zhao, A. Xin, NaOH hydrothermally treated gibbsite modified silicone acrylic emulsion-based intumescent flame-retardant coatings for plywood, *Colloid Surf. A-Physicochem. Eng. Asp.*, 646 (2022) 129001.

[16] K. Kanhaiya, H. Heinz, Adsorption and diffusion of oxygen on pure and partially oxidized metal surfaces in ultrahigh resolution, *Nano Lett.*, 22 (2022) 5392-5400.

[17] E. Georgantzia, M. Gkantou, G.S. Kamaris, Aluminium alloys as structural material: A review of research, *Engineering Structures*, 227 (2021) 111372.

[18] E.A. Starke Jr, J.T. Staley, Application of modern aluminum alloys to aircraft, *Progress in aerospace sciences*, 32 (1996) 131-172.

[19] K.U. Bhat, D.B. Panemangalore, S.B. Kuruveri, M. John, P.L. Menezes, Surface modification of 6xxx Series aluminum alloys, *Coatings*, 12 (2022) 180.

[20] K. Kanhaiya, M. Nathanson, P.J. in 't Veld, C. Zhu, I. Nikiforov, E.B. Tadmor, Y.K. Choi, W. Im, R.K. Mishra, H. Heinz, Accurate force fields for atomistic simulations of oxides, hydroxides, and organic hybrid materials up to the micrometer scale, *J. Chem. Theor. Comput.*, 19 (2023) 8293-8322.

[21] R. Buchheit, L. Montes, M. Martinez, J. Michael, P. Hlava, The electrochemical characteristics of bulk-synthesized Al<sub>2</sub>CuMg, *J. Electrochem. Soc.*, 146 (1999) 4424.

[22] X. Nie, A. Leyland, H. Song, A. Yerokhin, S. Dowey, A. Matthews, Thickness effects on the mechanical properties of micro-arc discharge oxide coatings on aluminium alloys, *Surf. Coat. Technol.*, 116 (1999) 1055-1060.

[23] S. Pathak, A. Sharma, A. Khanna, Value addition to waterborne polyurethane resin by silicone modification for developing high performance coating on aluminum alloy, *Prog. Org. Coat.*, 65 (2009) 206-216.

[24] S. Mirabedini, G. Thompson, S. Moradian, J. Scantlebury, Corrosion performance of powder coated aluminium using EIS, *Prog. Org. Coat.*, 46 (2003) 112-120.

[25] L. Jia, J. Shichun, S. Yan, N. Cong, H. Genzhe, Effects of zinc on the laser welding of an aluminum alloy and galvanized steel, *Journal of materials processing technology*, 224 (2015) 49-59.

[26] X. Tang, Y. Yu, Electrospinning preparation and characterization of alumina nanofibers with high aspect ratio, *Ceram. Int.*, 41 (2015) 9232-9238.

[27] F.-L. Toma, L.-M. Berger, C.C. Stahr, T. Naumann, S. Langner, Microstructures and functional properties of suspension-sprayed Al<sub>2</sub>O<sub>3</sub> and TiO<sub>2</sub> coatings: An overview, *Journal of Thermal Spray Technology*, 19 (2010) 262-274.

[28] R.T. Sanderson, Principles of electronegativity Part I. General nature, *J. Chem. Educ.*, 65 (1988) 112.

[29] Y. Xie, D. Kocae, Y. Kocae, J. Cheng, W. Liu, The effect of novel synthetic methods and parameters

control on morphology of nano-alumina particles, *Nanoscale Res. Lett.*, 11 (2016) 259.

[30] S. Lid, S. Köppen, L.C. Ciacchi, Creation of models and parametrization of a classical force field for amorphous Al<sub>2</sub>O<sub>3</sub>/water interfaces based on Density Functional Theory, *Comput. Mater. Sci.*, 140 (2017) 307-314.

[31] A.L. Martinotto, J.E. Zorzi, C.A. Perottoni, Born-Oppenheimer molecular dynamics simulation of pentanoic acid adsorption on  $\alpha$ -Al<sub>2</sub>O<sub>3</sub>, *Appl. Surf. Sci.*, 423 (2017) 780-787.

[32] Q. Zhang, T. Çağın, A. Van Duin, W.A. Goddard III, Y. Qi, L.G. Hector Jr, Adhesion and nonwetting-wetting transition in the Al/ $\alpha$ -Al<sub>2</sub>O<sub>3</sub> interface, *Phys. Rev. B*, 69 (2004) 045423.

[33] C. Li, P. Choi, Molecular dynamics study of the adsorption behavior of normal alkanes on a relaxed  $\alpha$ -Al<sub>2</sub>O<sub>3</sub> (0001) surface, *J. Phys. Chem. C*, 111 (2007) 1747-1753.

[34] I.-C. Yeh, J.L. Lenhart, J.A. Orlicki, B.C. Rinderspacher, Molecular dynamics simulation study of adsorption of bioinspired oligomers on alumina surfaces, *J. Phys. Chem. B*, 123 (2019) 7024-7035.

[35] H. Heinz, T.J. Lin, R.K. Mishra, F.S. Emami, Thermodynamically consistent force fields for the assembly of inorganic, organic, and biological nanostructures: the INTERFACE force field, *Langmuir*, 29 (2013) 1754-1765.

[36] H. Heinz, H. Ramezani-Dakhel, Simulations of inorganic-bioorganic interfaces to discover new materials: insights, comparisons to experiment, challenges, and opportunities, *Chem. Soc. Rev.*, 45 (2016) 412-448.

[37] J. Wang, R.M. Wolf, J.W. Caldwell, P.A. Kollman, D.A. Case, Development and testing of a general amber force field, *J. Comput. Chem.*, 25 (2004) 1157-1174.

[38] K. Vanommeslaeghe, E. Hatcher, C. Acharya, S. Kundu, S. Zhong, J. Shim, E. Darian, O. Guvench, P. Lopes, I. Vorobiov, CHARMM general force field: A force field for drug-like molecules compatible with the CHARMM all-atom additive biological force fields, *J. Comput. Chem.*, 31 (2010) 671-690.

[39] H. Sun, COMPASS: an ab initio force-field optimized for condensed-phase applications overview with details on alkane and benzene compounds, *J. Phys. Chem. B*, 102 (1998) 7338-7364.

[40] W.L. Jorgensen, D.S. Maxwell, J. Tirado-Rives, Development and testing of the OPLS all-atom force field on conformational energetics and properties of organic liquids, *J. Am. Chem. Soc.*, 118 (1996) 11225-11236.

[41] H. Heinz, R.A. Vaia, B.L. Farmer, R.R. Naik, Accurate simulation of surfaces and interfaces of face-centered cubic metals using 12-6 and 9-6 Lennard-Jones potentials, *J. Phys. Chem. C*, 112 (2008) 17281-17290.

[42] K. Kanhaiya, S. Kim, W. Im, H. Heinz, Accurate simulation of surfaces and interfaces of ten FCC metals and steel using Lennard-Jones potentials, *npj Comput. Mater.*, 7 (2021) 17.

[43] F.S. Emami, V. Puddu, R.J. Berry, V. Varshney, S.V. Patwardhan, C.C. Perry, H. Heinz, Force field and a surface model database for silica to simulate interfacial properties in atomic resolution, *Chem. Mater.*, 26 (2014) 2647-2658.

[44] H. Heinz, U.W. Suter, Atomic charges for classical simulations of polar systems, *J. Phys. Chem. B*, 108 (2004) 18341-18352.

[45] H. Heinz, H. Koerner, K.L. Anderson, R.A. Vaia, B.L. Farmer, Force field for mica-type silicates and dynamics of octadecylammonium chains grafted to montmorillonite, *Chem. Mater.*, 17 (2005) 5658-5669.

[46] H. Heinz, H.J. Castelijns, U.W. Suter, Structure and phase transitions of alkyl chains on mica, *J. Am. Chem. Soc.*, 125 (2003) 9500-9510.

[47] J.J. Winetrot, K. Kanhaiya, J. Kemppainen, P.J. in 't Veld, G. Sachdeva, R. Pandey, B. Damirchi, A. van Duin, G.M. Odegard, H. Heinz, Implementing reactivity in molecular dynamics simulations with harmonic

force fields, *Nat. Commun.*, 15 (2024) 7945.

[48] J. Huang, A.D. MacKerell Jr, CHARMM36 all-atom additive protein force field: Validation based on comparison to NMR data, *J. Comput. Chem.*, 34 (2013) 2135-2145.

[49] S.L. Mayo, B.D. Olafson, W.A. Goddard, DREIDING: a generic force field for molecular simulations, *J. Phys. Chem.*, 94 (1990) 8897-8909.

[50] P. Dauber-Osguthorpe, V.A. Roberts, D.J. Osguthorpe, J. Wolff, M. Genest, A.T. Hagler, Structure and energetics of ligand binding to proteins: *Escherichia coli* dihydrofolate reductase-trimethoprim, a drug-receptor system, *Proteins: Struct., Funct., Bioinf.*, 4 (1988) 31-47.

[51] H. Sun, S.J. Mumby, J.R. Maple, A.T. Hagler, An ab initio CFF93 all-atom force field for polycarbonates, *J. Am. Chem. Soc.*, 116 (1994) 2978-2987.

[52] H. Sun, Ab initio calculations and force field development for computer simulation of polysilanes, *Macromolecules*, 28 (1995) 701-712.

[53] H. Sun, Z. Jin, C. Yang, R.L. Akkermans, S.H. Robertson, N.A. Spenley, S. Miller, S.M. Todd, COMPASS II: extended coverage for polymer and drug-like molecule databases, *Journal of molecular modeling*, 22 (2016) 1-10.

[54] J. Liu, E. Tennessen, J. Miao, Y. Huang, J.M. Rondinelli, H. Heinz, Understanding chemical bonding in alloys and the representation in atomistic simulations, *J. Phys. Chem. C*, 122 (2018) 14996-15009.

[55] R.J. Hill, Crystal-structure refinement and electron-density distribution in diaspore, *Phys. Chem. Miner.*, 5 (1979) 179-200.

[56] J. Lewis, D. Schwarzenbach, H.D. Flack, Electric field gradients and charge density in corundum,  $\alpha$ -Al<sub>2</sub>O<sub>3</sub>, *Acta Cryst. A*, 38 (1982) 733-739.

[57] T.Z. Lin, H. Heinz, Accurate force field parameters and pH resolved surface models for hydroxyapatite to understand structure, mechanics, hydration, and biological interfaces, *J. Phys. Chem. C*, 120 (2016) 4975-4992.

[58] J.W. Ntalikwa, Determination of surface charge density of  $\alpha$ -alumina by acid-base titration, *Bulletin of the Chemical Society of Ethiopia*, 21 (2007).

[59] T.D. Pham, M. Kobayashi, Y. Adachi, Interfacial characterization of  $\alpha$ -alumina with small surface area by streaming potential and chromatography, *Colloids and Surfaces A: Physicochemical and Engineering Aspects*, 436 (2013) 148-157.

[60] J. Park, J.R. Regalbuto, A simple, accurate determination of oxide PZC and the strong buffering effect of oxide surfaces at incipient wetness, *J. Colloid Interface Sci.*, 175 (1995) 239-252.

[61] E.E. Newnham, Y.M.D. Haan, Refinement of the  $\alpha$  Al<sub>2</sub>O<sub>3</sub>, Ti<sub>2</sub>O<sub>3</sub>, V<sub>2</sub>O<sub>3</sub> and Cr<sub>2</sub>O<sub>3</sub> structures, *Zeitschrift für Kristallographie - Crystalline Materials*, 117 (1962) 235-237.

[62] J.M. McHale, A. Navrotsky, A.J. Perrotta, Effects of increased surface area and chemisorbed H<sub>2</sub>O on the relative stability of nanocrystalline  $\gamma$ -Al<sub>2</sub>O<sub>3</sub> and  $\alpha$ -Al<sub>2</sub>O<sub>3</sub>, *J. Phys. Chem. B*, 101 (1997) 603-613.

[63] T. Goto, O.L. Anderson, I. Ohno, S. Yamamoto, Elastic constants of corundum up to 1825 K, *Journal of Geophysical Research: Solid Earth*, 94 (1989) 7588-7602.

[64] H. d'Amour, D. Schiferl, W. Denner, H. Schulz, W. Holzapfel, High-pressure single-crystal structure determinations for ruby up to 90 kbar using an automatic diffractometer, *J. Appl. Phys.*, 49 (1978) 4411-4416.

[65] L. Smrčok, V. Langer, J. Křestan,  $\gamma$ -Alumina: a single-crystal X-ray diffraction study, *Acta Crystallographica Section C: Crystal Structure Communications*, 62 (2006) i83-i84.

[66] J. Majzlan, A. Navrotsky, W.H. Casey, Surface enthalpy of boehmite, *Clays Clay Miner.*, 48 (2000) 699-707.

[67] A. Pedone, G. Malavasi, M.C. Menziani, A.N. Cormack, U. Segre, A new self-consistent empirical interatomic potential model for oxides, silicates, and silica-based glasses, *J. Phys. Chem. B*, 110 (2006) 11780-11795.

[68] R.T. Cygan, J.-J. Liang, A.G. Kalinichev, Molecular models of hydroxide, oxyhydroxide, and clay phases and the development of a general force field, *J. Phys. Chem. B*, 108 (2004) 1255-1266.

[69] M. Povreau, J.A. Greathouse, R.T. Cygan, A.G. Kalinichev, Structure of hydrated gibbsite and brucite edge surfaces: DFT results and further development of the ClayFF classical force field with metal–O–H angle bending terms, *J. Phys. Chem. C*, 121 (2017) 14757-14771.

[70] A.K. Rappe, C.J. Casewit, K.S. Colwell, W.A. Goddard, W.M. Skiff, UFF, a full periodic table force field for molecular mechanics and molecular dynamics simulations, *J. Am. Chem. Soc.*, 114 (1992) 10024-10035.

[71] G.M. Psolfogiannakis, J.F. McCleery, E. Jaramillo, A.C.T. van Duin, ReaxFF reactive molecular dynamics simulation of the hydration of Cu-SSZ-13 zeolite and the formation of Cu dimers, *J. Phys. Chem. C*, 119 (2015) 6678-6686.

[72] Q. Zhang, T. Çağın, A. Van Duin, W.A. Goddard III, Y. Qi, L.G. Hector Jr, Adhesion and nonwetting-wetting transition in the Al/α-Al<sub>2</sub>O<sub>3</sub> interface, *Phys. Rev. B*, 69 (2004) 045423.

[73] P.J. Eng, T.P. Trainor, G.E. Brown Jr., G.A. Waychunas, M. Newville, S.R. Sutton, M.L. Rivers, Structure of the hydrated alpha-Al<sub>2</sub>O<sub>3</sub> (0001) surface, *Science*, 288 (2000) 1029-1033.

[74] D. Yang, M. Krasowska, R. Sedev, J. Ralston, The unusual surface chemistry of α-Al<sub>2</sub>O<sub>3</sub> (0001), *Phys. Chem. Chem. Phys.*, 12 (2010) 13724-13729.

[75] J. Zähr, S. Oswald, M. Türpe, H.J. Ullrich, U. Füssel, Characterisation of oxide and hydroxide layers on technical aluminum materials using XPS, *Vacuum*, 86 (2012) 1216-1219.

[76] T. Hiemstra, P. Venema, W.H.V. Riemsdijk, Intrinsic proton affinity of reactive surface groups of metal (hydr)oxides: The bond valence principle, *J. Colloid Interface Sci.*, 184 (1996) 680-692.

[77] B. Kasprzyk-Hordern, Chemistry of alumina, reactions in aqueous solution and its application in water treatment, *Adv. Colloid Interface Sci.*, 110 (2004) 19-48.

[78] F.T. Da Silva, A. Barbejat, H.S. Filho, Influence of handling and heating cycle on the morphology and flexural strength of glass-infiltrated alumina bars, *Revista Materia*, 13 (2008) 49-55.

[79] M.R. Das, J.M. Borah, W. Kunz, B.W. Ninham, S. Mahiuddin, Ion specificity of the zeta potential of α-alumina, and of the adsorption of p-hydroxybenzoate at the α-alumina–water interface, *J. Colloid Interface Sci.*, 344 (2010) 482-491.

[80] B. Ludwig, T.T. Burke, Infrared spectroscopy studies of aluminum oxide and metallic aluminum powders, Part I: Thermal dehydration and decomposition, *Powders*, 1 (2022) 47-61.

[81] B. Ludwig, Infrared spectroscopy studies of aluminum oxide and metallic aluminum powders, Part II: Adsorption reactions of organofunctional silanes, *Powders*, 1 (2022) 75-87.

[82] F.S. Emami, V. Puddu, R.J. Berry, V. Varshney, S.V. Patwardhan, C.C. Perry, H. Heinz, Prediction of specific biomolecule adsorption on silica surfaces as a function of pH and particle size, *Chem. Mater.*, 26 (2014) 5725-5734.

[83] S.V. Patwardhan, F.S. Emami, R.J. Berry, S.E. Jones, R.R. Naik, O. Deschaume, H. Heinz, C.C. Perry, Chemistry of aqueous silica nanoparticle surfaces and the mechanism of selective peptide adsorption, *J. Am.*

Chem. Soc., 134 (2012) 6244-6256.

- [84] D.S. BIOVIA, Materials Studio, v7. 0.200, San Diego: Dassault Systèmes, (2013).
- [85] A.P. Thompson, H.M. Aktulga, R. Berger, D.S. Bolintineanu, W.M. Brown, P.S. Crozier, P.J. in't Veld, A. Kohlmeyer, S.G. Moore, T.D. Nguyen, LAMMPS-a flexible simulation tool for particle-based materials modeling at the atomic, meso, and continuum scales, *Comput. Phys. Commun.*, 271 (2022) 108171.
- [86] J.C. Phillips, R. Braun, W. Wang, J. Gumbart, E. Tajkhorshid, E. Villa, C. Chipot, R.D. Skeel, L. Kale, K. Schulten, Scalable molecular dynamics with NAMD, *J. Comput. Chem.*, 26 (2005) 1781-1802.
- [87] J. Liu, J. Zeng, C. Zhu, J. Miao, Y. Huang, H. Heinz, Interpretable molecular models for molybdenum disulfide and insight into selective peptide recognition, *Chem. Sci.* , 11 (2020) 8708-8722.
- [88] F.H. Stillinger, T.A. Weber, Computer simulation of local order in condensed phases of silicon, *Phys. Rev. B*, 31 (1985) 5262.
- [89] C. Zhu, S.E. Hoff, M. Hémadi, H. Heinz, Accurate and ultrafast simulation of molecular recognition and assembly on metal surfaces in four dimensions, *Acs Nano*, 17 (2023) 9938-9952.

## Supplementary Material

for

# INTERFACE Force Field for Alumina with Validated Bulk Phases and a pH-Resolved Surface Model Database for Electrolyte and Organic Interfaces

Cheng Zhu,<sup>1</sup> Krishan Kanhaiya,<sup>1</sup> Samir Darouich,<sup>2</sup> Sean P. Florez,<sup>1</sup> Karnajit Sen,<sup>2</sup> Patrick Keil,<sup>3</sup>  
Nawel S. Khelfallah,<sup>4</sup> Eduard Schreiner,<sup>2</sup> Ratan K. Mishra,<sup>2\*</sup> Hendrik Heinz<sup>1\*</sup>

<sup>1</sup> Department of Chemical and Biological Engineering, University of Colorado Boulder, Boulder,  
CO 80303-0596, USA

<sup>2</sup> Group Research, BASF SE, Carl-Bosch-Strasse 38, 67056 Ludwigshafen am Rhein, Germany

<sup>3</sup> BASF Coatings GmbH, Glasuritstrasse 1, 48165 Münster, Germany

<sup>4</sup> Chemetall GmbH, Trakhener Strasse 3, 60487 Frankfurt am Main, Germany

\* Correspondence to: [ratan.mishra@basf.com](mailto:ratan.mishra@basf.com), [hendrik.heinz@colorado.edu](mailto:hendrik.heinz@colorado.edu)

This PDF file includes:

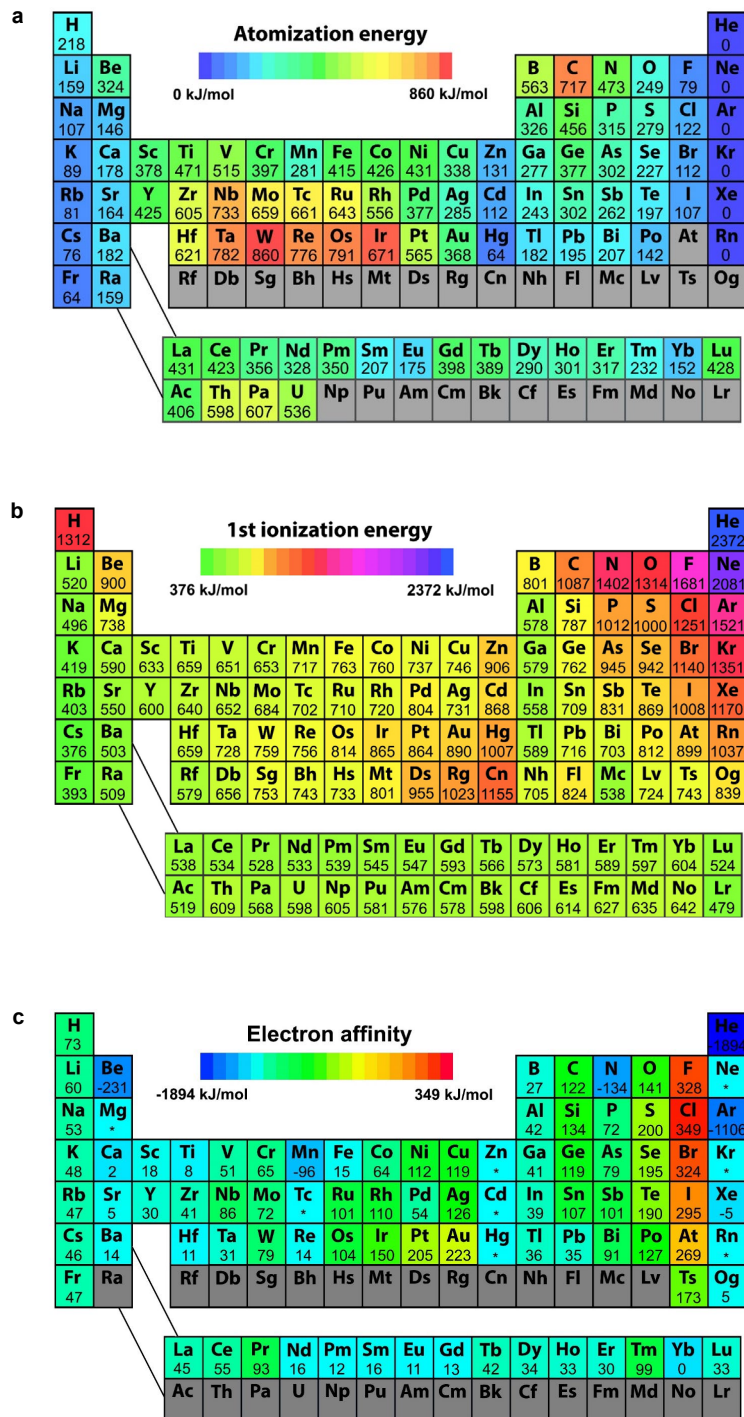
Supplementary Figures S1 to S14

Supplementary Tables S1 to S8

Supplementary Discussion Sections S1 to S6

Supplementary References

## Supplementary Figures



\* Denotes elements that are expected to have negative or near-zero electron affinities on quantum mechanical grounds.

**Figure S1.** Periodic tables of atomization energy, 1<sup>st</sup> ionization energy, and electron affinity of the elements (all data from ref. [1], reproduced with permission from ref. [2]). The data aids in assigning and validating atomic charges for molecular simulations as described in the Extended Born Model.[3] (a) The magnitude of atomization energy represents the tendency of an element towards covalent versus ionic bonding, affecting the amount of charge transfer. (b) The magnitude of the 1<sup>st</sup> ionization energy represents the ease of ionization of an element and affects the amount of positive charge of a metal species in an oxide. (c) The magnitude of the electron affinity (note: sometimes represented with opposite sign) indicates the stabilization energy by attracting a single electron and reflects the amount of negative charge accepted by the species that is a valence electron acceptor. Maxima of the electron affinity may be found for fractional charges, such as for N (-0.5e) and O (-0.6e to -0.7e) (ref. [3]). The atomization energy and ionization energy of the metal, and the electron affinity of the oxygen (or other nonmetal) in an oxide correlate with the atomic charges and molar energies of formation.[3] For example, the atomization energy of Al of 326 kJ/mol is much lower than for Si or C, but higher than for Mg and Mn, indicating atomic charges higher than Si and C, but lower than for Mg and Mn in a comparable coordination environment. The 1<sup>st</sup> ionization energy of Al is 578 kJ/mol, e.g., clearly lower than C, somewhat lower than Si, Mg, and Mn, like Ca and higher than Na. This comparison corroborates a higher charge than C as well as Mg and Mn in similar environment, some similarity to Ca and a higher charge than  $\text{Na}^+$  (as expected). Using experimental data from X-ray deformation electron densities,[3-6] multipole moments for similar compounds, these trends, and validated atomic

charges for compounds containing the mentioned nearby elements in IFF, suggest an atomic charge of approximately  $+1.5e \pm 0.1e$  for Al and  $-1.0e \pm 0.07e$  for O in alumina phases ( $+1.62e \pm 0.1e$  for Al and  $-1.08e \pm 0.07e$  for O in  $\text{Al}_2\text{O}_3$  phases in the non-bonded models).[7] The values are close to experimental data and consistent with the electronegativity difference of 1.83 relative to other compounds (Figure S2).

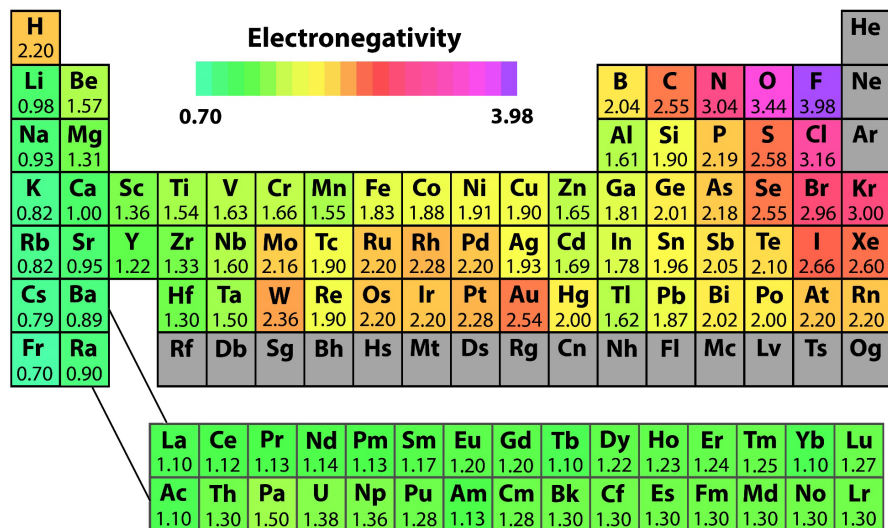


**Figure S2.** The periodic table of electronegativity according to Pauling (reproduced with permission from ref. [2]). Per definition, the square of the electronegativity difference between two elements quantifies the energy contribution to a pairwise bond due to electrostatic (non-covalent) interactions in eV (ref. [8]). The elemental electronegativity difference between O (3.44) and Al (1.61) is 1.83, which makes the Al–O bonds more ionic than covalent.

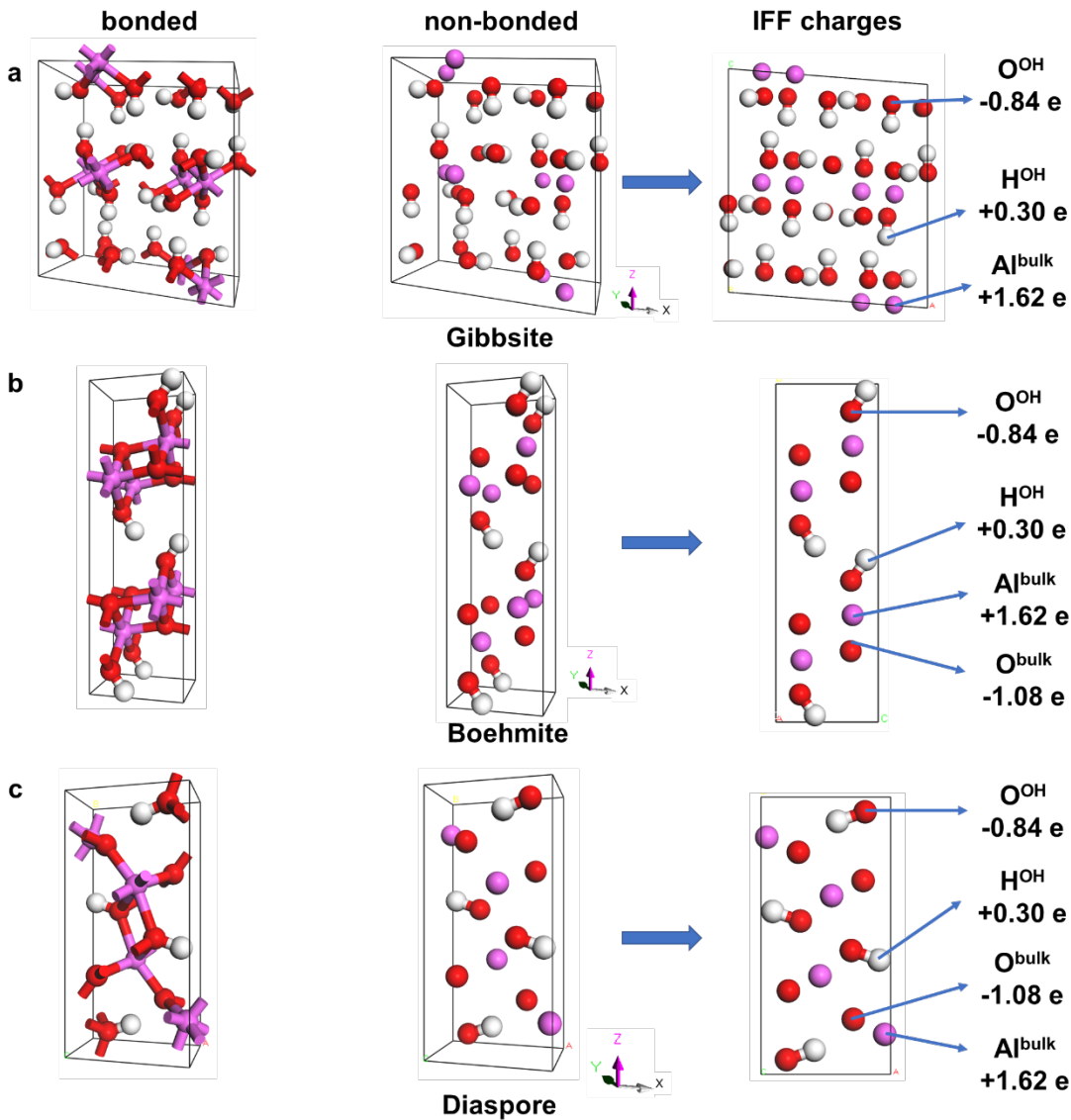


**Figure S3.** Representation of atomic charges on internal [Al O-H] groups in the minerals containing OH groups. One set of atom types is used for all minerals. (a) Gibbsite. (b) Boehmite. (c) Diaspore. When the [Al O-H] groups are exposed on external surfaces of these minerals, as well as on hydrated surfaces of  $\alpha$ -Al<sub>2</sub>O<sub>3</sub> and  $\gamma$ -Al<sub>2</sub>O<sub>3</sub>, the same atom types continue to be used but the atomic charges are reduced from -0.84e/0.30e to -0.79e/0.25e.

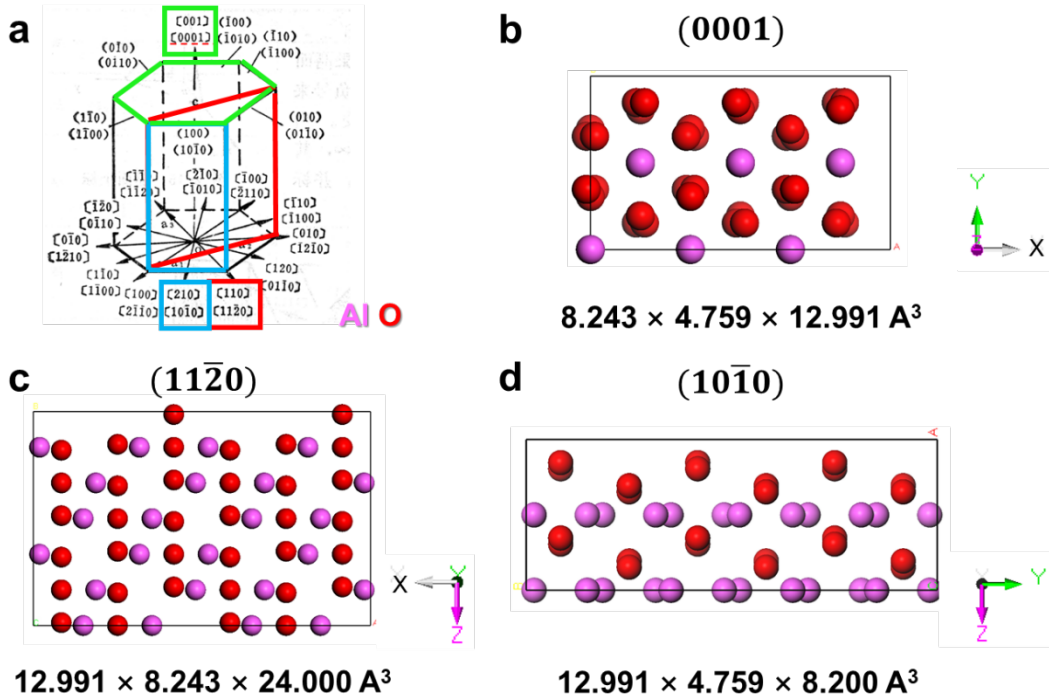


**Figure S4.** Cleavage planes in corundum (hexagonal  $\alpha$ -Al<sub>2</sub>O<sub>3</sub>). (a) Schematic of multiple cleavage planes in the hexagonal crystal system. (b) Side view of the (0001) facet. (c) Side view of the (1120) facet. (d) Side view of the (1010) facet. The corresponding supercell sizes are listed below. The corresponding calculated surface energies are listed in Table 2 in the main text.

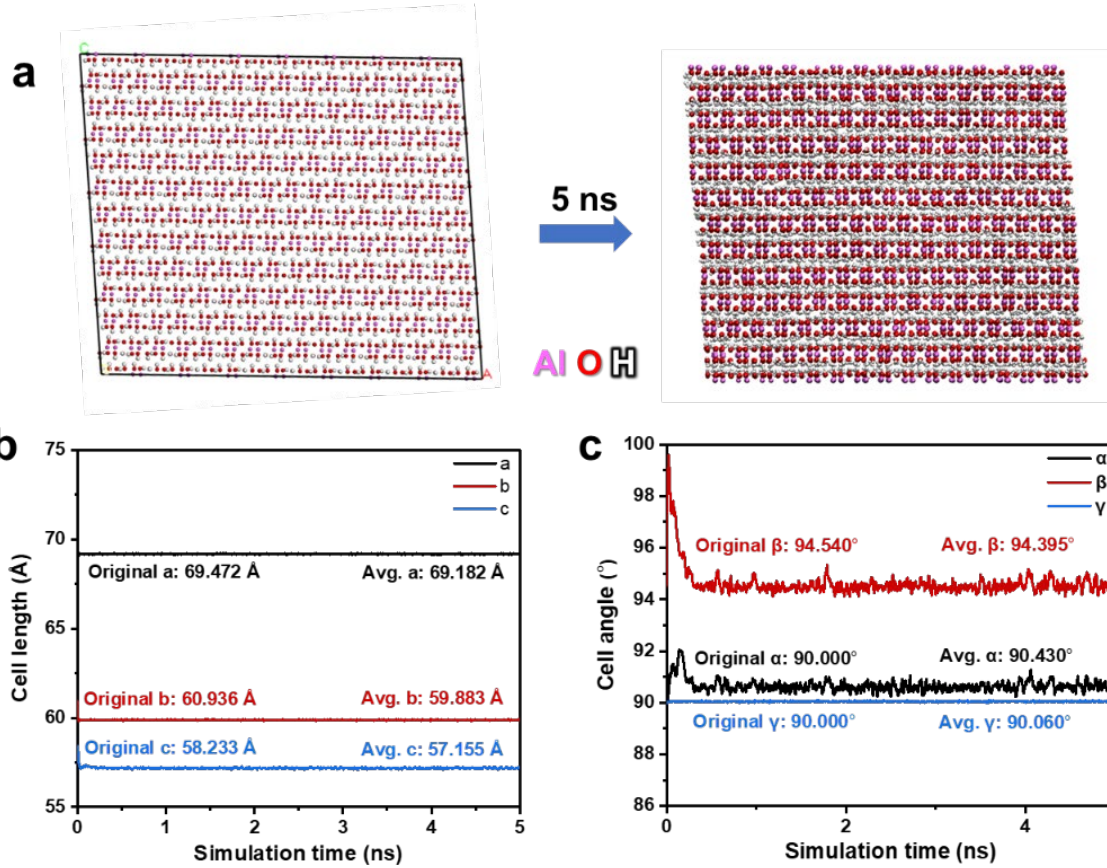


**Figure S5.** Stability of the gibbsite structures during IFF MD simulations (IFF-CVFF). (a) Starting and equilibrated structures after 5 ns for gibbsite (box size:  $69.472 \times 60.936 \times 58.416 \text{ \AA}^3$ ). (b) Values of the supercell lattice parameters  $a$ ,  $b$ ,  $c$  show high convergence as a function of simulation time. (c) Values of the cell angles as a function of simulation time, showing high convergence. We carried out MD simulations for 5 ns to ensure extensive relaxation of the lattice. Since there are only OH and Al layers inside the non-bonded models with relatively weak interactions, a large simulation cell is recommended (e.g., box size:  $69.472 \times 60.936 \times 58.416 \text{ \AA}^3$ ) to avoid sliding of atomic layers in the  $x$  and  $y$  directions. The simulated cell lengths and angles values are in very good agreement with XRD data with an average deviation  $<1\%$ .[9] Notably, for the lattice angles,

there is a sharp change at the beginning of simulations resulting from reorientation of the OH groups, which eventually return to the initial values. In addition, the simulated density is 2.52 g/cm<sup>3</sup>, only 4% higher than the experimental value 2.42 g/cm<sup>3</sup>. Achieving this agreement by direct application of IFF parameters of  $\alpha$ -Al<sub>2</sub>O<sub>3</sub> without additional adjustments provides strong proof of the high accuracy and compatibility of IFF parameters. If necessary, a higher accuracy of the density (<1% deviation) can be reached by slightly increasing the atomic charge on OH groups (e.g., +0.35e for H and -0.89e for O), presumably due to extensive internal hydrogen bonding.

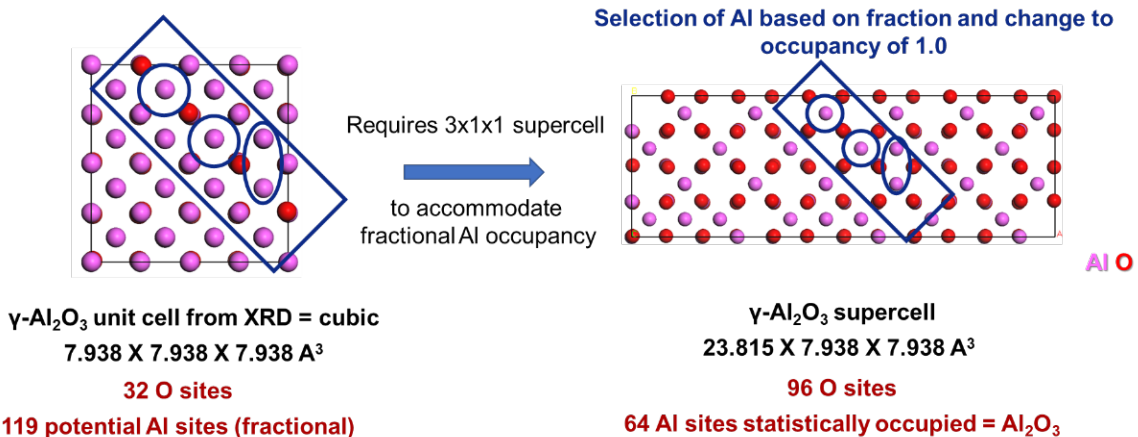


**Figure S6.** The construction of  $\gamma$ -Al<sub>2</sub>O<sub>3</sub> models for simulations. The X-ray crystal structure contains well-defined O sites and many potential Al sites with fractional occupancy.[10] A triple size unit cell is required, at minimum, to build a stoichiometric supercell in which fractionally occupied Al sites are converted into fully occupied sites. We placed Al atoms with full occupancy in statistical distribution. Many alternative distributions are possible, especially for larger cells. The effect of the statistical distribution of AL on the computed properties is hardly noticeable when the distribution of Al atoms is spatially even. More quantitatively,  $\gamma$ -Al<sub>2</sub>O<sub>3</sub> is a disordered cubic phase structure with random but stoichiometric occupancy of vacancies by Al in a well-defined oxygen lattice (32 O sites and 119 potential Al sites).[10] As the stoichiometric number of Al atoms among the fractionally occupied Al sites would be 21.33, the unit cell is not suitable for direct simulations. Larger cells and assumptions about a statistical full occupancy of Al sites are necessary to create a realistic simulation cell with Al and O in a stoichiometric ratio of 2:3. We built a  $\gamma$ -Al<sub>2</sub>O<sub>3</sub> supercell from  $3 \times 1 \times 1$  unit cells that contain 96 O sites and 357 potential Al sites. Then, we refined the structure by randomly converting 64 fractionally occupied Al sites into fully occupied Al sites. Rectangles and circles in the figure mark the portion of the structure before and

after refinement. The refined  $\gamma$ -Al<sub>2</sub>O<sub>3</sub> cell has 64 Al atoms and 96 O atoms, matching the stoichiometric ratio of 2:3.

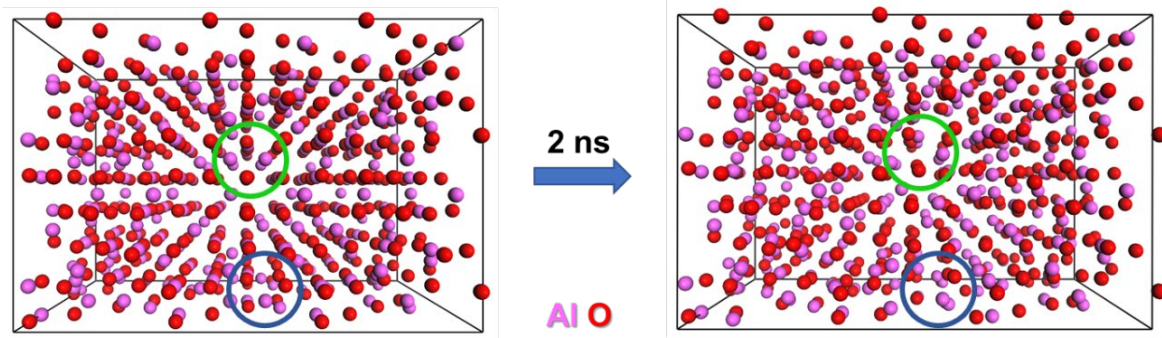


**Figure S7.** Perspective view of the starting and equilibrated structures of  $\gamma$ -Al<sub>2</sub>O<sub>3</sub> after 2 ns MD simulations with IFF-CVFF (cell size:  $23.815 \times 15.876 \times 15.876 \text{ \AA}^3$ ). After 2 ns, the positions of several Al atoms rearranged related to the random distribution and opportunity of fractional occupancy of at least 5x more potential sites (green and blue circles mark the representative regions with atomic rearrangement). These observations are consistent with XRD measurements, which indicate 357 sites of fractional occupancy by 64 Al atoms inside the lattice. The lattice has a stable structure; the surface energy and bulk modulus can be accurately calculated (Table S5).

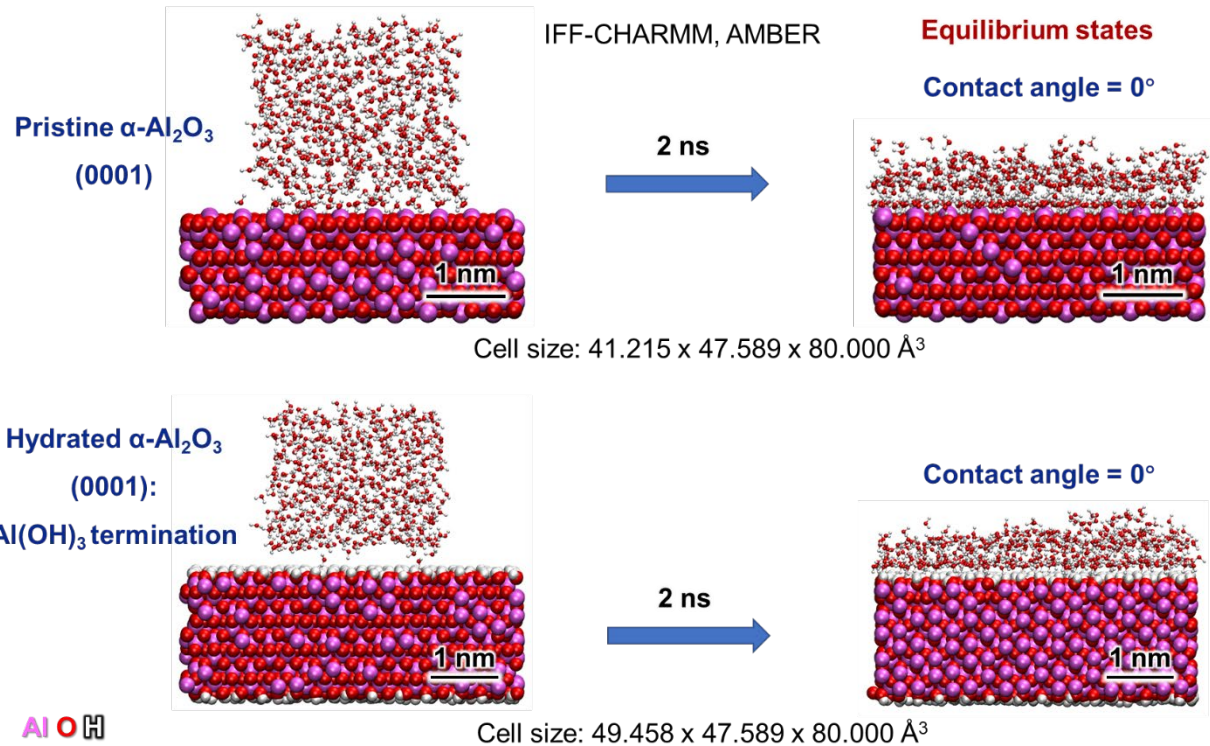
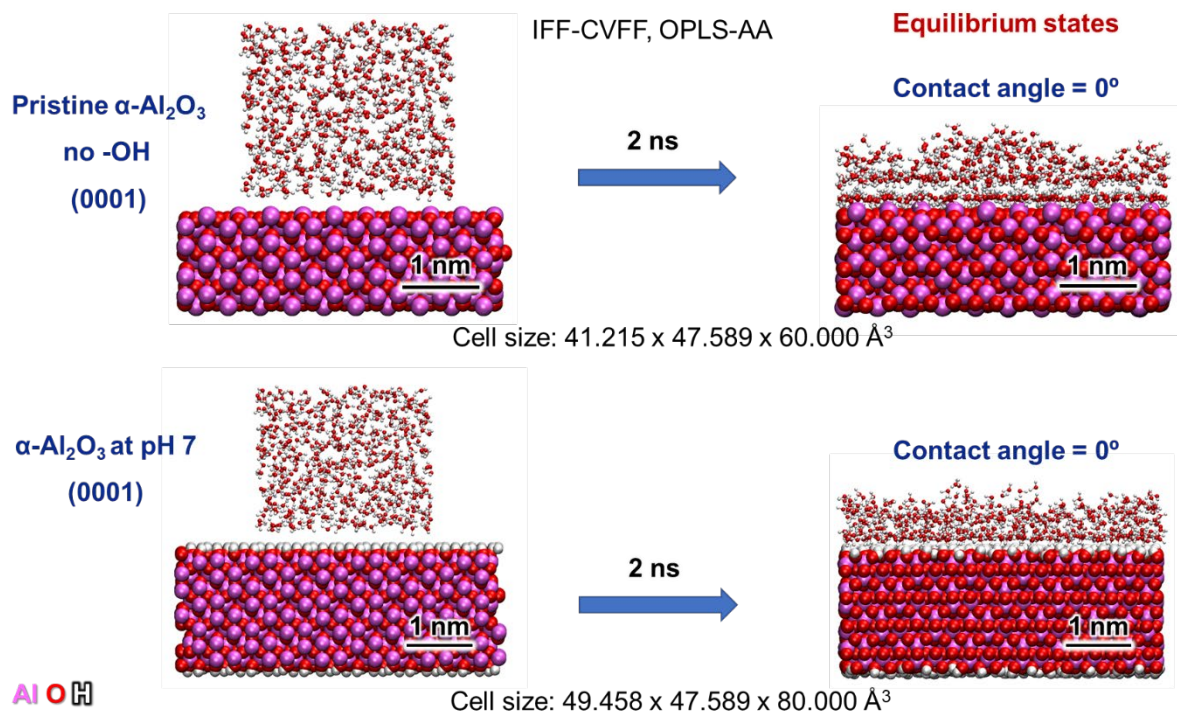


**Figure S8.** Simulated contact angle of water on pristine and hydrated  $\alpha\text{-Al}_2\text{O}_3$  (0001) surfaces at room temperature. The hydrated surface at pH 7 features an  $\text{Al(OH)}_3$  layer on top, i.e., a disordered molecular layer of gibbsite. Computed contact angles on both surfaces are  $0^\circ$ , consistent with experimental data.[11] MD simulations were carried out using IFF-CHARMM, AMBER and the flexible SPC water model (standard in IFF).



34

**Figure S9.** Simulated contact angle of water on pristine and hydrated  $\alpha\text{-Al}_2\text{O}_3$  (0001) surfaces at room temperature. The hydrated surface at pH 7 features an  $\text{Al}(\text{OH})_3$  layer on top, i.e., a disordered molecular layer of gibbsite. Computed contact angles on both surfaces are  $0^\circ$ , consistent with experimental data.[11] MD simulations were carried out using IFF-CVFF, OPLS-AA and the flexible SPC water model (standard in IFF).

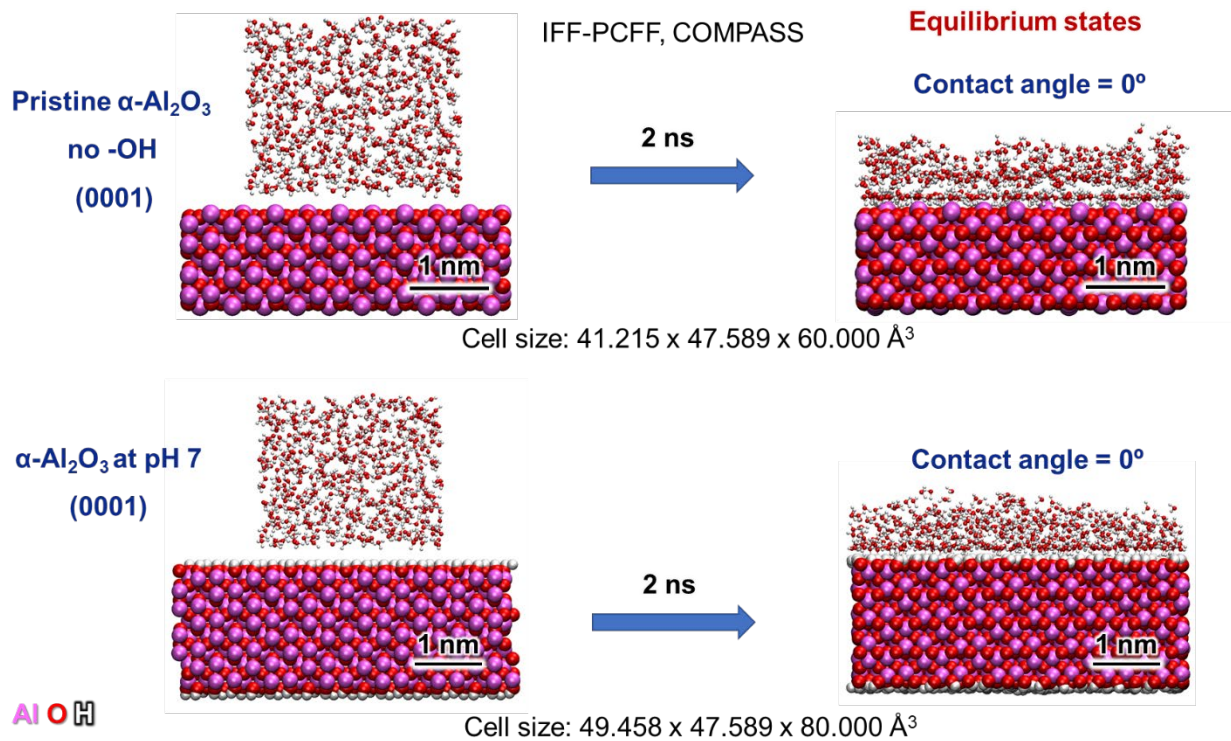
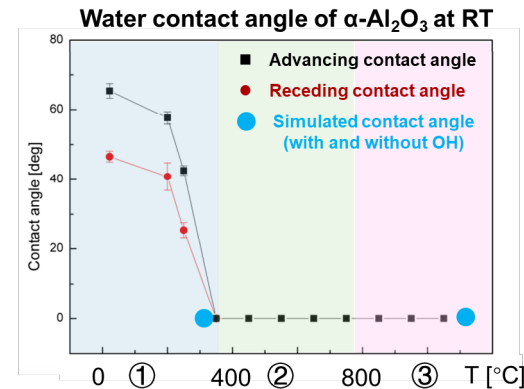
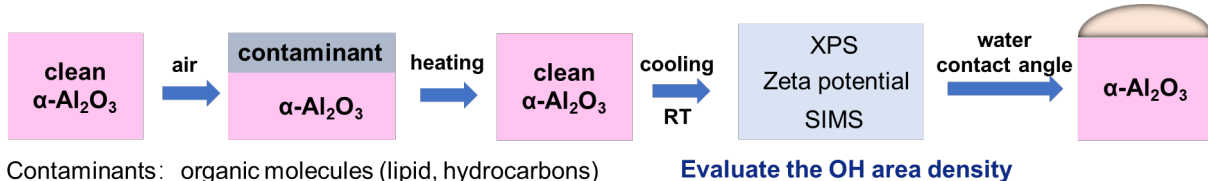


**Figure S10.** Simulated contact angle of water on pristine and hydrated  $\alpha\text{-Al}_2\text{O}_3$  (0001) surfaces at room temperature. The hydrated surface at pH 7 features an  $\text{Al}(\text{OH})_3$  layer on top, i.e., a disordered molecular layer of gibbsite. Computed contact angles on both surfaces are  $0^\circ$ , consistent with experimental data.[11] MD simulations were carried out using IFF-PCFF, COMPASS and the flexible SPC water model (standard in IFF).



- ① Decreasing contaminants on surface
- ② Clean surface with decreasing OH density (from 100% to ~20%) upon heating
- ③ Further dehydroxylation (from 20% to ~0% OH) and surface rearrangement upon further heating

**Figure S11.** Experimental measurement of water contact angle on  $\alpha\text{-Al}_2\text{O}_3$  (0001) surfaces.[11]

The presence of contaminants often leads to contact angles between  $50^\circ$  and  $60^\circ$ , which can be removed by heating or cleaning. The Al-OH groups on the surface are stable up to about  $500^\circ\text{C}$ . Contact angles reach  $0^\circ$  on clean hydrated surfaces. Above  $500^\circ\text{C}$ , the area density of Al-OH decreases due to dehydration, and a certain fraction of Al-OH groups persists above  $1050^\circ\text{C}$ . Surfaces instantly hydrate in contact with water, recreating a thin gibbsite layer.

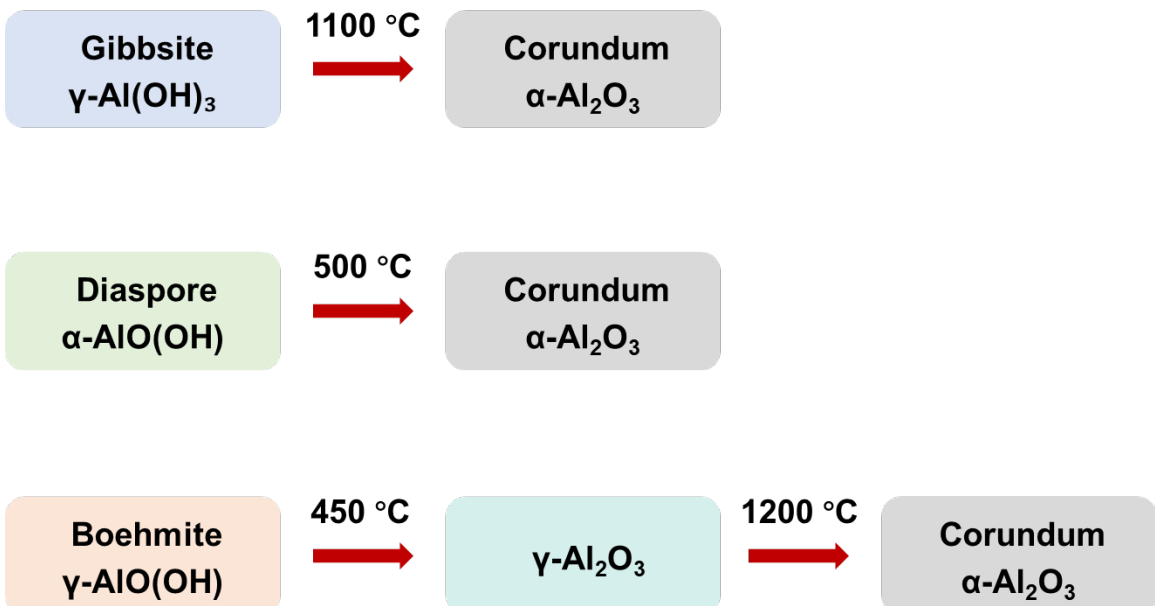


**Figure S12.** Common phase transitions of alumina phases.[12]  $\alpha\text{-Al}_2\text{O}_3$  is ultimately formed upon heating of any other oxyhydroxide phase.

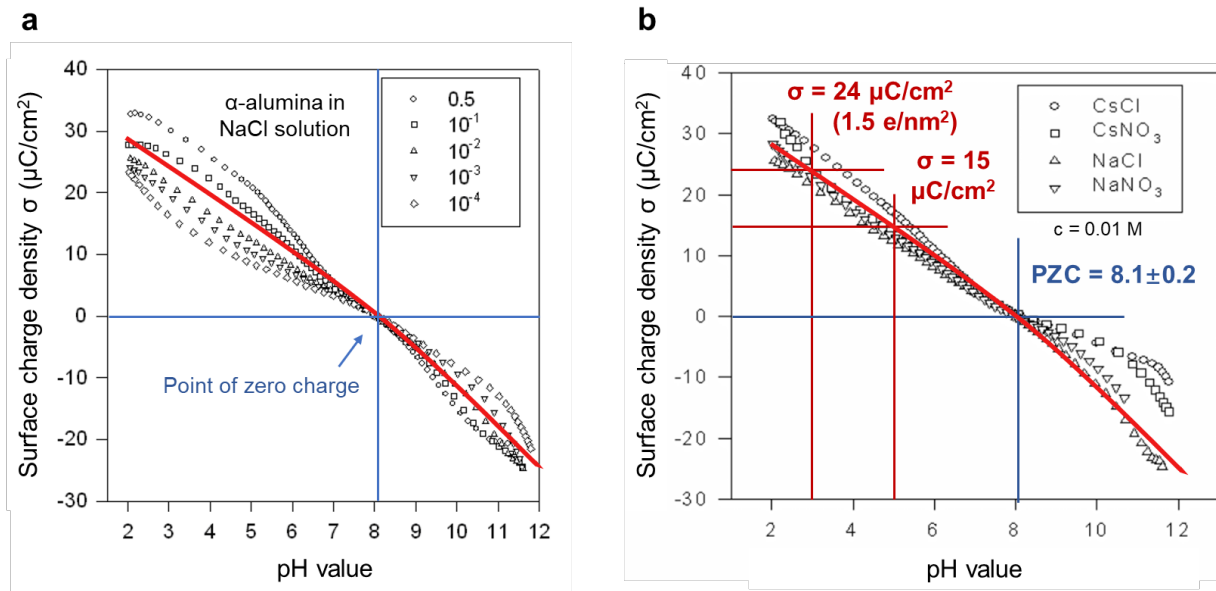


**Figure S13.** Experimental measurements of the surface charge of  $\alpha$ -alumina as a function of pH in electrolytes at different concentrations (reproduced with permission from the Bulletin of the Chemical Society of Ethiopia).[13] The data were measured by surface titration. (a) The surface charge density of  $\alpha$ -alumina as a function of pH value in aqueous NaCl solutions for multiple concentrations. Very dilute solutions of  $10^{-4}$  M NaCl to concentrated solutions of 0.5 M NaCl were tested. The red solid line represents average values to inform molecular models. The point of zero charge at pH = 8.1 is identified by two blue solid lines. (b) Measurements of the surface charge of  $\alpha$ -alumina as a function of pH value in different electrolytes at 0.01 M concentration.[13] NaNO<sub>3</sub> and NaCl lead to similar results whereas CsCl causes less ionization at high pH values due to more covalent bonding contributions of Cs<sup>+</sup> ions to the alumina surface than Na<sup>+</sup> ions. Two example readouts and the pzc are indicated. The data shown here is representative among literature reports[13-15] and includes the broadest pH ranges, which is a good reference to establish the IFF atomistic models.  $16 \mu\text{C}/\text{cm}^2 = 1.0 \text{ e/nm}^2$ . Deviations among different literature resources due to

measurement methods, ion concentration, and electrolyte types are approximately within  $\pm 5$   $\mu\text{C}/\text{cm}^2$ , or  $\pm 0.3 \text{ e}/\text{nm}^2$ .

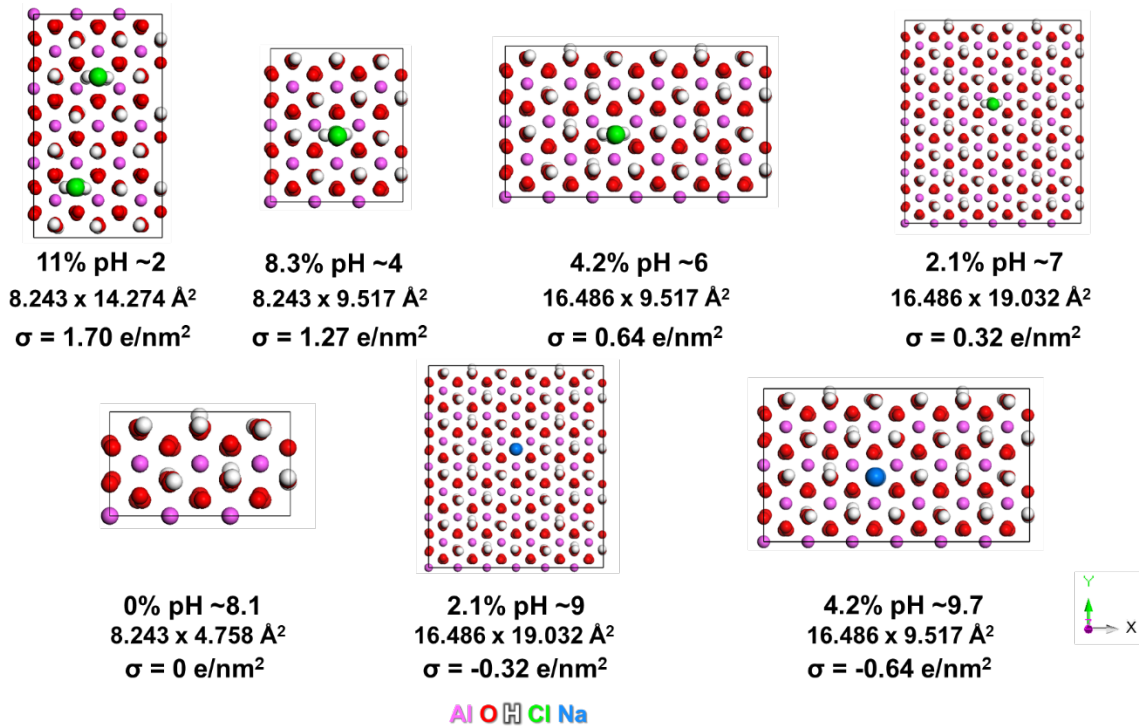


**Figure S14.** Representation of the surface chemistry of hydrated  $\alpha$ -alumina ( $\alpha$ - $\text{Al}_2\text{O}_3$  (0001))

surfaces using small repeat units. Annotations include the percentage of ionized OH groups, approximate pH value, the area of the surface, and the surface charge density ( $\sigma$ ). We recommend using larger supercells, especially for high charge densities, to allow for a statistical or otherwise intentional surface charge distribution as well as sufficient space for electrolyte and other components.

## Supplementary Tables

**Table S1.** Lattice constants, density, bulk modulus and interfacial properties of  $\alpha$ -Al<sub>2</sub>O<sub>3</sub> from experimental measurements and IFF MD simulations. Simulation results are displayed in IFF-CHARMM, IFF-cvff, and IFF-pcff, respectively.

Property	Exp.	IFF-	IFF-	IFF-	Avg. Dev. (%)
		CHARMM, AMBER	CVFF, OPLS	PCFF	
a (Å)	14.276[16]	14.279	14.217	14.322	0.25
b (Å)	14.276	14.282	14.217	14.315	0.24
c (Å)	12.991	12.990	13.070	12.932	0.36
$\alpha$ (°)	90.00[16]	89.99	90.00	89.97	0.02
$\beta$ (°)	90.00	90.00	90.00	90.00	0
$\gamma$ (°)	120.00	119.98	119.99	119.96	0.02
RMSD (Å)	N/A	0.15	0.14	0.16	N/A
Density (g/cm <sup>3</sup> )	3.986[16]	3.986	3.996	3.980	0.13
Surface energy	1.65±0.05[7,	1.65	1.67	1.65	1.8

(J/m <sup>2</sup> )	17]				
(0001)					
(11 $\bar{2}$ 0)	N/A <sup>a</sup>	1.88	1.85	1.86	N/A
Bulk modulus (GPa)	254±3[18, 19]	265	273	207	10.1
Water contact angle (°)	~0[11], <sup>b</sup> 0	0	0	0	0

<sup>a</sup> Some data on surface energies have been reported for both facets using DFT calculations, indicating the same trends ((0001)<(11 $\bar{2}$ 0)<(10 $\bar{1}$ 0)).[20] <sup>b</sup> The contact angle is moderately hydrophilic in laboratory atmosphere due to surface contamination and reduces to 0° upon cleaning the surfaces or heating to about 350 °C. Thermal treatment up to 350 °C removes organic contaminants but does not remove Al-OH groups on the surfaces, which requires temperatures above 500 °C.[11] Pure oxide surfaces terminated by Al or O (without OH) groups are also hydrophilic with a contact angle of 0° and the presence of water rapidly leads to hydration reactions with Al(OH)<sub>3</sub> surface layers.

**Table S2.** The experimental and calculated lattice parameters and surface energy of boehmite,  $\gamma$ -AlO(OH), using molecular dynamics simulation with IFF parameters.

Property	Exp.	IFF- CHARMM, AMBER	IFF- CVFF, OPLS	IFF- PCFF	Avg. Dev. (%)
<b>Lattice a (Å)</b>	28.760[21]	29.22	28.92	29.11	1.1
<b>Lattice b (Å)</b>	24.480	25.55	24.76	24.61	2.0
<b>Lattice c (Å)</b>	14.836	14.65	14.58	14.58	1.6
<b><math>\alpha</math> (°)</b>	90.000[21]	89.90	89.85	89.92	0.12
<b><math>\beta</math> (°)</b>	90.000	90.01	89.98	90.04	0.03
<b><math>\gamma</math> (°)</b>	90.000	89.27	90.36	90.09	0.44
<b>RMSD (Å)</b>	N/A	0.6	0.5	0.46	N/A
<b>Density (g/cm<sup>3</sup>)</b>	3.03[21]	2.90	3.03	3.04	1.5
<b>Surface energy (J/m<sup>2</sup>)</b>	(001) most likely: <sup>a</sup> ~0.9; DFT: <sup>b</sup> 0.96±0.12[22, 23] Experiment: 0.52 (facet average)[23]	0.86	0.95	0.86	~5

	(010) DFT: <sup>b</sup> 0.28±0.02[20, 24]	0.17	0.24	0.25	NA
<b>Bulk modulus (GPa)</b>	Likely: 100±10 <sup>c</sup>  Expt: 98[25] <sup>d</sup> and  110±15[26] <sup>e</sup> , DFT:  82-97 [27]	95	100	70	~10

<sup>a</sup> Given well-known surface energies for  $\alpha$ -Al<sub>2</sub>O<sub>3</sub> of 1.69 J/m<sup>2</sup>, for MgO of 0.95 J/m<sup>2</sup> and surface energies much lower of hydroxides such as Mg(OH)<sub>2</sub> of 0.225 J/m<sup>2</sup> that are closely reproduced by IFF,[7] a surface energy of ~0.9 J/m<sup>2</sup> appears to be reasonable for  $\gamma$ -AlO(OH). <sup>b</sup> DFT calculations are not a reliable reference (50% deviation not uncommon).[7] <sup>c</sup> The experimental bulk modulus is somewhat uncertain to-date, see references and interpretations below. <sup>d</sup> Ref. [25] reports bulk moduli for boehmite nanotubes at 98 GPa. <sup>d</sup> Ref. [26] reports predominantly high-pressure data at 5-50 GPa. At low to medium pressure (0 to 3 GPa), the reported compressibility points to a bulk modulus between 95 and 120 GPa (Figure 5a in ref. [26]). As the bulk modulus would require more data near zero pressure, the error bars remain high at 110 ±15 GPa. Extrapolation from high pressure moduli from 0 to 50 GPa are 135 GPa.

**Table S3.** Experimental and calculated lattice parameters and surface energies of diaspore,  $\alpha$ -AlO(OH), using IFF models and parameters. The lattice parameters  $a$  and  $b$  using IFF-CHARMM parameters showed large differences from experiments of +10% and +5%, which may be remedied by specific modifications of the OH parameters.

Property	Exp.	IFF-CHARMM, AMBER	IFF-CVFF, OPLS	IFF-PCFF	Avg. Dev. (%)
<b>Lattice a (Å)</b>	17.604[4]	19.25	17.91	17.76	4.0
<b>Lattice b (Å)</b>	18.842	17.92	18.68	18.47	2.6
<b>Lattice c (Å)</b>	14.225	14.33	14.43	14.56	1.5
<b><math>\alpha</math> (°)</b>	90.000[4]	90.02	90.35	90.06	0.16
<b><math>\beta</math> (°)</b>	90.000	89.58	89.91	90.55	0.39
<b><math>\gamma</math> (°)</b>	90.000	90.21	89.88	89.53	0.30
<b>Density (g/cm<sup>3</sup>)</b>	3.38[4]	3.23	3.31	3.34	2.6
<b>Surface energy (J/m<sup>2</sup>)</b>	(001) N/A	1.21	1.2	1.3	NA
	(100) N/A	1.10	1.22	1.32	NA

<b>Bulk modulus (GPa)</b>	Likely: 120; 90±20,[28] <sup>a</sup> 134,[29] <sup>b</sup> 120[30], <sup>c</sup> high p:140- 156[30][31] <sup>d</sup>	107	115	86	-15
-------------------------------	--	-----	-----	----	-----

<sup>a</sup> The high pressure study in ref. [28] shows a steep slope at low pressure below 1 GPa, suggesting a bulk modulus of  $90 \pm 20$  GPa (Figure 2 and Table 1 in ref. [28]). At higher pressures up to 20 GPa, the slope flattens considerably. <sup>b</sup> Most studies have difficulties accurately measuring the volume response below 0.5 GPa or 1 GPa stress. <sup>c</sup> Bulk moduli down to 120 GPa have been reported at low stress.[30] At higher stress, 140-153 GPa were observed. <sup>d</sup> At high pressures up to 50 GPa, extrapolations also suggest 140-153 GPa[30] and 146-156 GPa.[31]

**Table S4.** The experimental and calculated bulk properties of gibbsite,  $\gamma$ -Al(OH)<sub>3</sub>, using IFF models and parameters. The lattice parameters  $a$  and  $b$  using IFF-PCFF parameters showed notable differences from experiment of +4% and +2.5%. The surface energy with IFF-OPLS/CVFF appears to be somewhat overestimated. Specific modifications of the OH parameters could remedy the differences.

Property	Exp.	IFF-CHARMM	IFF-OPLS/CVFF	IFF-PCFF	Avg. Dev. (%)
<b>Lattice a (Å)</b>	69.472[9]	70.85	69.18	72.26	2.1
<b>Lattice b (Å)</b>	60.936	61.10	59.88	62.54	1.5
<b>Lattice c (Å)</b>	58.233	58.15	57.16	57.79	0.92
<b><math>\alpha</math> (°)</b>	90.000[9]	90.00	90.43	90.35	0.29
<b><math>\beta</math> (°)</b>	94.540	94.44	94.40	94.64	0.12
<b><math>\gamma</math> (°)</b>	90.000	90.00	90.06	90.10	0.06
<b>Density (g/cm<sup>3</sup>)</b>	2.42[9]	2.38	2.52	2.29	3.7
<b>Surface energy (J/m<sup>2</sup>)</b>	(001) DFT: <sup>a</sup> 0.29[24]	0.29	0.30	0.27	~5
<b>Bulk modulus (GPa)</b>	Est. 30-35 <sup>b</sup> Low pressure: 36[32] High pressure: 49[32] 70-85[33] <sup>c</sup>	30	32	21	~15

<sup>a</sup> DFT calculations are not a reliable reference (50% deviation not uncommon), even though good agreement is found here. <sup>b</sup> Gibbsite,  $\gamma$ -Al(OH)<sub>3</sub>, is a soft mineral, easily scratched by a knife. It has perfect cleavage in the (001) plane, which consists of 2D planes of OH groups on both sides. A complex response to pressure has been found experimentally and the bulk modulus is likely the same or lower than for Mg(OH)<sub>2</sub> (45 GPa[7]) or Ca(OH)<sub>2</sub> (35 GPa[7]), which have a similar structure and lower density of (OH) groups per metal atom. The experimental data by Liu et al.[32] from 0 to 0.7 GPa compressive stress (425.2 Å<sup>3</sup> to 416.9 Å<sup>3</sup>) suggest  $B = 36$  GPa. At lower pressure (0.1 GPa or less), the value is likely to decrease, leading to our estimate of 30-35 GPa. Measurements on high pressure phases yielded bulk moduli from 49 GPa[32] up to 85 GPa,[33] which relate to the response under a pressure of many GPa, which leads to different Al(OH)<sub>3</sub> phases.

**Table S5.** The experimental and calculated bulk properties of  $\gamma$ -Al<sub>2</sub>O<sub>3</sub> using IFF parameters and refined structures. A  $3 \times 1 \times 1$  supercell was used to account for the statistical occupancy of Al atoms of many possible lattice sites. The positions of O atoms are uniquely determined.[10]

Property	Exp.	IFF- CHARMM	IFF- OPLS/CVFF	IFF- PCFF	Avg. Dev. (%)
<b>Lattice a (Å)</b>	23.815[10]	23.97	24.08	23.91	0.72
<b>Lattice b (Å)</b>	15.876	15.99	15.88	16.00	0.50
<b>Lattice c (Å)</b>	15.876	16.01	15.83	15.93	0.51
<b><math>\alpha</math> (°)</b>	90.000[10]	89.42	90.13	89.70	0.37
<b><math>\beta</math> (°)</b>	90.000	89.67	89.88	89.50	0.35
<b><math>\gamma</math> (°)</b>	90.000	90.12	89.93	89.88	0.11
<b>RMSD (Å)</b>	N/A	0.17	0.18	0.16	N/A
<b>Density (g/cm<sup>3</sup>)</b>	3.65[10]	3.53	3.58	3.55	2.65
<b>Surface energy (J/m<sup>2</sup>)</b>	(001) 1.66±0.1[23]	1.69	1.74	1.57	4
<b>Bulk modulus</b>	162	162	206	143	13

**Table S6.** The experimental[18] and simulated elastic constants of  $\alpha$ -Al<sub>2</sub>O<sub>3</sub> using IFF-CVFF, OPLS-AA. The agreement is excellent for the shear modulus and Poisson ratio, and very good for the principal components. Values for less common shear-normal coupling such as C<sub>14</sub> diverge and could be uncertain in experiments.

$\alpha$ -Al <sub>2</sub> O <sub>3</sub>	<b>Shear modulus (GPa)</b>	<b>Poisson ratio</b>	<b>Elastic constant (GPa)</b>						
			<b>C<sub>11</sub></b>	<b>C<sub>33</sub></b>	<b>C<sub>44</sub></b>	<b>C<sub>66</sub></b>	<b>C<sub>12</sub></b>	<b>C<sub>13</sub></b>	<b>C<sub>14</sub></b>
Exp.	165	0.24	497.0	501	147.0	167.5	163	116	22.0
IFF- CVFF	155.1	0.26	471.1	517.3	117.2	140.4	179.6	162.7	8.8
Dev. (%)	-6.0	8.3	-5.2	3.3	-20.3	-16.2	10.2	40.2	-60.0

**Table S7.** The surface charge density of  $\alpha$ -alumina as reported from acid-base titration in different units.[13] Measurements in  $\mu\text{C}/\text{cm}^2$  are converted into the number of charged sites per  $\text{nm}^2$ , and the percentage of affected OH surface groups, assuming a (001) or (0001) plane with  $\text{Al(OH)}_3$  groups. Surface charge densities of  $+0.5 \text{ e}/\text{nm}^2$  and  $+1.5 \text{ e}/\text{nm}^2$ , for example, lead to triple the charge density and qualitatively different water interfacial structure and binding of molecules, especially when containing ionic groups. The surface is electroneutral near  $\text{pH } 8.1 \pm 0.2$ [13, 15] (other studies report a range from  $\text{pH } 7$  to  $9$ ).[14] Negatively charged surfaces at  $\text{pH}$  values larger than  $9$  lead to attraction of oppositely charged molecules. These major differences in nanoscale behavior have been largely neglected in prior simulations and are critical for predictive simulations. Different phases of alumina and oxyhydroxides exhibit semi-quantitatively the same surface chemistry, point of zero charge, and surface terminations.

<b>pH values</b>	<b>Exp.</b>	<b>Exp.</b>	<b>Percentage of <math>\text{Al(OH)}_3</math> surface groups ionized<sup>b</sup></b>
	<b>Surface charge density</b> ( $\mu\text{C}/\text{cm}^2$ )[13, 14] <sup>a, b</sup>	<b>Surface charge density</b> ( $\text{e}/\text{nm}^2$ ) <sup>c</sup>	
<b>2 (diss.)</b>	$28 \pm 2$	$1.75 \pm 0.1$	$\sim 12\%$
<b>3 (diss.)</b>	$24 \pm 2$	$1.5 \pm 0.1$	$\sim 10\%$
<b>4 (diss.)</b>	$19 \pm 2$	$1.2 \pm 0.1$	$\sim 8\%$
<b>5</b>	$15 \pm 2$	$0.9 \pm 0.1$	$\sim 6\%$
<b>6</b>	$10 \pm 2$	$0.6 \pm 0.1$	$\sim 4\%$

7	5 $\pm$ 2	0.3 $\pm$ 0.1	$\sim$ 2%
8.0-8.2	0 $\pm$ 2 (pzc at 8.1 $\pm$ 0.2)	0 $\pm$ 0.1	0
9	-5 $\pm$ 2	-0.3 $\pm$ 0.1	$\sim$ 2%
10 (diss.)	-12 $\pm$ 2	-0.75 $\pm$ 0.1	$\sim$ 5%
11 (diss.)	-18 $\pm$ 2	-1.1 $\pm$ 0.1	$\sim$ 8%
12 (diss.)	-24 $\pm$ 2	-1.5 $\pm$ 0.1	$\sim$ 10%

<sup>a</sup> Surface charge density of  $\alpha$ -Al<sub>2</sub>O<sub>3</sub> in NaCl solution at a concentration of 0.1 M NaCl from ref. [13]. The values remain similar in a broader concentration range  $<10^{-4}$  M to  $>0.5$  M in good approximation. NaNO<sub>3</sub> solutions show similar data within  $\pm 2$   $\mu$ C/cm<sup>2</sup>. <sup>b</sup> CsCl solutions, also included in ref. [13], show slightly higher positive surface charge at low pH (ca. +31  $\mu$ C/cm<sup>2</sup> at pH = 2) and a lower negative surface charge at high pH (ca. -15  $\mu$ C/cm<sup>2</sup> at pH = 12). A lower negative surface charge density at high pH values likely results from covalent-type bonding of Cs<sup>+</sup> ions to OH<sup>-</sup> ions in solution (Cs<sup>+</sup> has a typical atomic charge of only +0.6e to +0.7e),[3] thereby reducing the amount of OH<sup>-</sup> ions available in solution to form AlO<sup>-</sup> groups from AlOH groups. In contrast, Na<sup>+</sup> ions are fully ionic in solution (+1.0e), form no complexes with OH<sup>-</sup> ions and enable the maximum activity of OH<sup>-</sup> ions to form AlO<sup>-</sup> sites. Consistent with this interpretation, the surface charge density of  $\alpha$ -Al<sub>2</sub>O<sub>3</sub> at low CsCl concentrations of 10<sup>-4</sup> M is identical to that in 10<sup>-4</sup> M NaCl solution (see Figure S13). <sup>c</sup> Unit conversion from  $\mu$ C/cm<sup>2</sup>. <sup>d</sup> We assume an area density of 15.3 or 13.6 OH groups per nm<sup>2</sup> as found in hydrated (0001)  $\alpha$ -alumina and (001) gibbsite, respectively.

**Table S8.** The percentage of ions dissociated from  $\alpha$ -alumina surfaces at various pH values according to MD simulations, along with the density per area. Below pH 8, the groups include  $\text{Al}(\text{OH}_2)^+$   $\text{Cl}^-$ , at pH 8 there were no charged groups (pzc), and above pH 8, the groups include  $\text{AlO}^-$   $\text{Na}^+$ . The fraction of dissociated ions is larger at lower total surface charges (near the pzc) than at high surface charge, and chloride ions tend to dissociate further than sodium ions. The data are averaged over the last 75 ns of 100 ns simulation time and uncertainties are  $\pm 5\%$  of the given values.

pH	Ion species	Dissociated ( $> 5 \text{ \AA}$ )	Total area density of ions ( $\text{nm}^{-2}$ )	Area density of dissociated ions ( $\text{nm}^{-2}$ )
2	$\text{Cl}^-$	13 %	1.87	0.25
5	$\text{Cl}^-$	45 %	0.85	0.38
8	None	None	0	0
10	$\text{Na}^+$	13 %	0.85	0.11
12	$\text{Na}^+$	8 %	1.53	0.12

## Supplementary Discussion

### S1. Prior Validation of the Interface Force Field (IFF)

IFF is a class I force field, that is, a combination of electrostatics, Lennard-Jones, and bonded terms, as is commonly used in MD simulations. It includes 12-6 and 9-6 options for Lennard-Jones parameters for most compounds. The concept of IFF has been briefly described in the main text and in detail in the introductory publication.[34] In comparison to other force fields, like OPLS-AA, CHARMM, and others, IFF uses a more quantitative, consistent approach for a wider range of chemistries that leads to order-of-magnitude higher accuracy, i.e., inorganic, organic compounds, and biomaterials. The combination of different compounds, and IFF with other force fields work well because the parameters for each material separately reproduce internal multipole moments, molecular/lattice geometry, as well as the surface energy and interactions with other molecules. IFF builds on a self-consistent classical Hamiltonian for each validated compound, which enables a high degree of compatibility and transferability. In addition, IFF uses only one interpretable set of parameters, which lowers the uncertainty in model assumptions (also called epistemic uncertainty).[35] This approach contrasts grey-box and black-box approaches with many different parameter sets for the same physical systems, for example, as in density functionals and ReaxFF.

The protocol of IFF development is to step by step validate the atomic charge, bonded terms (bond, angle, and dihedral values and constants), Lennard-Jones parameters, structural and surface properties, leading to estimations of bulk and interfacial properties with accuracy over 95%

compared to experimental measurements.[34] The rigorous validations and consistent protocols for IFF development guarantee high accuracy, interpretability, compatibility and transferability. IFF has been extensively validated and applied for MD simulations of bulk materials and inorganic-organic interfaces, including specific molecular recognition, self-assembly, dynamics, competitive adsorption, electrolyte interfaces, crystal growth, and reactivity at interfaces.[36-41]

## **S2. The Limitations of Bonded Models**

The major limitation of bonded models lies in the complex bond connections inside the atomic models, especially compounds with more than 6 bond connections for an atom, which require an extensive and complete set of bonded terms in the force field file to carry out a successful molecular dynamics simulation. The definition and validation of the bonded terms, e.g., settings for bond, angle, and dihedral equilibrium values and force constants, even when they are given by crystal structures, vibration spectra, and require no actual parameter search, is very time consuming. In addition, the atomic charges and Lennard-Jones parameters require thorough analysis to reproduce key bulk and interfacial properties for validation, including lattice constants, density, surface energy, water contact angle, adsorption energy, and mechanical properties.

When modifications are needed in the system, such as a change from oxide ions to hydroxide ions, elemental doping, and surface hydration to Al-OH groups, it is even more challenging to use bonded models due to the introduction of new atoms, known or unknown new bond topology. Any new bond, element, or force field type of an existing element requires a new set of bond, angle,

dihedral, and possibly out of plane (improper) parameters and force constants. The known structure and chemical analogy often helps in finding the added parameters quickly, however, the sheer number of necessary terms can feel discouraging. We believe this may be a reason why many researchers seek help from density functional theory (DFT) calculations with oversimplified systems, accepting losses in accuracy, and neglect the necessary dynamics.

The definition of bonded terms is a challenge of the entire MD simulation field, and there have been very limited solutions. We recognize, however, several opportunities: (1) Predominantly covalent compounds such as organic and biological matter composed of carbon, nitrogen, oxygen, and hydrogen usually has low coordination numbers (1 to 4), which does not introduce a huge number of bonded terms. Also, analogy considerations to derive bonded terms, which for the most part have clear starting points in experimental data and involve narrow physical ranges for optimization, can be taught to AI-based agents for automatic presentation, reducing the workload of the researcher. (2) Predominantly ionic compounds, or about half ionic compounds, such as alumina, salts, and several other oxides have higher coordination numbers, which lead to an exponential increase in angle and torsion terms if the bonded interactions are included.[42, 43] From a physical viewpoint, however, these terms become increasingly redundant as interactions are mostly ionic and represented by nonbonded terms. Therefore, great benefit arises from using nonbonded models which eliminate the entire batch of bonded parameters and introduce much greater flexibility. If needed to reproduce the equilibrium structure in borderline cases, bonded terms can still be utilized. However, when bonding is clearly more covalent than ionic, e.g., in

silica, zirconia, and other oxides, the use of nonbonded parameters without bonded terms is unphysical. Charges that are higher than chemically realistic values are necessary, even if nonbonded models may give qualitatively usable results for some properties. (3) Overall, the entire parameterization process for different phases is at least ten times faster with non-bonded models (1 week for beginners) than with bonded models ( $> 10$  weeks). Experts can handle either process within 1 day to 3 days. In the big picture, the advantages of the non-bonded models surpass minor limitations.

For either type of protocol, bonded or nonbonded, there is opportunity to utilize AI as a guide to accelerate the parameterization process. The thought patterns, identification and retrieval of suitable reference data for IFF, as well as the battery of test simulations for validation are too complex, however, for full automation in the foreseeable future.

### **S3. Further Details on Non-bonded Models, Advantages, and Limitations**

The nature of chemical bonding in oxides is governed by the chemical environment and intrinsic atomic properties, such as atomization energy, ionization energy, and electronegativity.[44, 45] Based on the extent of valence electron transfer, metal-oxygen bonds in oxides can be broadly categorized as covalent, ionic, or intermediate (covalent/ionic).[46, 47] Typical covalent-dominated oxides include  $\text{SiO}_2$ ,  $\text{CeO}_2$ ,  $\text{MnO}_2$ ,  $\text{TiO}_2$ ,  $\text{ZrO}_2$ , and  $\text{MoO}_3$ . Ionic-dominated oxides include  $\text{CaO}$ ,  $\text{MgO}$ ,  $\text{CoO}$ , and  $\text{Na}_2\text{O}$ , while mixed-bonding compounds such as  $\text{Al}_2\text{O}_3$ ,  $\text{V}_2\text{O}_3$ , and

$\text{Fe}_2\text{O}_3$  exhibit both covalent and ionic character. In general, increased ionic character correlates with higher chemical reactivity.

In this context, it is chemically justified to represent ionic and mixed ionic/covalent oxides using non-bonded models in molecular dynamics (MD) simulations. These models eliminate explicit bond connections among atoms and instead rely on electrostatic interactions between positively and negatively charged species to reflect valence electron transfer. This approach is conceptually similar to modeling metallic bonding in FCC metals, where atoms interact without net charge transfer.[48] In non-bonded models, all bonded terms are omitted—except for surface hydroxyl (OH) groups where needed—greatly simplifying the parameterization process.

Validated non-bonded models offer accurate predictions (typically >95% agreement with experiments) for key bulk and interfacial properties, including lattice constants, density, bulk modulus, surface energy, water contact angle, and adsorption energy. Notably, surface energies—which are often difficult to capture by bonded models due to bond constraints—can be readily calculated using non-bonded models. Elemental doping is easily implemented by substituting existing atoms with desired anions or cations while maintaining stoichiometry. Surface hydroxylation can also be customized to match experimental surface chemistry. Moreover, because bonded terms are absent, the same force field parameters can often be transferred to other polymorphs of the same compound without requiring reparameterization. Nonbonded force fields also often perform to compute vibration spectra.

Despite these advantages, non-bonded models have reduced compatibility across different force fields (e.g., CHARMM, CVFF, PCFF). This is primarily due to differences in mixing rules for 12-6 Lennard-Jones potentials—e.g., arithmetic mean for  $r_{min}$  in CHARMM, AMBER, and DREIDING, geometric mean for CVFF and OPLS-AA. To address this issue, slight modifications to the IFF LJ parameters were made to ensure compatibility with various force field formats and simulation packages (see Table 1). Bonded models would usually work fine in either of these formats. When using a different LJ potential, such as 9-6 LJ in IFF-PCFF, both bonded and nonbonded force fields require different LJ parameters due to a change in mathematical form and using Waldman-Hagler combination rules.[49]

#### **S4. Interpretation of Force Field Parameters for the Alumina Phases**

The ability to describe a structurally diverse set of minerals using a single parameter set highlights the robustness of the chemical information embedded in the IFF parameters (Table 1). It also demonstrates that minor variations in coordination environments do not necessitate complex polarizable models or additional empirical fit parameters, as previously suggested.[50, 51] The key lies in accurately representing bonding through experimentally and theoretically backed atomic charges, along with validating structures and energies—a unique principle of IFF and IFF-R.[34]

The Lennard-Jones (LJ) and bonded parameters for O-H groups remain the same for all hydroxide bulk phases and for OH surface groups of all minerals, and are similar to those of other

oxides.[7] This assumption is practical and sufficiently accurate, however, the atomic charges require more detailed consideration. The assigned values are essential in representing interactions in the bulk minerals and at surfaces, including ionization as a function of pH value (Figure 3 and Table 1). Across pH values from 0 to 14, the presence of  $\text{AlOH}_2^+ \cdots \text{Cl}^-$ ,  $\text{AlOH}$ , and  $\text{AlO}^- \cdots \text{Na}^+$  groups on the surface modifies zeta potentials and charge density on the surface across orders of magnitude, changing water interfaces, types of attracted charged and functional groups in molecules, and polyelectrolyte interactions.

To represent these effects, we differentiate between two atomic charge settings for OH groups based on their chemical environment, “bulk” and “surface” (Table 1). In gibbsite, boehmite, and diaspore, bulk AlOH groups inside the crystal lattice carry a charge of +0.30e on H atoms and -0.84e on the O atoms (Figure 3a). This charge distribution reflects the binding strength and acidity of the H atoms. For example, the OH bond strength in AlOH groups is greater compared to SiOH groups, and the acidity weaker than in SiOH groups (pK of ~8.4 for alumina phases versus ~3 for silica). As a result, the H charge in AlOH groups of +0.3e is lower than in SiOH groups with a H charge of +0.4e and an O charge of -0.675e.[52]

Additionally, the Al-O bond in alumina is more polar than the Si-O bond in silica, leading to a higher oxygen charge in AlOH groups. This increased polarity necessitates a lower H charge to prevent artificially high charges and multipole moments on the O atoms in AlOH groups. The bulk OH groups also experience greater local polarity, with oxygen and aluminum charges of -1.08e and +1.62e in the vicinity, respectively, compared to surface OH groups, which are exposed to

water with lower charges of -0.82e (O) and +0.41e (H), and therefore have lower charges of -0.79e (O) and +0.25e (H) (Figure 3b and Table 1). The slightly lower charge on the surface is induced by the less polar environment, corresponding to a small amount of depolarization, similar to recent evidence for  $\text{Ca}^{2+}$  ions in anhydrite versus gypsum (approximately +1.6e versus +1.7e).[53] The charge assignments for bulk OH were further validated by their agreement with experimental bulk moduli.

Second, we distinguish two charge settings for protonated and deprotonated surface  $\text{AlOH}$  groups, namely,  $\text{AlOH}_2^+ \cdots \text{Cl}^-$  groups at low pH values and  $\text{AlO}^- \cdots \text{Na}^+$  groups at high pH values in solution (Figure 3b and Table 1). The Al atoms in  $\text{AlOH}_2^+ \cdots \text{Cl}^-$  groups retain +1.62e charge, the oxygen charge also retains -0.79e, and the H charge is increased to +0.625e, leading to an overall positive charge of +1.0e that is compensated by an anion such as  $\text{Cl}^-$  (Figure 3b). The two nearest Al atoms in  $\text{AlO}^- \cdots \text{Na}^+$  groups absorb some of the incoming negative charge and have +1.48e charge, and the oxygen atom carries a higher charge of -1.26e, leading to an overall negative charge of -1.0e that is compensated by a cation such as  $\text{Na}^+$  (Table 1). Note that there are two Al atoms per such deprotonated OH group on the surface of alumina phases that are affected by these adjustments.

We tested different charge assignments, such as reduced negative charges in O atoms in  $\text{AlOH}_2^+ \cdots \text{Cl}^-$  down to -0.5e and reduced H charges down to +0.48e, which would be justified if also using bonded terms for Al-O bonds. However, we reflect covalent bonding here through nonbonded interactions, which requires upkeep of high charges for structural stability, such as -

0.79e for O. If charges are lowered, for example, the  $\text{OH}_2^+$  groups would dissociate from the surface. Keeping the O charge in  $\text{AlOH}_2^+$  groups at the same level as in neutral Al-OH groups prevents this failure mode, represents the interfacial properties well, and simplifies modifications for protonated groups. In  $\text{AlO}^- \cdots \text{Na}^+$  groups at high pH values, similar considerations apply. Lowering the nearby Al charges more significantly below +1.48e, which would be realistic in bonded models (e.g., Al down to +1.30e and O to -0.90e), can lead to instabilities in the nonbonded structure. Therefore, the Al charges of the two nearest neighbors are only reduced from +1.62e to +1.48e, and the oxygen charge remains at -1.26e.

The origin of these charges increments lies in partitioning the bulk Al charge of 1.62e into 6 equal contributions of +0.27e from the 6 coordinative Al-O bonds per Al atom. For example, bulk O atoms are bound to 4 Al atoms and then carry the opposite charge of  $-4 \cdot 0.27e = -1.08e$ . In case of an AlOH group, the H atom has a charge of +0.3e (bulk) or +0.25e (surface), which is closely the same contribution to the O charge as another Al atoms. The oxygen atoms in AlOH groups are bound to two Al atoms and one hydrogen atom, resulting in a charge of  $-2 \cdot 0.27e + (-0.3e) = -0.84e$  (bulk), for example. Finally, when AlOH groups are protonated to  $\text{AlOH}_2^+$  groups, the incoming charge of +1.0e is distributed over the two H atoms, increasing the H charge to  $2 \times +0.625e$  and (which is +1.0e more than the original H charge of 0.25e), and the oxygen charge remains at -0.79e (Figure 3b and Table 1). When AlOH groups are deprotonated,  $\text{AlO}^-$  groups form on the surface, and the negative charge of -1.0e is mainly distributed over the oxygen atoms and the two attached Al atoms. Hereby, removal of the H atom leaves -0.75e for distribution, of which the majority

would remain on the oxygen atom (-0.47e) and some part (-0.28e) be distributed over the two attached Al atoms, reducing their charge from +1.62e to +1.48e and increasing the oxygen charge from -0.79e to -1.26e. These charges are relatively high but suitable for a nonbonded model, which needs to cover some contributions by covalent through stronger ionic bonding.[7]

The Lennard-Jones parameters for the bulk alumina phases reflect the relative nonbonded atomic sizes of Al and O, and have been thoroughly validated for  $\alpha$ -Al<sub>2</sub>O<sub>3</sub>.[7] The LJ parameters for the Al-OH groups in bulk and surface environments are similar to the ones used for silanol groups on silica, which were suitable to accurately describe hydration energies and contact angles. In alumina, the oxygen atom has a similar environment and charge. The hydrogen atoms in OH groups have zero LJ parameters (or nearly zero in IFF-PCFF) and are only characterized by an atomic charge, which is lower than in silanol groups due to higher charge of Al and reduced acidity compared to silanol groups as known from experiments.

IFF parameters compatible with CVFF and OPLS-AA parameters are identical because the combination rules for  $r_{min, ij}$  are the same (geometric) (Equation (1)). A separate set of 12-6 LJ parameters is used for compatibility with CHARMM, AMBER, and DREIDING, which use arithmetic combination rules for  $r_{min, ij}$  (Equation (1)). Finally, a set of LJ parameters with 9-6 LJ options is included for use of IFF with PCFF, CFF, and COMPASS (Equation (2)). The origin of these differences was previously described.[42, 54-57] Different scaling of nonbond parameters between 1, 4-bonded atoms can be neglected due to the lack of angle and dihedral parameters (Equation (1)).

If covalent constraints for some bonds are desired, such as Al-O in protonated ( $\text{Al}_2\text{OH}_2^+$ ) or dissociated ( $\text{Al}_2\text{O}^-$ ) surface groups, they can be added along with appropriate harmonic bond and angle parameters, including adjustments in atomic charges and maintaining overall charge neutrality.

## **S5. Point of Zero Charge of Gibbsite, Hydrated Alumina, and Other Phases**

Data on the point of zero charge vary somewhat by source. An authoritative, up-to-date compilation is given by Kosmulski.[58] The most universal suggestion for the point of zero charge (neutral, OH-terminated surface) is a pH value of  $9 \pm 0.3$ , and a wider reported range of  $9 \pm 1$ . Some alumina samples, diaspore, boehmite, amorphous alumina, alumina nanoparticles, or other phases may have lower pzc if not given enough time to hydrate on the surface. Therefore, also reports of pzc as low as 7 are common.[59] On balance, therefore, we suggest a pzc of 8 to 8.5, which reasonably covers common situations.

The proposed models can be shifted to a specific point of zero charge that corresponds to the experimental data for the system of interest. Hereby, we can assume that the master surface titration curve (Figure 8a and Figure S13) will only be shifted on the horizontal pH axis, e.g., to a pzc to 7, 8 (default), or 9, and otherwise look closely the same. I.e., only the intersection point with the horizontal axis would shift to the new pzc. For example, if current models assume full OH termination at pH 8 and an ionization of  $+0.3 \text{ e/nm}^2$  at pH 7 ( $\text{OH}_2^+ \text{Cl}^-$ ), the same models can be used to represent pH 9 and pH 8 if it is known that the point of zero charge is at pH = 9 instead of

pH = 8. This approximation is up to an order of magnitude better than not making it. Experimental reference data and “master curves” for surface titration are known for a few similar OH-terminated oxides (silica, titania, ceria, alumina) share common features, even when the pzc is different, indicating a similar amount of ionization per surface area for a similar pH distance from the pzc, as well as some dependence on the electrolyte composition (Figure S13). In the future, it may be feasible to utilize machine learning to determine the expected ionization properties, however, currently the total amount of reference data remains limited.

## S6. Computation of Binding Free Energy from Langmuir Adsorption Isotherms: Theory and Limitations

The experimental adsorption isotherms of p-hydroxybenzoic acid show a clear trend as a function of pH (Figure 9a and Figure 5 in ref. [59]). The decrease in adsorbed amount for higher pH values is consistent with alumina surface chemistry and suggests a smaller negative binding free energy as seen in MD simulations for single molecules. Calculations of the associated binding free energies from the experimental Langmuir isotherms, however, showed a less intuitive correlation.[59] In the Langmuir model, [59, 60] the adsorbed amount  $\Gamma$  is given as:

$$\Gamma = \Gamma_{max} C_e / \left( \frac{1}{K_S} + C_e \right), \quad (S1)$$

with a maximum adsorbed amount  $\Gamma_{max}$ , the equilibrium concentration of p-hydroxybenzoate in solution  $C_e$ , and the adsorption coefficient  $K_S$ . Furthermore, the adsorption coefficient  $K_S$  is defined as:

$$K_S = \frac{N_{ads}}{(N_S - N_{ads})C_e}, \quad (S2)$$

with  $N_{ads}$  equal to the number of molecules adsorbed,  $N_S$  the number of available surface sites, and  $C_e$  the equilibrium concentration as in equation (S1).

Using the measured data (Figure 5 and Table 2 in ref. [59]), the values of  $K_S$  at pH values of 5, 6, 7, 8, and 9 were reported as 0.42, 0.32, 0.11, 0.18, and 0.38 l/mmol, respectively, with uncertainties between  $\pm 0.03$  and  $\pm 0.12$  l/mmol. The corresponding values of  $K_S$  are 420, 320, 110, 180, and 380 M<sup>-1</sup>. This trend appears at odds with the measured values of  $\Gamma_{max}$ , which decreased as shown in Figure 9a (equal to Figure 5 in the original paper ref. [59]) from 3.82, 2.11, 1.09, 0.49, to 0.41  $\mu\text{mol}/\text{m}^2$  from pH 5 to 9 and is well explicable based on surface chemistry.

The corresponding free energies of adsorption, calculated as:

$$\Delta G = -RT \ln K_S \quad (S3)$$

are -3.64, -3.47, -2.84, -3.13, and -3.58 kcal/mol at pH 5, 6, 7, 8, and 9, respectively. Like the trend in  $K_S$ , the increase in negative binding free energy towards pH 9 does not follow the trend in adsorption capacity in the isotherms (Figure 9a). Given the original measurements of adsorption isotherms including  $\Gamma_{max}$ , we expect that strong adsorption at pH 5 would correspond to the larger negative free energies of binding (-3.6 kcal/mol), while adsorption is expected to be much less favorable at pH 9 as seen in the isotherms and in MD simulation (Figure 9).

In conclusion, the calculated binding constants from the Langmuir models in equations (S1) and (S2) may not represent the experimental data well. Possible reasons lie in the definition of available surfaces sites  $N_S$  and occupied surface sites  $N_{ads}$  on these chemically diverse surfaces

(Figures 7 to 9). Simulations show high mobility across the surface paired with a certain level of attraction and average distance, driven by the amount electrostatic attraction and ion pairing. The original Langmuir models from the 1910s, as still used today, were not developed for chemically adaptable surface and absorbents with pH-sensitive chemistry in electrolytes; instead, they focused on mica, glass, and clean metal surfaces with rare gas adsorption in vacuum.[60] Future studies may therefore venture more into thermodynamic descriptions of reactive surfaces and their adsorption isotherms, such as our method of computation of  $K$  and  $\Delta G$  from MD simulations. In addition, infrared spectroscopy can provide further insight into binding modes and mechanisms as shown in ref. [59].

## Supplementary References

- [1] D.R. Lide, CRC Handbook of Chemistry and Physics CRC Press, Boca Raton, FL, 2015.
- [2] J. Liu, E. Tennessen, J. Miao, Y. Huang, J.M. Rondinelli, H. Heinz, Understanding chemical bonding in alloys and the representation in atomistic simulations, *J. Phys. Chem. C*, 122 (2018) 14996-15009.
- [3] H. Heinz, U.W. Suter, Atomic charges for classical simulations of polar systems, *J. Phys. Chem. B*, 108 (2004) 18341-18352.
- [4] R.J. Hill, Crystal-structure refinement and electron-density distribution in diaspore, *Phys. Chem. Miner.*, 5 (1979) 179-200.
- [5] J. Lewis, D. Schwarzenbach, H.D. Flack, Electric field gradients and charge density in corundum,  $\alpha$ -Al<sub>2</sub>O<sub>3</sub>, *Acta Cryst. A*, 38 (1982) 733-739.
- [6] C.C. Dharmawardhana, K. Kanhaiya, T.-J. Lin, A. Garley, M.R. Knecht, J. Zhou, J. Miao, H. Heinz, Reliable computational design of biological-inorganic materials to the large nanometer scale using Interface-FF, *Mol. Sim.*, 43 (2017) 1394-1405.
- [7] K. Kanhaiya, M. Nathanson, P.J. in 't Veld, C. Zhu, I. Nikiforov, E.B. Tadmor, Y.K. Choi, W. Im, R.K. Mishra, H. Heinz, Accurate force fields for atomistic simulations of oxides, hydroxides, and organic hybrid materials up to the micrometer scale, *J. Chem. Theor. Comput.*, 19 (2023) 8293-8322.
- [8] J.E. Huheey, E.A. Keiter, R.L. Keiter, *Inorganic Chemistry - Principles of Structure and Reactivity*, 4th ed., Harper Collins College Publishers, New York, 1993.
- [9] H. Saalfeld, M. Wedde, Refinement of the crystal structure of gibbsite, A1 (OH) 3, *Zeitschrift für Kristallographie-Crystalline Materials*, 139 (1974) 129-135.

[10] L. Smrčok, V. Langer, J. Křestan,  $\gamma$ -Alumina: a single-crystal X-ray diffraction study, *Acta Crystallographica Section C: Crystal Structure Communications*, 62 (2006) i83-i84.

[11] D. Yang, M. Krasowska, R. Sedev, J. Ralston, The unusual surface chemistry of  $\alpha$ -Al<sub>2</sub>O<sub>3</sub> (0001), *Phys. Chem. Chem. Phys.*, 12 (2010) 13724-13729.

[12] Y. Xie, D. Kocaefe, Y. Kocaefe, J. Cheng, W. Liu, The effect of novel synthetic methods and parameters control on morphology of nano-alumina particles, *Nanoscale Res. Lett.*, 11 (2016) 259.

[13] J.W. Ntalikwa, Determination of surface charge density of  $\alpha$ -alumina by acid-base titration, *Bulletin of the Chemical Society of Ethiopia*, 21 (2007).

[14] T.D. Pham, M. Kobayashi, Y. Adachi, Interfacial characterization of  $\alpha$ -alumina with small surface area by streaming potential and chromatography, *Colloids and Surfaces A: Physicochemical and Engineering Aspects*, 436 (2013) 148-157.

[15] J. Park, J.R. Regalbuto, A simple, accurate determination of oxide PZC and the strong buffering effect of oxide surfaces at incipient wetness, *J. Colloid Interface Sci.*, 175 (1995) 239-252.

[16] E.E. Newnham, Y.M.D. Haan, Refinement of the  $\alpha$  Al<sub>2</sub>O<sub>3</sub>, Ti<sub>2</sub>O<sub>3</sub>, V<sub>2</sub>O<sub>3</sub> and Cr<sub>2</sub>O<sub>3</sub> structures, *Zeitschrift für Kristallographie - Crystalline Materials*, 117 (1962) 235-237.

[17] J.M. McHale, A. Navrotsky, A.J. Perrotta, Effects of increased surface area and chemisorbed H<sub>2</sub>O on the relative stability of nanocrystalline  $\gamma$ -Al<sub>2</sub>O<sub>3</sub> and  $\alpha$ -Al<sub>2</sub>O<sub>3</sub>, *J. Phys. Chem. B*, 101 (1997) 603-613.

[18] T. Goto, O.L. Anderson, I. Ohno, S. Yamamoto, Elastic constants of corundum up to 1825 K, *Journal of Geophysical Research: Solid Earth*, 94 (1989) 7588-7602.

[19] H. d'Amour, D. Schiferl, W. Denner, H. Schulz, W. Holzapfel, High-pressure single-crystal structure determinations for ruby up to 90 kbar using an automatic diffractometer, *J. Appl. Phys.*, 49 (1978) 4411-4416.

[20] A.P. Amrute, Z. Łódziana, H. Schreyer, C. Weidenthaler, F. Schüth, High-surface-area corundum by mechanochemically induced phase transformation of boehmite, *Science*, 366 (2019) 485-489.

[21] A.N. Christensen, M. Lehmann, P. Convert, Deuteration of crystalline hydroxides. Hydrogen bonds of  $\gamma$ -AlOO (H, D) and  $\gamma$ -FeOO (H, D), *Acta Chem. Scand.*, 36 (1982) 303-308.

[22] M.P. Prange, X. Zhang, M.E. Bowden, Z. Shen, E.S. Ilton, S.N. Kerisit, Predicting surface energies and particle morphologies of boehmite ( $\gamma$ -AlOOH) from density functional theory, *J. Phys. Chem. C*, 122 (2018) 10400-10412.

[23] J. Majzlan, A. Navrotsky, W.H. Casey, Surface enthalpy of boehmite, *Clays Clay Miner.*, 48 (2000) 699-707.

[24] G.-h. Liu, Z. Li, X.-b. Li, T.-g. Qi, Z.-h. Peng, Q.-s. Zhou, Precipitation of spherical boehmite from concentrated sodium aluminate solution by adding gibbsite as seed, *International Journal of Minerals, Metallurgy, and Materials*, 24 (2017) 954-963.

[25] X. Xing, Z. Wei, L. Jiang, J. Zhang, Y. Luo, Y. Ma, Q. Cui, Abnormal compression behavior with unexpected negative linear compressibility of  $\gamma$ -AlOOH nanotubes, *Appl. Phys. Lett.*, 125 (2024) 093102.

[26] X. Zhou, J. Zhang, Y. Ma, H. Tian, Y. Wang, Y. Li, L. Jiang, Q. Cui, The solvothermal synthesis of  $\gamma$ -AlOOH nanoflakes and their compression behaviors under high pressures, *RSC Adv.*, 7 (2017) 4904-4911.

[27] D. Tunega, H. Pašalić, M.H. Gerzabek, H. Lischka, Theoretical study of structural, mechanical and spectroscopic properties of boehmite ( $\gamma$ -AlOOH), *J. Phys.: Condensed Matter*, 23 (2011) 404201.

[28] J.-a. Xu, J. Hu, L.-c. Ming, E. Huang, H. Xie, The compression of diaspore, AlO(OH) at room temperature up to 27 GPa, *Geophys. Res. Lett.*, 21 (1994) 161-164.

[29] K.-D. Grevel, M. Burchard, D.W. Faßhauer, T. Peun, Pressure-volume-temperature behavior of diaspore and corundum: An in situ x-ray diffraction study comparing different pressure media, *J. Geophysical Research: Solid Earth*, 105 (2000) 27877-27887.

[30] S. Huang, J. Xu, D. Liu, B. Li, Z. Ye, W. Chen, Y. Kuang, F. Chi, D. Fan, M. Ma, W. Zhou, Stability and thermoelasticity of diaspore by synchrotron x-ray diffraction and Raman spectroscopy, *Frontiers in Earth Science*, Volume 9 - 2021 (2021).

[31] F. Jiang, J. Majzlan, S. Speziale, D. He, T.S. Duffy, Single-crystal elasticity of diaspore, AlOOH, to 12GPa by Brillouin Scattering, *Physics of the Earth and Planetary Interiors*, 170 (2008) 221-228.

[32] H. Liu, J. Hu, J. Xu, Z. Liu, J. Shu, H.K. Mao, J. Chen, Phase transition and compression behavior of gibbsite under high-pressure, *Phys. Chem. Miner.*, 31 (2004) 240-246.

[33] E. Huang, J.F. Lin, J. Xu, T. Huang, Y.C. Jean, H.S. Sheu, Compression studies of gibbsite and its high-pressure polymorph, *Phys. Chem. Miner.*, 26 (1999) 576-583.

[34] H. Heinz, T.J. Lin, R.K. Mishra, F.S. Emami, Thermodynamically consistent force fields for the assembly of inorganic, organic, and biological nanostructures: the INTERFACE force field, *Langmuir*, 29 (2013) 1754-1765.

[35] P.V. Coveney, R.R. Highfield, When we can trust computers (and when we can't), *Philosophical Transactions of the Royal Society A*, 379 (2021) 20200067.

[36] H. Heinz, H. Ramezani-Dakhel, Simulations of inorganic-bioorganic interfaces to discover new materials: insights, comparisons to experiment, challenges, and opportunities, *Chem. Soc. Rev.*, 45 (2016) 412-448.

[37] X. Shao, C. Zhu, P. Kumar, Y. Wang, J. Lu, M. Cha, L. Yao, Y. Cao, X. Mao, H. Heinz, Voltage modulated untwist deformations and multispectral optical effects from ion intercalation into chiral ceramic nanoparticles, *Adv. Mater.*, (2023) 2206956.

[38] S. Akkineni, C. Zhu, J. Chen, M. Song, S.E. Hoff, J. Bonde, J. Tao, H. Heinz, S. Habelitz, J.J. De Yoreo, Amyloid-like amelogenin nanoribbons template mineralization via a low-energy interface of ion binding sites, *Proceedings of the National Academy of Sciences*, 119 (2022) e2106965119.

[39] H. Ramezani-Dakhel, L. Ruan, Y. Huang, H. Heinz, Molecular mechanism of specific recognition of cubic Pt nanocrystals by peptides and of the concentration-dependent formation from seed crystals, *Adv. Funct. Mater.*, 25 (2015) 1374-1384.

[40] L. Ruan, H. Ramezani-Dakhel, C.-Y. Chiu, E. Zhu, Y. Li, H. Heinz, Y. Huang, Tailoring molecular specificity toward a crystal facet: a lesson from biorecognition toward Pt {111}, *Nano Lett.*, 13 (2013) 840-846.

[41] S. Wang, E. Zhu, Y. Huang, H. Heinz, Direct correlation of oxygen adsorption on platinum-electrolyte interfaces with the activity in the oxygen reduction reaction, *Sci. Adv.*, 7 (2021) eabb1435.

[42] H. Heinz, H. Koerner, K.L. Anderson, R.A. Vaia, B.L. Farmer, Force field for mica-type silicates and dynamics of octadecylammonium chains grafted to montmorillonite, *Chem. Mater.*, 17 (2005) 5658-5669.

[43] H. Heinz, H.J. Castelijns, U.W. Suter, Structure and phase transitions of alkyl chains on mica, *J. Am. Chem. Soc.*, 125 (2003) 9500-9510.

[44] J. Liu, E. Tennessen, J. Miao, Y. Huang, J.M. Rondinelli, H. Heinz, Understanding chemical bonding in alloys and the representation in atomistic simulations, *J. Phys. Chem. C*, 122 (2018) 14996-15009.

[45] J. Duffy, Chemical bonding in the oxides of the elements: a new appraisal, *J. Solid State Chem.*, 62 (1986) 145-157.

[46] D.E. Gibbs, Chemistry: Concepts and models (Robinson, William R.; Odom, Jerome D.; Holtzclaw, Henry F., Jr.), *J. Chem. Educ.*, 69 (1992) A278.

[47] J.A. Duffy, Ionic– covalent character of metal and nonmetal oxides, *J. Phys. Chem. A*, 110 (2006) 13245–13248.

[48] K. Kanhaiya, S. Kim, W. Im, H. Heinz, Accurate simulation of surfaces and interfaces of ten FCC metals and steel using Lennard–Jones potentials, *npj Comput. Mater.*, 7 (2021) 17.

[49] M.P. Oliveira, P.H. Hünenberger, Influence of the Lennard–Jones combination rules on the simulated properties of organic liquids at optimal force-field parametrization, *J. Chem. Theory Comput.*, 19 (2023) 2048–2063.

[50] J.W. Ponder, C. Wu, P. Ren, V.S. Pande, J.D. Chodera, M.J. Schnieders, I. Haque, D.L. Mobley, D.S. Lambrecht, R.A. DiStasio, M. Head-Gordon, G.N.I. Clark, M.E. Johnson, T. Head-Gordon, Current Status of the AMOEBA polarizable force field, *J. Phys. Chem. B*, 114 (2010) 2549–2564.

[51] J.A. Lemkul, J. Huang, B. Roux, A.D. MacKerell, An empirical polarizable force field based on the classical Drude oscillator model: Development history and recent applications, *Chem. Rev.*, 116 (2016) 4983–5013.

[52] F.S. Emami, V. Puddu, R.J. Berry, V. Varshney, S.V. Patwardhan, C.C. Perry, H. Heinz, Force field and a surface model database for silica to simulate interfacial properties in atomic resolution, *Chem. Mater.*, 26 (2014) 2647–2658.

[53] R.K. Mishra, S. Darouich, P.J. in 't Veld, R.J. Flatt, H. Heinz, Understanding hydration reactions, mechanical properties, thermal expansion, and organic interfacial interactions of calcium sulfate hydrates from the atomic scale, *Cem. Concr. Res.*, 189 (2025) 107740.

[54] S. Wang, K. Hou, H. Heinz, Accurate and compatible force fields for molecular oxygen, nitrogen, and hydrogen to simulate gases, electrolytes, and heterogeneous interfaces, *J. Chem. Theory Comput.*, 17 (2021) 5198–5213.

[55] J. Liu, J. Zeng, C. Zhu, J. Miao, Y. Huang, H. Heinz, Interpretable molecular models for molybdenum disulfide and insight into selective peptide recognition, *Chem. Sci.*, 11 (2020) 8708–8722.

[56] R.K. Mishra, L. Fernández-Carrasco, R.J. Flatt, H. Heinz, A Force Field for tricalcium aluminate to characterize surface properties, initial hydration, and organically modified interfaces in atomic resolution, *Dalton Trans.*, 43 (2014) 10602–10616.

[57] H. Heinz, R.A. Vaia, B.L. Farmer, R.R. Naik, Accurate simulation of surfaces and interfaces of face-centered cubic metals using 12–6 and 9–6 Lennard-Jones potentials, *J. Phys. Chem. C*, 112 (2008) 17281–17290.

[58] M. Kosmulski, The pH dependent surface charging and points of zero charge. X. Update, *Adv. Colloid Interface Sci.*, 319 (2023) 102973.

[59] M.R. Das, J.M. Borah, W. Kunz, B.W. Ninham, S. Mahiuddin, Ion specificity of the zeta potential of  $\alpha$ -alumina, and of the adsorption of p-hydroxybenzoate at the  $\alpha$ -alumina–water interface, *J. Colloid Interface Sci.*, 344 (2010) 482–491.

[60] I. Langmuir, The adsorption of gases on plane surfaces of glass, mica, and platinum *J. Am. Ceram. Soc.*, 40 (1918) 1361–1403.